2016

STM Investigation of Silicene

Jincheng Zhuang
University of Wollongong

STM Investigation of Silicene

This thesis is presented as part of the requirements for the Award of the Degree of

Doctor of Philosophy

from the

University of Wollongong

by

JINCHENG ZHUANG
B. Sc., M. Sc.

Institute for Superconducting and Electronic Materials

Faculty of Engineering

April 2016

CERTIFICATION

I, Jincheng Zhuang, declare that this thesis, submitted in fulfilment of the requirements for the award of Doctor of Philosophy, in the Institute for Superconducting & Electronic Materials, Faculty of Engineering, University of Wollongong, is wholly my own work unless otherwise referenced or acknowledged. This document has not been submitted for qualifications at any other academic institution.

Jincheng Zhuang

20/08/ 2016

DEDICATION

To my family and friends, who stand by me all the time.

ACKNOWLEDGEMENTS

My thesis is undertaken with the supports from all the people in the Institute for Superconducting and Electronic Materials (ISEM) at the University of Wollongong in Australia.

Firstly, I wish to express my deepest gratitude to my research supervisors, Professor Shi Xue Dou, for their academic supervision and guidance, constant support and encouragement, invaluable advice throughout my doctoral degree. I would like to express my utmost appreciation to my co-supervisor, Dr. Yi Du, for his professional suggestions and inculcation, including theoretical knowledges and experimental skills. He spent amounts of time to mentor me in the construction of self-confidence and future orientation as well. I am deeply grateful to Dr. Xun Xu, for his support and supervision for my research. I also wish to thank Dr. Zhi Li, for his great guidance of passing on knowledge in the field of condensed matter physics.

Furthermore, I am grateful to Dr. Wai Kong Yeoh, who spent his valuable time on microstructural test for my samples and manuscript reversion. My deep gratitude goes to my co-workers, Mr. Haifeng Feng, Mr. Long Ren, and Ms. Li Wang, who have been very helpful, sharing their experiences and knowledge. I would also like to thank Dr. Tania Silver for her critical reading of my manuscripts and thesis.

I would also like to thank for their kind assistance from staffs and technicians in ISEM, including Dr. Germanas Peleckis (XRD, PPMS), Dr. Kosta Konstantinov (BET, TGA/DTA), Mr. Darren Attard (SEM), Mr. Tony Romeo (SEM, EDS), Dr. Dongqi Shi (PLD), Mrs. Crystal Login, Mrs. Narelle Badger, Mrs. Joanne George (OH&S), Mr. Robert Morgan, Mr. Mathew Davis, Mrs. Candace Gabelish.

Moreover, many thanks to Dr. Jianping Yang, Mr. Hongqiang Wang, Mr. Tengfei Zhou, Mr. Ruixiang Yu, Mr. Feixiang Xiang, Mr. Jun Wang, Mr. Muhamad Faiz, Ms. Xuan Wen Gao, and other students and staff at ISEM, for their kind help and valuable advice.

Finally, I would like to express my deep appreciation and love to my parents, wife, who are standing by me and encouraging me to move forward all the time.

ABSTRACT

Silicene, the silicon-based counterpart of graphene, has attracted intensive interest due to its unique characteristics and a wide range of promising applications. In this thesis, we investigate its growth mechanism, EPC strength, and oxygen adsorption functionality. The details are as following:

1. Epitaxial growth mechanism of silicene layers fabricated on a Ag(111) surface by MBE deposition were reported in this chapter. The coverage effect and the structural defects have been identified by using STM imaging. It is found that substrate temperature plays a critical role in determination of the silicene superstructures. Several types of defects are observed in different silicene superstructures, which are most likely induced by the low coverage effect or the interface lattice mismatch between silicene and Ag(111). Furthermore, the silicene sheet prefers to initially arise at the terrace edge of the substrate. Our results imply that the growth mechanism of all silicene superstructures follows the Stranski-Krastanov growth mode.

2. The special coupling between Dirac fermion and lattice vibrations, in other words, electron phonon coupling, in silicene layers on an Ag(111) surface was probed by *in-situ* Raman spectroscopy. The tensile strain, induced by the lattice mismatch between silicene and the substrate, and the charge doping from the substrate, modulate EPC strength. The Raman spectrum clearly reveals evolution of defect peaks with coverage of silicene layers. The peaks at low frequency correspond to the different electron scattering modes occurring at the zigzag and armchair edges. This work implies that Raman spectroscopy allows unambiguous, fast, and nondestructive identification of silicene layers, which is critically lacking in this emerging research field so far.

3. Monolayer silicene grown on Ag(111) surfaces prove a band gap that is tunable by oxygen adatoms from semimetallic to semiconducting type. We find that the adsorption configurations and amounts of oxygen adatoms on the silicene surface perform as the critical factors for band gap engineering, which is determined by different buckling degrees in $\sqrt{13}\times\sqrt{13}$, 4×4, and $2\sqrt{3}\times2\sqrt{3}$ superstructures. The Si-O-Si bonds are the most energy-favored species formed on $\sqrt{13}\times\sqrt{13}$, 4×4, and $2\sqrt{3}\times2\sqrt{3}$ structures under oxidation, which is verified by in-situ Raman spectroscopy as well as first-principles calculations. The silicene monolayers retain their structures when fully covered by oxygen adatoms. Our work demonstrates the feasibility of tuning the band gap of silicene with oxygen adatoms, which, in turn, expands the base of available two-dimensional electronic materials for devices with properties that is hardly realized with graphene oxide.

4. Epitaxial silicene shows a strong interaction with the substrate that dramatically affects its electronic structure. The role of electronic coupling in the chemical reactivity between the silicene and the substrate is still unclear so far. The hybridization between Si and Ag induces a metallic surface state, which can gradually decay by oxygen adsorption. XPS results manifest the decoupling of Si-Ag bonds as well as the relatively oxygen resistance of Ag(111) surface after oxygen treatment. First-principles calculations have also illustrated the evolution of the electronic structure of silicene during oxidation. It has been demonstrated experimentally and theoretically that the high chemical activity of 4×4 silicene is attributable to the Si pz state, while the Ag(111) substrate exhibits relatively inert chemical behaviour.

5. Silicene is a monolayer allotrope of silicon atoms arranged in a honeycomb structure with massless Dirac fermion characteristics, similar to graphene. It ensures development of silicon-based multifunctional nanoelectronic and spintronic devices operated at room temperature due to strong spin-orbit coupling. Nevertheless, until now, silicene could only be

epitaxially grown on conductive substrates. The strong silicene-substrate interaction may depress its superior electronic properties. A quasi-free-standing silicene layer that has been successfully obtained through oxidization of bilayer silicene on the Ag(111) surface. The oxygen atoms intercalate into the underlayer of silicene, which can isolate the top layer of silicene from the substrate. In consequence, the top layer of silicene exhibits the signature of a 1×1 honeycomb lattice and hosts massless Dirac fermions due to much less interaction with the substrate. Furthermore, the oxidized silicon buffer layer is expected to serve as an ideal dielectric layer for electric gating in electronic devices. These findings are relevant for the future design and application of silicene-based nanoelectronic and spintronic devices.

TABLE OF CONTENTS

LIST OF ABBREVIATIONS

2D	Two Dimensional
DFT	Density Functional Theory
QSHE	Quantum Spin Hall Effect
QAHE	Quantum Anomalous Hall Effect
LEED	Low Energy Electron Diffraction
BZ	Brillouin Zone
EPC	Electron-Phonon Coupling
UHV	Ultra High Vacuum
ARPES	Angle Resolved Photoemission Spectroscopy
QPI	Quasiparticle Interferences
STS	Scanning Tunnelling Spectroscopy
HUC	Hydrogenated Unit Cell
HCT	Honeycomb Chained Triangle
IET	Inequivalent Triangle
MBE	Molecular Beam Epitaxy
K-Cell	Knudsen Diffusion Cell
DOS	Density of State
TERS	Tip-Enhance Raman Spectroscope
XPS	X-ray Photoelectron Spectroscopy
SK	Stranski-Krastanov
SOC	Spin-Orbit Coupling
LT-STM	Low-Temperature Scanning Tunneling Microscopy
ML	Monolayer
VW	Volmer-Weber

FM	Frank-van der Merwe
LB	Low Buckled
FS	Free-Standing
BCS	Bardeen-Cooper-Schrieffer
VASP	Vienna Ab Initio Simulation Package
PAW	Projector Augmented Wave
GGA	Generalized Gradient Approximation
PBE	Perdew-Burke-Ernzerhof
AIMD	ab initio Molecular Dynamics
SSS	Shockley Surface State
HSB	Hybridized Surface Band
FETs	Field Effect Transistors
DP	Dirac Point

CHAPTER 1

INTRODUCTION

1.1 General background.

Stable and single-atom thick two dimensional (2D) materials could be exfoliated from van der Waals solids, which were demonstrated for the first time by the discovery of graphene [1]. These materials possess unique and fascinating properties due to their novel electronic structures [2-6]. Since then, graphene has generated enormous interest due to the novel physical and chemical phenomena evoked by the dimensional confinement effect. The rapid and recent advances in this carbon-based 2D material have raised teasing questions on exploring new 2D materials exhibiting a rich spectrum of properties. Among them, hexagonal boron nitride (*h*-BN) with similar structure to graphene is an insulator [7], while monolayer MoS_2 and WS_2 are semiconductors with direct-band-gap [8,9]. The plentiful variety of properties in different 2D materials indicates promising potential for device engineering and applications in sensing, photonicsn, energy storage, *etc*. These 2D materials with atomic layers have been made to be incorporated into devices to realize exceptional performance. Due to the incompatibility with current semiconductor-based electronic techniques, hwoever, it is extremely difficult to develop reliable and durable applications. Furthermore, achieving single crystals with large size has become the main obstacle to their properties characterization and device fabrication. Exploration for new 2D materials is therefore highly desirable for potential applications.

Similar to graphene, silicene is a single atom thick material with the characteristic honeycomb structure. In graphene, the carbon atoms are more stable in sp^2 hybridization rather than sp^3 hybridization, while the situation is reversed for silicon. Thus, it is challenging

to synthesize silicene. Silicon atoms are not energetically encouraging in terms of spontaneously forming silicene, limiting the conventional chemical or physical methods that could be used to fabricate silicene. Its exciting and rich physics have been predicted by many theoretical calculations [10-12]. For instance, density functional theory (DFT) calculations indicate that silicene exhibits the Dirac fermion state in a linear dispersion band structure close to the Fermi level [11]. The quantum spin Hall effect (QSHE) was also forecast in silicene [13]. The electronic properties of silicene could be modulated by the effects of the substrate [14-16], defects [17,18], interlayer coupling [19], and metal interactions [20]. These theoretical works have paved the way to the exploration of anisotropic transport behaviour and experimentally investigation of three novel properties of silicene [21-31]. Moreover, silicene is inherently compatible with current silicon-based chip-production processes, which is advantageous in contrast with graphene, so silicene could be a material of the future.

1.2 Literature review and research motivation.

1.2.1 Two-dimensional structure of silicene.

Silicene, silicon-based atomically thin 2D sheets was first proposed based on first-principles total-energy calculations [32]. Unlike the planar structure of graphene, however, with sp^2 hybridization configuration, silicon atoms arrange themselves in the form of low buckled structure due to a mixture of sp^2 hybridization and sp^3 hybridization. Silicene has been firstly fabricated on Ag(111) substrate in 2012 [14]. Rich phases of silicene have been grown on various substrates, evoked by the competition between sp^2 hybridization and sp^3 hybridization. These substrates include Ag(111) [2,10,14,28,33,34], Ag(110) [35], Au(110) [36], Ir(111) [3], and ZrB_2-covered Si(111) [4]. Most silicene samples are fabricated on

Ag(111) substrate, and this thesis is focused on the films grown on Ag(111) substrate.

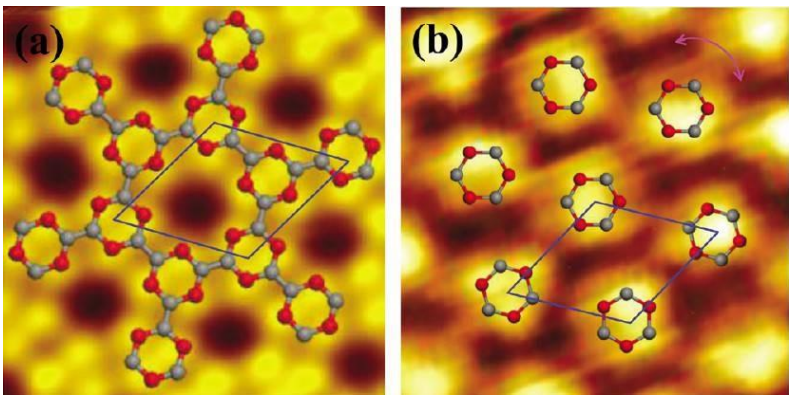

Fig. 1.1 STM images and models of H phase silicene and T phase silicene [2].

4×4 silicene phase is a 4×4 reconstruction (with respect to the Ag(111) substrate) or a 3×3 reconstruction (with respect to 1×1 silicene) [10]. Large-scale 4×4 silicene films can be easily fabricated by maintaining the substrate temperature at around 420 K during deposition. Fig. 1.1(a) and (b) displays the phase exhibiting honeycomb structures (labelled H) and the other phase, which consists of close-packed protrusions (labelled T), respectively. The ratio between these two phases could be modulated by the coverage and the deposition temperature, where phase T tends to form at a lower Si coverage and lower temperature, but will disappear and be replaced by phase H at higher coverage and temperature. Thus, phase T is regarded as the precursor of the stable phase H. Based on experimental observation from scanning tunnelling microscopy (STM) results and first-principles calculations, a model of a low buckled honeycomb structure with missing hexagonal silicon rings at the corners in each 4×4 unit cell is proposed, as shown in Fig. 1.1(b). Although similar STM results have been reported by Lin *et al.* [20] and Vogt *et al.* [13], different structure models have been planned, where the hole in the STM image is caused by the six Si atoms that are buckled upward. It is reported that absorption of hydrogen changes the buckling structure of 4×4 silicene [37]. Through detailed discussion on the STM results and theoretical calculations, they proposed a structural model with intact honeycomb structure, which is helpful to clarify this controversy.

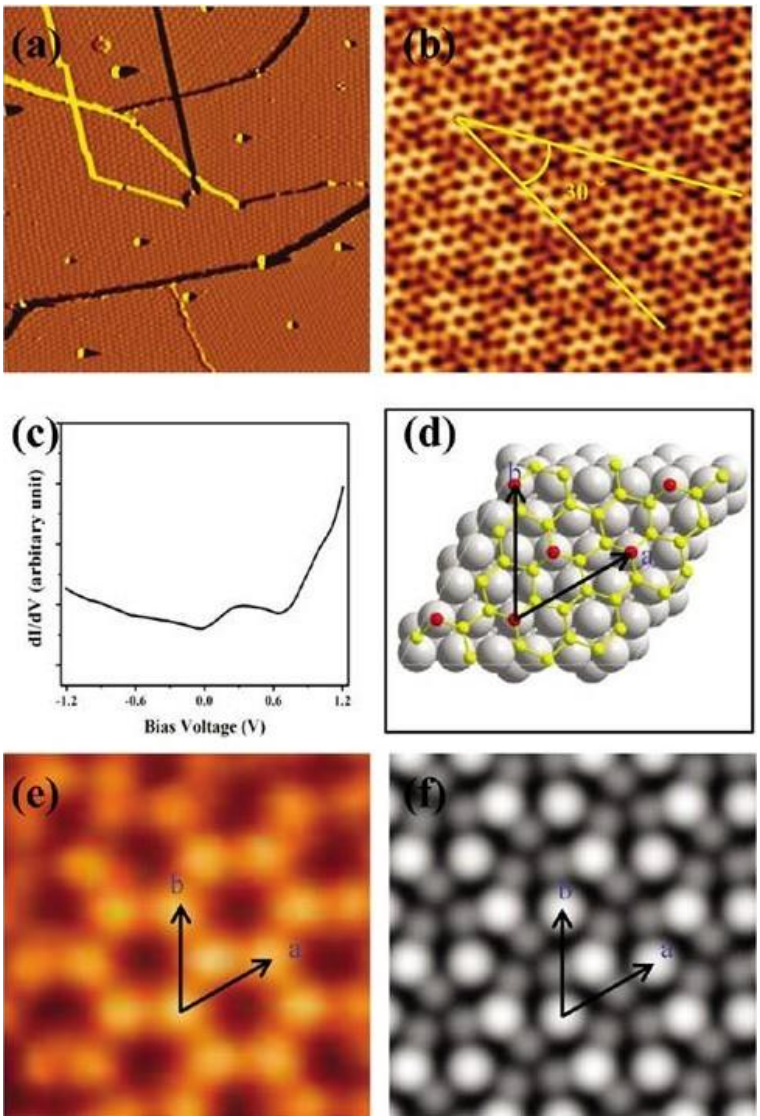

Fig. 1.2 (a) A derivative STM imageof 0.9 monolayer (ML) silicon atoms (200×200 nm^2, V_{tip} = 1.43 V). (b) Enlarged view of STM image in (a), showing the atomic structure of moiré patterns (15×15 nm^2, V_{tip} = −1.0 V). The period of the honeycomb rings identified by the bright areas is 1.0 nm, while other areas are defective and disordered. (c) The density of states (DOS) of this phase shows a peak at 0.3 V and a shoulder at 0.9 V. (d) Simulated model of $2\sqrt{3}\times2\sqrt{3}$ superstructure of silicene. (e,f) Comparative results for experimental and calculated STM images. All these figures are from Ref [2].

A new phase of silicene defined as $2\sqrt{3}\times2\sqrt{3}$ silicene emerges (with respect to 1×1 silicene) on increasing the substrate temperature to 480 K [2]. This phase usually manifests itself as a defective moiré pattern with a period about 3.8 nm, as shown in Fig. 1.2. Figure 2(b) shows that there are hexagonal rings at the bright part and defective dark part between adjacent

moiré patterns. Based on the first-principles calculations, a structure model for $2\sqrt{3}\times2\sqrt{3}$ silicene is proposed, as shown in Fig. 1.2(d) and (f). The dark parts of the moiré pattern are made up of silicon atoms that deviate from the structure of Ag(111). Therefore, the strong interaction between silicene and Ag(111) substrate, as demonstrated by the moiré pattern, will keep the hexagonal rings stable and intact.

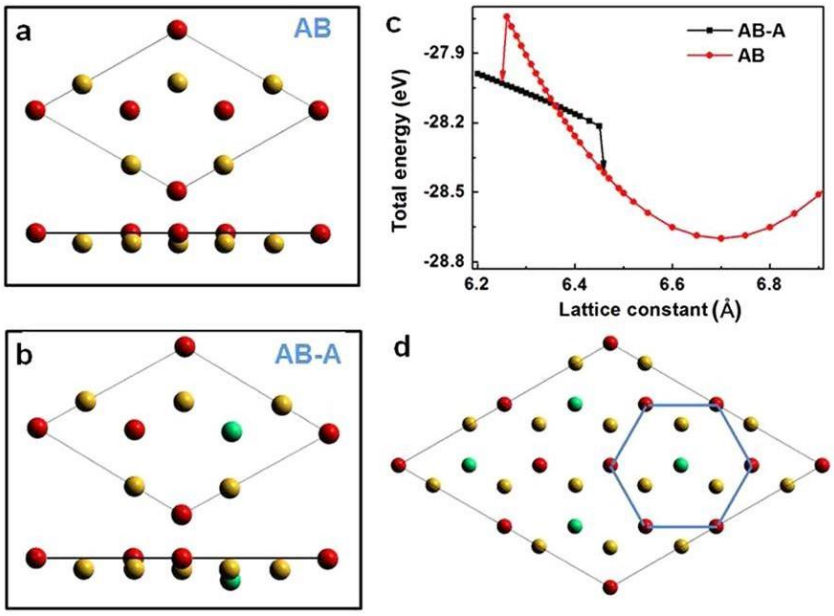

Fig. 1.3 (a), (b) AB model and AB-A model for lattice arrangement, respectively. (c) Simulated energy phase transition diagram based on two models. (d) A larger schematic model illuminating the honeycomb structure of $\sqrt{3}\times\sqrt{3}$ reconstructed silicene [19].

Further increasing the substrate temperature up to 500 K leads to a more stable silicene phase defined as $\sqrt{3}\times\sqrt{3}$ silicene. Due to the honeycomb structure, this phase is the most extensively investigated phase among all the silicene phases. Meanwhile, it may be the most controversial phase. Chen *et al.* [2,21] proposed a structural model with a unit cell consisting of three layers of silicon atoms, as shown in Fig. 1.3. Arafune *et al* [38] proposed a bilayer structure according to the layer thickness, as well as sixfold symmetry of the surface structure. Recently, a new configuration in which substrate Ag atoms are segregated on the silicene

surface forming a √3×√3 superstructure, which is similar to √3×√3 silicene, was proposed by Shirai *et al.* based on tensor low energy electron diffraction (LEED) analysis [39]. This scene has also been observed in very recent STM works [40,41]. All these results query whether √3×√3 silicene is a true layered structure or not.

Furthermore, there are various superstructures with different buckling patterns and periodicity [42]. However, systematic experimental and theoretical studies are still lacking for these phases. Even for the three phases discussed above, there are controversies rather than unanimous views. Detailed studies on the structure of silicene phases are needed.

1.2.2 Phonon modes in silicene

Raman spectroscopy is widely used for structural characterization, phonon dynamics research, and electron-phonon coupling (EPC) investigations in 2D Dirac fermion systems [43]. In silicene, the long-wavelength optical E_{2g} phonon mode at the Γ point of the Brillouin zone (BZ), which corresponds to the relative displacement of nonequivalent neighbouring silicon atoms [14], is the phonon mode flagship and of particular interest. Due to the buckled structure, any perturbations will be expected to induce direct electronic transitions across the Dirac point, that is, E_{2g} phonons couple to low-energy excitations. The vibrational properties of silicene were first studied by DFT calculations [44]. By considering the buckling of silicene and its preferred energy states, the non-resonance Raman spectra of free-standing silicene are reflected by a prime peak (E_{2g}) located at around 570 cm^{-1}. The Raman peaks at lower frequencies than the E_{2g} peak are attributed to the effects of defects at the edges.

Although the multilayer silicene films show just a very small top surface oxidation after 24 h exposure to ambient air [45], the monolayer silicene is unstable under ambient conditions [45]. In order to eliminate the effects of the oxidation of silicene, co-deposition of Al and O_2

to form an Al_2O_3 capping layer in an ultra high vacuum (UHV) ambient as a protective layer was performed before the *ex-situ* Raman measurement, resulting in an intact Al_2O_3/silicene/Ag heterostructure [46,47]. Combined with DFT calculation, the Raman spectra of different silicene superstructures indicate that the E_{2g} peak is located at around 520 cm^{-1}, which is much smaller than the value for simulated free-standing silicene [44]. Furthermore, the Raman spectrum as a function of excitation energy was also investigated to probe the resonant behaviour [47]. The results indicate that the monolayer silicene consists of a mixture of hybridized sp^2 structure and sp^3 structure. The broad shoulder at lower wavenumber (450-510 cm^{-1}) than that of the silicene signature E_{2g} peak is ascribed to buckling-induced vibrational modes in Ref. 47. Nevertheless, this shoulder may be associated with the effects of the formation of Si-O bonds. Because the oxygen adsorption energy on a Si surface with dangling bonds is low, the monolayer silicene is extremely sensitive to oxygen. Therefore, oxidation cannot be ignored in this *ex-situ* measurement. *In-situ* Raman measurements under UHV are expected to be performed to identify silicene in different phases and reveal the details of the phonon modes as well as their relationship to the silicene electronic properties.

1.2.3 Electronic structures in silicene

Due to the honeycomb structure, silicene is predicted to share similar novel electronic properties to graphene [32,48-50], where the electronic π- and π*- bands resulting from the Si $3p_z$ orbital are dispersed linearly to cross around the Dirac point, and charge carriers behave like massless Dirac fermions [20]. Nevertheless, due to the fact that 12 atoms are in pure sp^2 state and the rest 6 atoms are in sp^2-sp^3 mixed hybridization [14], monolayer silicene shows strong interfacial coupling with the substrate. In this case, the electrons are confined by the substrate, leading to the absence of Landau levels and Dirac fermion characteristics [51]. The

angle resolved photoemission spectroscopy (ARPES) results indicate that no Dirac cones could be observed at the *K* points of the monolayer silicene Brillouin zone, but instead, a dominant hybrid surface metallic band is generated by the strong interaction between the monolayer silicene and the Ag(111) *sp*-band [19,52-54]. Therefore, the electronic structure of monolayer silicene has been intensively modulated by the substrate, resulting from the robust interaction between the monolayer silicene and the Ag(111).

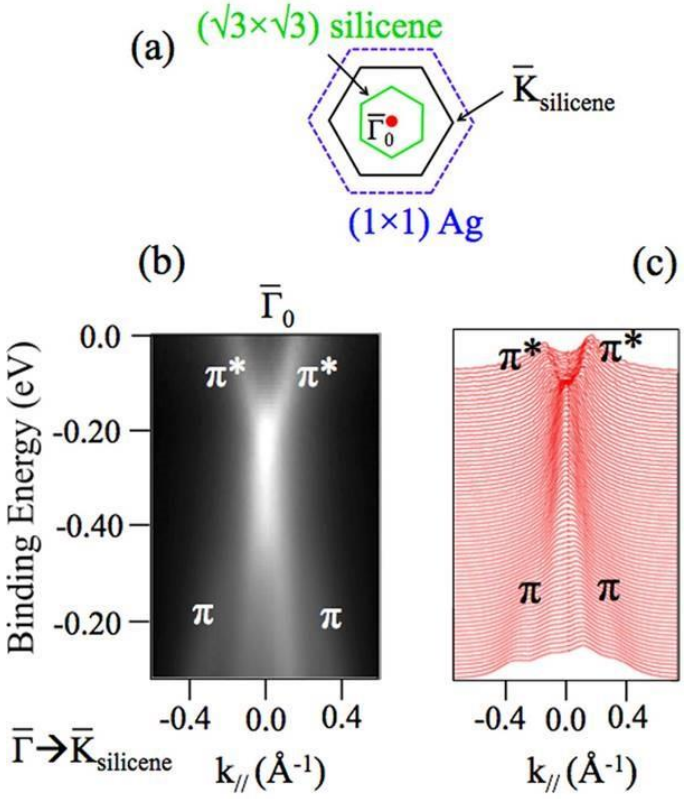

FIG. 1.4 (a) Schematic illustration of Brillouin zones of 1×1 silicene, √3×√3 silicene, and 1×1 Ag(111). (b) Linear dispersion of electronic bands at Γ_0. (c) Waterfall line profiles of the dispersion displayed in (b) as a guide for the eyes [55].

Due to the indirect contact with the silver substrate, √3×√3 silicene shows a low buckled structure and weak interfacial coupling with the substrate. Thus, the Dirac fermion characteristics are expected to be present in the electronic structure of √3×√3 silicene. The direct signature of Dirac fermions, the Dirac cones, appear on the *K* and *K*' points of the 1×1

silicene Brillouin zone as well as the Γ points of $\sqrt{3}\times\sqrt{3}$ silicene Brillouin zone, as shown in Fig. 1.4 [55,56]. The Dirac point is below the Fermi surface, which is caused by the electron doping from the Ag(111) substrate [57]. The calculated Fermi velocity from the ARPES results at room temperature could be 0.3×10^6 ms^{-1}, which is still a little smaller than that of graphene [55,58], but high enough for potential silicene-based applications. The linear band dispersion is also deduced from the pronounced quasiparticle interferences (QPI) patterns in the scanning tunnelling spectroscopy (STS) measurements, demonstrating the existence of Dirac fermions in the $\sqrt{3}\times\sqrt{3}$ silicene [19].

There are two critical discoveries that could be implied from the investigation of the silicene electronic structure by both STS and ARPES measurements. Firstly, the electronic structure of single layer silicene is intensively modulated by Si-Ag coupling. Secondly, the Dirac fermion characteristics have been observed in $\sqrt{3}\times\sqrt{3}$ silicene due to the weak coupling of Si atoms in this superstructure. Since the presence of Dirac fermion properties is crucial for the application of 2D materials [59], silicene shows highly promising prospects for potential application in innovative devices due to its direct compatibility with silicon micro and nano technologies.

1.2.4 Chemical properties of silicene

Hydrogenation was found to be a useful chemical method to modulate the electronic properties of graphene, such as by opening a band gap [60-62]. In contrast to the graphene case, where hydrogen tends to form clusters, hydrogenated silicene exhibits a long-range ordered structure. Combined with first principles calculations, the STM results indicate that there are seven hydrogen atoms in one (4×4) unit cell, and that the buckling configuration of Si atoms in silicene is spontaneously rearranged after hydrogenation [37].

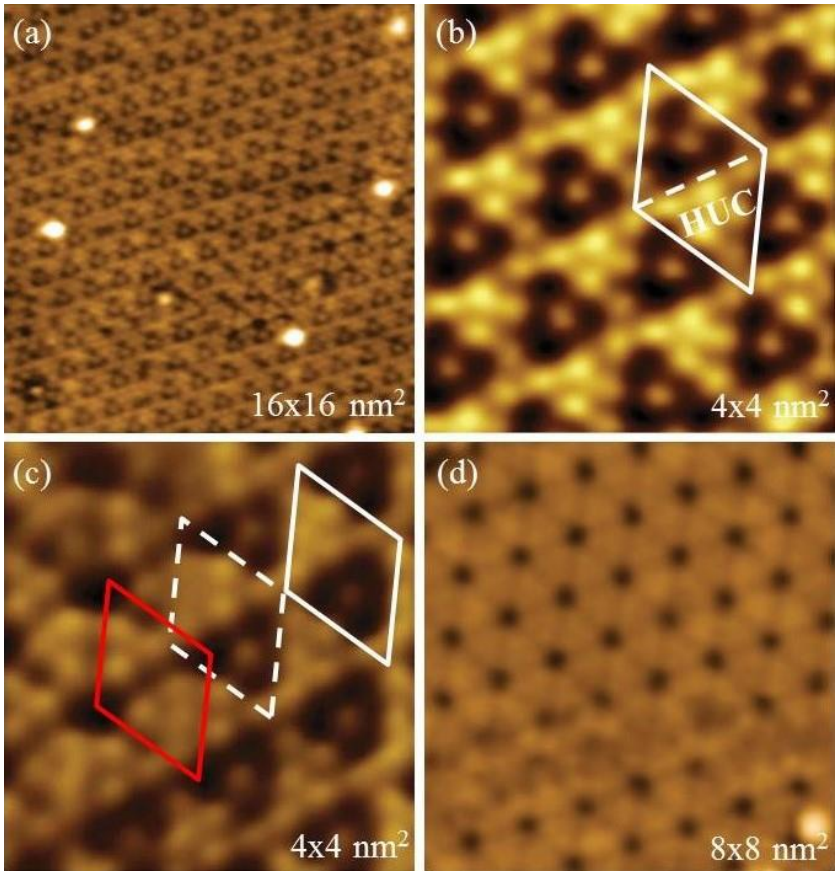

Fig. 1.5 (a) STM image of a hydrogenated silicene-(4×4) surface showing an ordered (4×4) structure. (b) Enlargement of the hydrogenated (4×4) phase. The white rhombus marks an apparent unit cell of the structure. There are six bright protrusions in one hydrogenated unit cell (HUC) and one protrusion in the other HUC. (c) STM image showing a comparison between the positions of the apparent unit cells of clean and hydrogenated silicene (4×4). The red and white rhombuses correspond to the clean (4×4) unit cells and the hydrogenated (4×4) unit cells, respectively. (d) The clean silicene-(4×4) surface is fully recovered after annealing the surface at 450 K [37].

Upon exposure to 900 L hydrogen at room temperature, a perfectly ordered structure with the same (3×3) periodicity can be observed, as shown in Fig. 1.5(a). There are no changes on further increasing the hydrogen dosage, indicating the saturation of hydrogen adsorption. Two inequivalent HUCs are identified in the high-resolution image of the hydrogenated structure, one with six bright spots while the other has only one bright spot in the middle, as shown in Fig. 1.5(b). The distance between the nearest bright spots is around 3.8 Å, similar to

the lattice constant of 1×1 silicene. Figure 1.5(c) displays clean 3×3 silicene in the left part of the image, whereas the right part is the hydrogenated region. The two sets of (3×3) unit cells are shifted along the Si-Si bond direction by the distance of one Si-Si bond length, induced by the change in the buckling configuration after hydrogenation. Moreover, dehydrogenation occurs and a clean silicene surface is recovered by means of annealing the sample to a moderate temperature (about 450 K), as shown in Fig. 1.5(d). Such homogenously ordered, reversible hydrogenation is valuable for modifying the electronic properties of silicene [37].

1.2.5 Argument on the existence of $\sqrt{3}\times\sqrt{3}$ silicene

Metal/semiconductor structures are of particular interest in several arenas. The Ag-Si system has been intensively studied for several decades due to its fascinating atomic arrangements and surface electronic states, as well as the related physical properties.

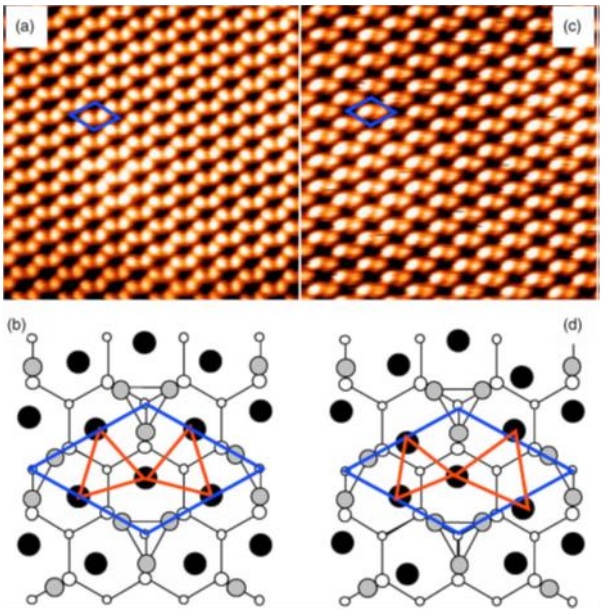

Fig. 1.6 (a) STM image of $\sqrt{3}\times\sqrt{3}$ silicene (V_{bias} = −0.6 V, I = 1.0 nA, 8.4×8.4 nm). (b) Model for HCT. (c) STM image of the same area as image (a) with different measurement parameter (V_{bias} = −0.3 V, I = 0.3 nA). (d) Model for IET [63].

The Ag $\sqrt{3}\times\sqrt{3}R30°$ reconstruction with a honeycomb structure on Si(111) was widely

investigated prior to the discovery of silicene. The honeycomb-chained-triangle (HCT) model and the inequivalent-triangle (IET) model were proposed to identify the atomic structure of the Si(111)-(√3×√3)-Ag surface, as shown in Fig. 1.6 (a) and (b), respectively [63,64]. It was first believed that the HCT structure observed at higher temperature (higher than 67 K) was evoked by the thermal fluctuations of both IET^{+} and IET^{-} structures at low temperature, while Zhang *et al.* found that Si(111)-(√3×√3)-Ag with the IET structure can also be observed both at room temperature (RT) and LT in STM results [63]. It suggests that the so-called HCT-IET phase transition could be caused by the condition of the microscope tip [64].

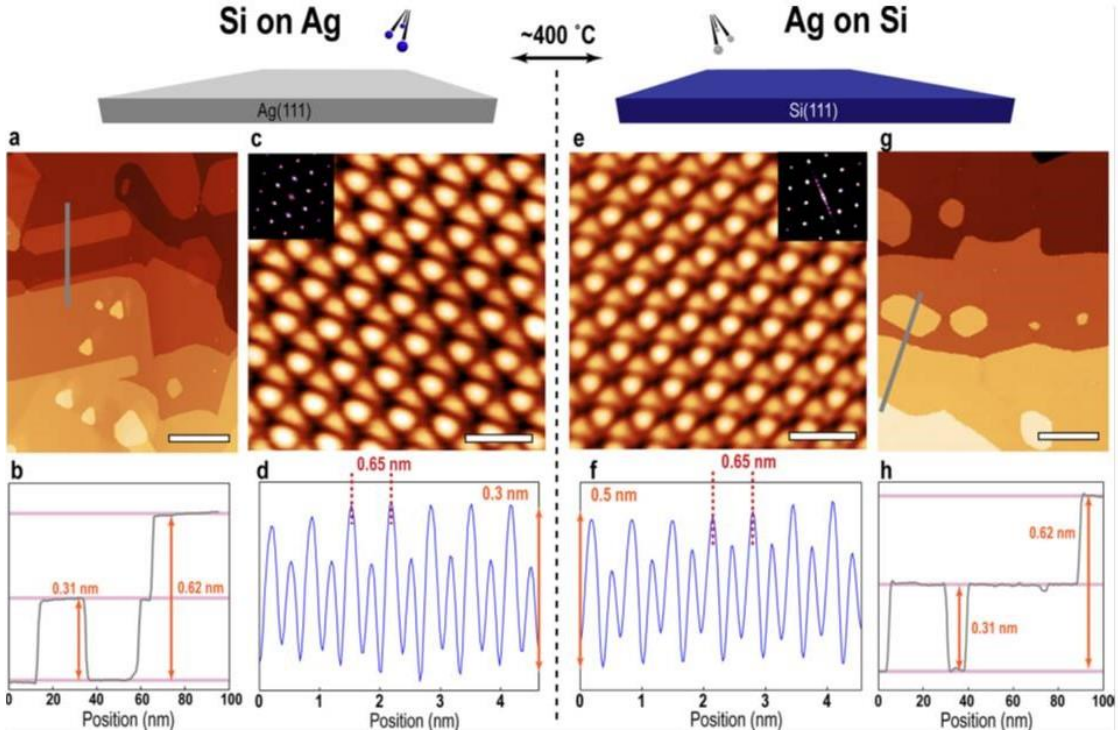

Fig. 1.7 (Top) Schematic illustrations for growth of Si on Ag(111) and Ag on Si(111). (a) STM topography of √3×√3 silicene (scale bar = 50 nm, V_{bias}= -1.0 V, I = 400 pA) with (b) line profile revealing a 0.31 nm step height. (c) Atomic-scale STM topography of the √3×√3 silicene with (d) line profile (scale bar = 1 nm, V_{bias} = 0.3 V, I = 1.0 nA). (e) Atomic-scale STM topography of the √3×√3 phase for Ag on Si(111) with (f) line profile (scale bar = 1 nm, V_{bias} = -1.0 V, I = 100 pA) revealing an indistinguishable lateral atomic periodicity compared to the V_{bias} = -1.0 V phase for Si on Ag(111) shown in part (d). (g) STM topography of the √3×√3 phase for Ag on Si(111) with (h) line profile (scale bar = 50 nm, V_{bias} = 0.85 V, I = 1.4 nA),

showing identical step heights and similar island shapes to the √3×√3 phase for Si on Ag(111) shown in part (a) [40].

A recent work by Mannix *et al* [40] claimed that √3×√3 silicene is structurally and electronically identical to the HCT mode on Si(111) substrate. As shown in Fig. 1.7, both √3×√3 silicene and √3×√3 Ag are honeycomb structures with a similar lattice constant around 0.65 nm and a monolayer around height of 0.31 nm in STM images, raising debate about the existence of √3×√3 silicene. On the other hand, clear evidence of the existence of multilayer silicene has been reported by a comprehensive x-ray crystallographic study, where multilayer silicene is effectively realized upon growth at rather low growth temperatures (∼200 ℃) [65]. Further work on the atomic structure of silicene, especially the √3×√3 phase, are urgently needed to clarify those novel physical and chemical properties explored on silicene.

1.2.6 Research motivation

Based on the literature review, this thesis is focused on research on (i) the atomic structure of silicene to illustrate the existence of silicene; (ii) *in-situ* Raman measurements to provide unambiguous, high-throughput, non-destructive identification of epitaxial silicene; (iii) the effects of oxygen adsorption on band-gap engineering of silicene; and (iv) realization of quasi-free-standing silicene layer through oxidization of bilayer silicene.

1.3 Outline of Chapters

Chapter 2 displays the STM technique, covering both the experimental and theoretical details that form our basic understanding of the recorded images. A brief introduction to molecular beam epitaxy (MBE), ARPES, and Raman spectroscopy are also included.

Chapter 3 presents the epitaxial growth mechanism of silicene layers deposited on Ag(111) surfaces by MBE deposition. Several kinds of defects are identified in different silicene superstructures, which are most likely induced by the low coverage effect and the structural mismatch between the silicene and the Ag(111) surface. Furthermore, the silicene sheet starts to emerge at a terrace edge of the substrate. Our results indicate that the growth mechanism of silicene follows the Stranski-Krastanov growth mode for all superstructures.

Chapter 4 reports on the special coupling between Dirac fermions and lattice vibrations, in other words, EPC, in silicene layers on the Ag(111) substrate surface, which was probed by *in-situ* Raman spectroscopy. The tensile strain, induced by the lattice mismatch between the silicene and the substrate, and the charge doping from the substrate, modulate the EPC strength. The Raman spectrum clearly reveals the evolution of defect peaks with growing coverage of silicene layers. The peaks at low frequency correspond to the different electron scattering modes occurring at the zigzag and armchair edges. This work implies that Raman spectroscopy allows unambiguous, fast, and nondestructive identification of silicene layers, which is critically lacking in this emerging research field so far.

A band gap that is tunable by oxygen adatoms from semimetallic to semiconducting type is introduced in Chapter 5. There are two critical factors for the band gap engineering, the adsorption configurations and the amounts of oxygen adatoms on the silicene surface, which is determined by the different degrees of buckling in different silicene superstructures. By using *in-situ* Raman spectroscopy as well as first-principles calculations, it is found that the Si-O-Si bonds are the most energy-favored cases formed on $\sqrt{13}\times\sqrt{13}$, 3×3, and $\sqrt{7}\times\sqrt{7}$ structures under oxidation. The silicene monolayers could retain their structures, even when fully covered by oxygen adatoms. This work demonstrates the feasibility of silicene for

band-gap modulation with oxygen adatoms, expeanding the base of available 2D electronic materials for devices with properties that are hard to achieve with graphene oxide.

Chapter 6 presents the hybridized electronic structures of epitaxial 3×3 silicene on Ag(111), which are characterized by STM and ARPES. A metallic surface state, resulting from the hybridization between Si and Ag, can gradually decay due to oxygen adsorption. X-ray photoemission spectroscopy confirms this decoupling of Si-Ag bonds, and the relatively high oxygen resistance of the Ag(111) surface compared with 3×3 silicene. The results confirmed experimentally and theoretically that the high chemical activity of 3×3 silicene is attributable to the Si p_z state.

Chapter 7 presents a quasi-free-standing silicene layer that has been successfully obtained through oxidization of bilayer silicene on the Ag(111) surface. The oxygen atoms intercalate into the underlayer of silicene, which can isolate the top layer of silicene from the substrate. In consequence, the top layer of silicene exhibits the signature of a 1×1 honeycomb lattice and hosts massless Dirac fermions due to much less interaction with the substrate. Furthermore, the oxidized silicon buffer layer is expected to serve as an ideal dielectric layer for electric gating in electronic devices. These findings are relevant for the future design and application of silicene-based nanoelectronic and spintronic devices

1. K. S. Novoselov, A. K. Geim, S. V. Morozov, D. Jiang, Y. Zhang, S. V. Dubonos, I. V. Grigorieva, and A. A. Firsov, Science **306**, 666 (2004).
2. B. J. Feng, Z. J. Ding, S. Meng, Y. G. Yao, X. Y. He, P. Cheng, L. Chen, and K. H. Wu, Nano Lett. **12**, 3507 (2012).

3. L. Meng, Y. L. Wang, L. Z. Zhang, S. X. Du, R. T. Wu, L. F. Li, Y. Zhang, G. Li, H. T. Zhou, W. A. Hofer, and H. J. Gao, Nano Lett. **13**, 685 (2013).
4. A. Fleurence, R. Friedlein, T. Ozaki, H. Kawai, Y. Wang, and Y. Yamada-Takamura, Phys. Rev. Lett. **108**, 245501 (2012).
5. J. F. Gao and J. J. Zhao, Sci. Rep. **2**, 861 (2012).
6. A. Kara, H. Enriquez, A. P. Seitsonen, L. C. Lew Yan Voon, S. Vizzini, B. Aufray, and H. Oughaddou, Surf. Sci. Rep. **67**, 1 (2012).
7. K. Watanabe, T. Takashi, and H. Kanda, Nat. Mater. **3**, 404 (2004).
8. G. Seifert, H. Terrones, M. Terrones, G. Jungnickel, and T. Frauenheim, Phys. Rev. Lett. **85**, 146 (2000).
9. D. Braga, I. G. Lezama, H. Berger, and A. F. Morpurgo, Nano Lett. **12**, 5218 (2012).
10. C. C. Liu, H. Jiang, and Y. G. Yao, Phys. Rev. B 84, 195430 (2011).
11. A. O'Hare, F. V. Kusmartsev, and K. I. Kugel, Nano Lett. **12**, 1045 (2012).
12. A. Resta, T. Leoni, C. Barth, A. Ranguis, C. Becker, T. Bruhn, P. Vogt, and G. Le Lay, Sci. Rep. **3**, 2399 (2013).
13. C. C. Liu, W. X. Feng, and Y. G. Yao, Phys. Rev. Lett. 107,076802 (2011).
14. P. Vogt, P. De Padova, C. Quaresima, J. Avila, E. Frantzeskakis, M. C. Asensio, A. Resta, B. Ealet, and G. Le Lay, Phys. Rev. Lett. **108**, 155501 (2012).
15. L. Chen, H. Li, B. J. Feng, Z. J. Ding, J. L. Qiu, P. Cheng, K. H. Wu, and S. Meng, Phys. Rev. Lett. **110**, 085504 (2013).
16. H. S. Liu, J. F. Gao, and J. J. Zhao, J. Phys. Chem. C **117**, 10353 (2013).
17. J. F. Gao, J. F. Zhang, H. S. Liu, Q. F. Zhang, and J. J. Zhao, Nanoscale **5**, 9785 (2013).
18. B. J. Feng, W. B. Li, J. L. Qiu, P. Cheng, L. Chen, and K. H. Wu, Chin. Phys. Lett. **32**, 037302 (2015).

19. Y. Feng, B. J. Feng, Z. J. Xie, W. B. Yi, X. Liu, D. F. Liu, L. Zhao, L. Chen, X. J. Zhou, and K. H. Wu, Chin. Phys. Lett. **31**, 127303 (2014).

20. H. S. Liu, N. N. Han, and J. J. Zhao, J. Phys.: Condens. Matter **26**, 475303 (2014).

21. L. Chen, C. C. Liu, B. J. Feng, X. Y. He, P. Cheng, Z. J. Ding, S. Meng, Y. G. Yao, and K. H. Wu, Phys. Rev. Lett. **109**, 056804 (2012).

22. C. C. Liu, W. X. Feng, and Y. G. Yao, Phys. Rev. Lett. **107**, 076802 (2011).

23. R. Quhe, R. X. Fei, Q. H. Liu, J. Zheng, H. Li, C. Xu, Z. Ni, Y. Wang, D. Yu, Z. Gao, and J. Lu, Sci. Rep. **2**, 853 (2012).

24. M. Ezawa, Phys. Rev. Lett. **109**, 055502 (2012).

25. M. Ezawa, Phys. Rev. Lett. **110**, 026603 (2013).

26. D. Chiappe, C. Grazianetti, G. Tallarida, M. Fanciulli, and A. Molle, Adv. Mater. **24**, 5088 (2012).

27. H. Enriquez, S. Vizzini, A. Kara, B. Lalmi, and H. Oughaddou, J. Phys.: Condens. Matter **24**, 314211 (2012).

28. H. Jamgotchian, Y. Colignon, N. Hamzaoui, B. Ealet, J. Y. Hoarau, B. Aufray, and J. P. Bibérian, J. Phys.: Condens. Matter **24**, 172001 (2012).

29. A. C. Ferrari and D. M. Basko, Nat. Nanotech. **8**, 235 (2013).

30. Z. Liu, K. Suenaga, P. J. F. Harris, and S. Iijima, Phys. Rev. Lett. **102**, 015501 (2009).

31. W. X. Li, C. Stampfl, and M. Scheffler, Phys. Rev. B. **65**, 075407 (2002).

32. K. Takeda and K. Shiraishi, Phys. Rev. B **50**, 14916 (1994).

33. C. L. Lin, R. Arafune, and K. Kawahara, Appl. Phys. Express **5**, 45802 (2012).

34. Y. Du, J. C. Zhuang, H. S. Liu, X. Xu, S. Eilers, K. H. Wu, P. Cheng, J. J. Zhao, X. D. Pi, K. W. See, G. Peleckis, X. L. Wang, and S. X. Dou, ACS Nano **8**, 10019 (2014).

35. B. Aufray, A. Kara, S. Vizzini, H. Oughaddou, C. Léandri, B. Ealet, and G. Le Lay, Appl. Phys. Lett. **96**, 183102 (2010).

36. M. R. Tchalala, H. Enriquez, A. J. Mayne, A. Kara, S. Roth, M. G. Silly, A. Bendounan, F. Sirotti, T. Greber, B. Aufray, G. Dujardin, M. Ait Ali, and H. Oughaddou, Appl. Phys. Lett. **102**, 083107 (2013).

37. J. L. Qiu, H. X. Fu, Y. Xu, A. I. Oreshkin, T. N. Shao, H. Li, S. Meng, L. Chen, and K. H. Wu, Phys. Rev. Lett. **114**, 126101 (2015).

38. R. Arafune. C. L. Lin, K. Kawahara, N. Tsukahara, E. Minamitani, Y. Kim, N. Takagi, and M. Kawai, Surf. Sci. **608**, 297 (2013).

39. T. Shirai, T. Shirasawa, T. Hirahara, N. Fukui, T. Takahashi, and S. Hasegawa, Phys. Rev. B **89**, 241403 (2014).

40. A. J. Mannix, B. Kiraly, B. L. Fisher, M. C. Hersam, and N. P. Guisinger, ACS Nano **8**, 7538 (2014).

41. J. G. Feng, S. R. Wagner, and P. P. Zhang, Sci. Rep. **5**, 10310 (2015).

42. Z. L. Liu, M. X. Wang, J. P. Xu, J. F. Ge, G. Le. Lay, P. Vogt, D. Qian, C. L. Gao, C. H. Liu, and J. F. Jia, New J. Phys. **16**, 075006 (2014).

43. N. B. Kopnin and E. B. Sonin, Phys. Rev. Lett. **100**, 246808 (2008).

44. E. Scalise, M. Houssa, G. Pourtois, B. Van den Broek, V. Afanas'ev, and A. Stesmans, Nano Res. **6**, 19 (2013).

45. P. De Padova, C. Ottaviani, C. Quaresima, B. Olivieri, P. Imperatori, E. Salomon, T. Angot, L. Quagliano, C. Romano, A. Vona, M. Muniz-Miranda, A. Generosi, B. Paci, and G. Le Lay, 2D Mater. **1**, 021003 (2014).

46. A. Molle, C. Grazianetti, D. Chiappe, E. Cinquanata, E. Cianci, G. Tallarida, and M. Fanciulli, Adv. Funct. Mater. **23**, 4340 (2013).

47. E. Cinquata, E. Scalise, D. Chiappe, C. Grazianetti, B. van den Broek, M. Houssa, M. Fanciulli, and A. Molle, J. Phys. Chem. C **117**, 16719 (2013).

48. G. G. Guzmán-Verri and L. C. Lew Yan Voon, Phys. Rev. B **76**, 075131 (2007).

49. S. Cahangirov, M. Topsakal, E. Aktürk, H. Şahin, and S. Ciraci, Phys. Rev. Lett. **102**, 236804 (2009).

50. S. Lebègue and O. Eriksson, Phys. Rev. B **79**, 115409 (2009).

51. C. L. Lin, R. Arafune, K. Kawahara, M. Kanno, N. Tsukahara, E. Minamitani, Y. Kim, M. Kawai, and N. Takagi, Phys. Rev. Lett. **110**, 076801 (2013).

52. D. Tsoutsou, E. Xenogiannopoulou, E. Golias, P. Tsipas, and A. Dimoulas, Appl. Phys. Lett. **103**, 231604 (2013).

53. X. Xu, J. C. Zhuang, Y. Du, H. F. Feng, N. Zhang, C. Liu, T. Lei, J. O. Wang, M. Spencer, T. Morishita, X. L. Wang, and S. X. Dou, Sci. Rep. **4**, 7543 (2014).

54. J. Avila, P. De Padova, S. Cho, I. Colambo, S. Lorcy, C. Quaresima, P. Vogt, A. Resta, G. Le Lay, and M. C. Asensio, J. Phys.: Condens. Matter **25**, 262001 (2013).

55. P. De Padova, P. Vogt, A. Resta, J. Avila, I. Razado-Colambo, C. Quaresima, C. Ottaviani, B. Olivieri, T. Bruhn, T. Hirahara, T. Shirai, S. Hasegawa, M. C. Asensio, and G. Le Lay, Appl. Phys. Lett. **102**, 163106 (2013).

56. P. De Padova, J. Avila, A. Resta, I. Razado-Colambo, C. Quaresima, C. Ottaviani, B. Olivieri, T. Bruhn, P. Vogt, M. C. Asensio, and G. Le Lay, J. Phys.: Condens. Matter **25**, 382202 (2013).

57. J. C. Zhuang, X. Xu, Y. Du, K. H. Wu, L. Chen, W. C. Hao, J. O. Wang, W. K. Yeoh, X. L. Wang, and S. X. Dou, Phys. Rev. B **91**, 161409 (2015).

58. B. J. Feng, H. Li, C. C. Liu, T. N. Shao, P. Cheng, Y. G. Yao, S. Meng, L. Chen, and K. H. Wu, ACS Nano **7**, 9049 (2013).

59. J. O. Sofo, A. S. Chaudhari, and G. D. Barber, Phys. Rev. B **75**, 153401 (2007).

60. D. C. Elias, R. R. Nair, T. M. G. Mohiuddin, S. V. Morozov, P. Blake, M. P. Halsall, A. C. Ferrari, D. W. Boukhvalov, M. O. Katsnelson, A. K. Geim, and K. S. Novoselov. Science **323**, 610 (2009).

61. R. Balog, B. Jørgensen, L. Nilsson, M. Andersen, E. Rienks, M. Bianchi, M. Fanetti, E. Lægsgaard, A. Baraldi, S. Lizzit, Z. Sljivancanin, F. Besenbacher, B. Hammer, T. G. Pedersen, P. Hofmann, and L. Hornekær, Nat. Mater. **9**, 315 (2010).
62. T. Andreev, I. Barke, and H. Hövel, Phys. Rev. B **70**, 205426 (2004).
63. H. M. Zhang, J. B. Gustafsson, and L. S. O. Johansson, Phys. Rev. B **74**, 201304 (2006).
64. N. Sato, T. Nagao, and S. Hasegawa, Surf. Sci. **442**, 65 (1999).
65. P. De Padova, A. Generosi, B. Paci, C. Ottaviani, C. Quaresima, B. Olivieri, E. Salomon, T. Angot, and G. Le Lay, 2D Mater. **3**, 031011 (2016).

CHAPTER 2

EXPERIMENTAL TECHNIQUES

The research in this thesis was conducted in a system comprising UHV-MBE-STM-Raman techniques or UHV-MBE-ARPES techniques. Thus, this chapter will briefly introduce these techniques, including: UHV, MBE, STM and STS, Raman, and ARPES spectroscopy.

2.1 UHV technique

In order to prevent contamination from molecular impurities, the samples need to be under a UHV system. UHV (~10^{-10} Torr) could be obtained by a series of vacuum pumps, which are devices that remove gas molecules from a sealed volume by mechanical methods, phisical methods, and chemical methods, in order to leave behind a partial vacuum. The most frequently-used vacuum pumps are mechanical pumps, turbomolecular pumps, sputter ion pumps, and titanium sublimation pumps. The first two types of pumps belong to the gas bleeding type, from which high vacuum could be obtained, and the last two pumps are classified as reaction of residual gas type, which can realize and maintain the UHV.

There is a balance between the pumping effect of the pump and the gas leakage/release. Thus, the limitation of the pressure is not the limitation of the pump. There are four kinds of source for the gas leakage/release: (1) Gas is released from the surfaces of chamber walls or accessories. (2) Gas dissolved in the body of the chamber or accessories could be redistributed to the surface with increasing temperature. (3) Gas permeates into the chamber from the atomsphere due to the pressure difference between the UHV in chamber and the ordinary pressure outside the chamber. This permeation will be intensively enhanced when the chamber wall is very thin. (4) The vapor pressure of some materials, such as normal metal, glass, and quatz, is low and does not affect the UHV. Materials with high saturated vapor

pressure, however, such as brass, lastics, and nylon, should not be used in UHV chamber. Thus, the most frequently-used material for chamber walls is 304 stainless steel with the properties of high corrosion resistance, good workability, and low gas permeation. The temperature of chamber pariete could be 150 ˚C in the baking process, accelerating the gas redistribution and release.

2.2 MBE technique

MBE is an epitaxy method performed under UHV by heating a source oven to deposit individual molecules on the surface of the substrate. The molecules will arrange themselves in the epitaxial growth mode, consisting of adsorption, transference, and reaction at the surface. The MBE technique is one of the most widely used methods to fabricate semiconductor films. In contrast to other epitaxy techniques, the MBE technique is a growth process that is essentially unbalanced between the kinetics and the thermodynamics, where the gas phase atoms form solid phase atoms during the deposition process.

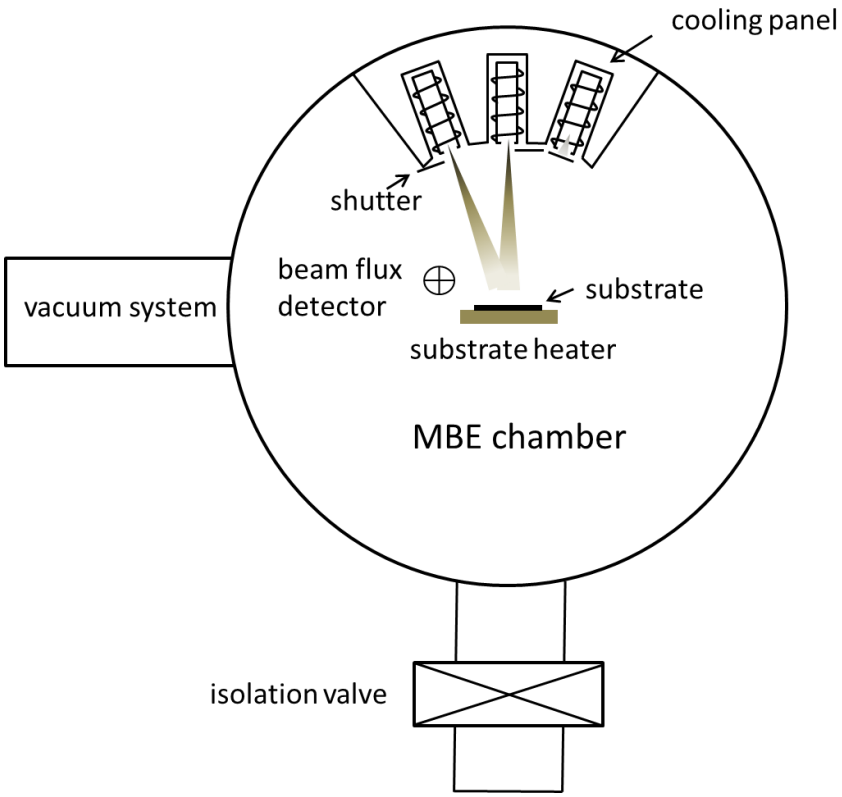

Fig. 2.1 Schematic diagram of MBE chamber.

Figure 2.1 displays a schematic diagram of a typical MBE system, including the source oven, shutter, beam flux detector, and cooling panel. The introduction of liquid nitrogen (LN_2) could improve the vacuum and reduce the effect of impurities.

As one of the most important components of the MBE chamber, the source ovens for a commercial MBE system are usually Knudsen Diffusion Cell (K-Cells). Each one is made up of a crucible, shutter, heater, heat shield screen, thermocouple, and cooling water. The crucible is used to store the materials for growth, and is generally composed of pyrolytic boron nitride or Al_2O_3. The heater for the crucible is tungsten filament. There is a heat shield screen made of tantalum film surrounding the crucible, contributing to uniform heating for the crucible and less thermal energy loss. The shutter in front of the crucible is used to accurately control the growth time. The thermocouple is the tool used to detect the

temperature of crucible. Furthermore, a circulating cooling water system is added to the K-Cell source oven, decreasing the heat irradiation to the environment and improving the UHV. Several source ovens could be installed together in the chamber to realize multi-elemental co-deposition.

A home-made simple source oven could be used for the samples that do not need accurate growth control. The material used for such a source oven is tantalum film in the shape of boat. The materials used in this kind of source oven contain Ag, Fe, Cu, Cr, *etc*. The Si source used in this thesis is connected directly to the two current electrodes of a home-made simple source oven. A leak valve is suitable for materials that are in the form of liquid or gas at room temperature, for example, the oxygen used in this work. For the alkalis or alkaline-earth metals, such as Cs, K, Na, Rb, and Li, their compound froms are applied in SAES Getters, because their elementary substances are easily oxidized.

Compared with other epitaxial growth methods, the priorities of MBE could be summarized as follows:

(1) The fabricated samples are high purity due to the fact that the process is operated under UHV.

(2) The accuracy of the film can reach the atomic level. The growth rate is around 0.1 monolayer to 10 monolayers per second, and the thickness can be controlled by the shutters.

(3) The low substrate temperature is beneficial for the weak diffusion of atoms between the substrate and the epitaxial film, leading to the absence of defects caused by high temperature.

(4) Because the MBE growth is in an unbalanced condition, this method could synthesize the films which are hard to obtain by the usual methods in the condition of thermal balance.

2.3 STM technique

STM was first explored in 1982 by Gerd Binnig and Heinrich Rohrer [1,2]. It is a unique and powerful means of investigation in surface science and has become the technique of choice for revealing the characteristics of a wide variety of surfaces at the atomic level. The design of STM technique on surface science was acknowledged in 1986 when the inventors received the Nobel Prize.

2.3.1 The principle of STM

The working principle of the STM is rather simple. A sharp metallic tip is brought into close proximity to the surface of a conducting sample, so that the wave functions of tip and the sample will start to overlap, enabling an exchange of electrons in the classically forbidden vacuum gap between the tip and the surface. The typical distance for this quantum mechanical tunneling phenomenon is ~5 Å. If a positive bias voltage is applied to the sample, electrons will start to tunnel from the filled tip states to the empty sample states or vice versa. The net flow of electrons results in a measurable tunnel current, which is in the nanoampere range and strongly dependent on the distance between the tip and the sample, due to the exponential decay of the electronic wave functions into the vacuum gap. If the tip is attached to a scanner tube made of a piezoelectric material, it is possible in practice to control the position of the tip in the sub-Ångstrøm range, making the STM capable of creating atomically resolved images of surfaces.

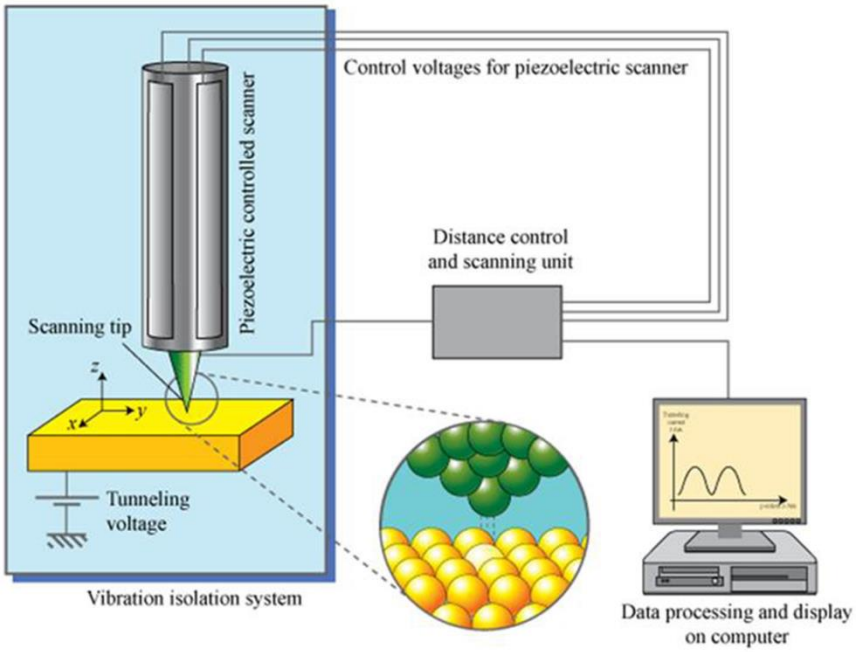

Figure 2.2 Illustration of the principle of STM.

STM imaging is usually conducted in the so-called constant current mode, in which a feedback loop adjusts the distance between the tip and the surface to keep the current constant at a preset value while the tip is raster scanned across the surface at a fixed bias voltage. When the tip traverses a protrusion, the feedback loop will move the tip away from the surface. When the tip has moved across the protrusion, the feedback loop will bring the tip closer to the surface. The height position of the tip could be recorded as a function of the lateral position of the tip, making a topographic image of the surface. It should be noted that the constant current STM images are also affected by the local density of states at the Fermi level projected to the position of the tip apex. Therefore, the images in general reflect a convolution of the geometric and electronic structure of the surface. The operational principle is illustrated in Fig. 2.2.

2.3.2 Theory of STM

In order to obtain a precise interpretation of STM images, it is important to know the factors

determining the tunnel current. This is a convoluted task because a complete modeling of the tunnel current requires detailed knowledge about the exact geometric and electronic states of both the tip and the surface. Thus, a simple one-dimensional model will be introduced to explain the tunneling and thus STM imaging.

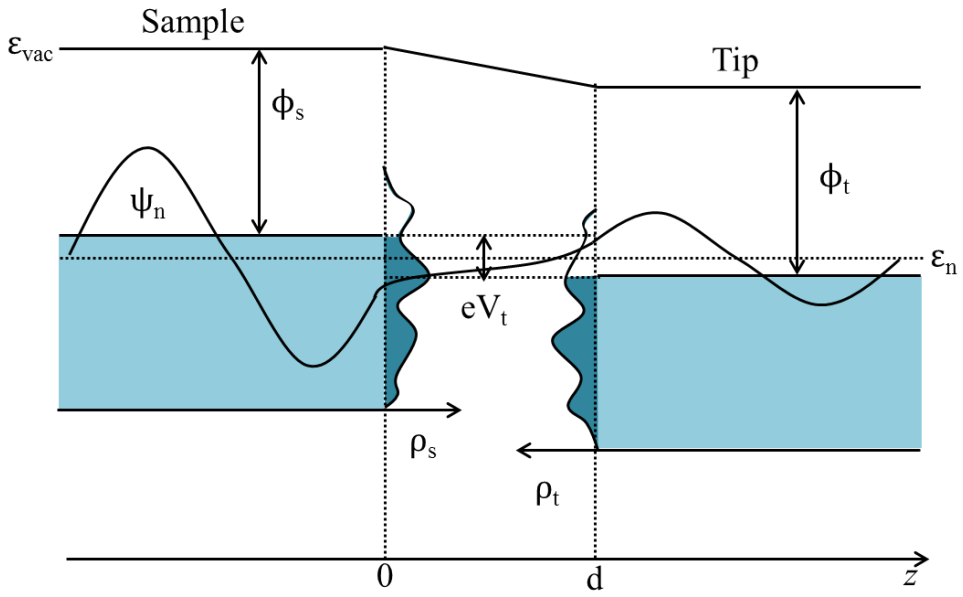

Fig. 2.3 Schematic diagram of an electron tunnel junction with a width *d*. A negative bias voltage, V_t, is applied to the sample. ϕ_s and ϕ_t are the work function of the sample and tip, respectively. ρ_s and ρ_t are the densities of states of the sample and tip, respectively. ψ_n is the wave function with energy ε_n that decays exponentially in the junction. ε_{vac} is the vacuum energy, and ε_F is the Fermi energy of the sample.

The vacuum gap can be replaced by a constant potential barrier, $U(z)$, in the region $0 < z < d$, in a simple one-dimensional model. The Schrödinger equation describing an electron with energy $\varepsilon < U(z)$ moving along the $+z$ direction in the classically forbidden region could be written as:

$$-\frac{\hbar^2}{2m_e}\frac{d^2}{dz^2}\psi(z) + U(z)\psi(z) = \varepsilon\psi(z) \tag{2.1}$$

where

$$\psi(z) = \psi(0)e^{-\kappa z} \tag{2.2}$$

is the wave function of the electron, and $\kappa = \sqrt{2m_e(U-\varepsilon)}/\hbar$ is the attenuation constant, with m_e the mass of the electron. The probability *w* of an electron emerging at the position *z* = d is:

$$w \propto |\psi(\mathrm{d})|^2 = |\psi(0)|^2 e^{-2\kappa \mathrm{d}} \tag{2.3}$$

This exponential decay in the barrier region is illustrated in Fig. 2.3. The tunnel current is directly proportional to the total number of sample states within the energy interval eV_t, leading to:

$$I_t \propto \sum_{\varepsilon_n=\varepsilon_F-eV_t}^{\varepsilon_F} |\psi_n(\mathrm{d})|^2 \tag{2.4}$$

If the density of states (DOS) does not vary significantly with the interval, Equation 2.4 could be expressed as:

$$I_t \propto V_t \rho_s(z=\mathrm{d}, \varepsilon_F) = V_t \rho_s(z=0, \varepsilon_F) e^{-\frac{2}{\hbar}\sqrt{2m_e\phi}\mathrm{d}} \tag{2.5}$$

Thus, the constant current STM image reflects the contours of the constant local DOS at the Fermi level and at the position of the tip.

2.3.2 Theory of STS

Another application of the STM is scanning tunnelling spectroscopy (STS). In fact, the original idea of building the STM was not to build a microscope, but rather to perform spectroscopy locally on an area less than 10 nm in diameter [2].

The concept of the STS technique follows from Equation 2.5. The equation implies that if the

DOS of the tip is constant, so the conductance (I/V) plotted as a function of V reflects the LDOS of the surface. According to the perturbation theory suggested by J. Bardeen, the tunnel current could be described as:

$$I_t \propto \int_0^{eV} \rho_s(\varepsilon_F - eV + \varepsilon)\, \rho_t(\varepsilon_F + \varepsilon) d\varepsilon \tag{2.6}$$

This equation implies that the tunnel current is determined by the integration of DOS of the two subsystems. Because the ρ_t of metallic tip is generally treated as a constant, differentiation of Equation 2.6 gives as:

$$\frac{dI}{dV} \propto \rho_s(\varepsilon_F - eV) \tag{2.7}$$

Thus, $\frac{dI}{dV}$ reflects the local density of states of the sample surface.

2.4 *In-situ* Raman technique

Our *in-situ* Raman technique is actually based on part of a tip-enhanced Raman spectroscope (TERS) system. For TERS, the light of the laser used in the scattering experiment has to be focused onto the tip-sample junction and the scattered light has to be collected and analysed by a spectrograph, while for *in-situ* Raman spectroscopy, we need to focus the laser on the surface of the sample. The illuminating laser and the spectrograph are placed outside the chamber. The laser beam has thus to be guided into the UHV chamber and the scattered light guided out of the chamber to the spectrograph, as shown in the schematic diagram in Fig. 2.4(a). The laser can be focused by the incident lens, and the optical image can be collected through the observation lens. The Raman signal is reflected back and is collected by a spectrometer which is attached to the incident lens.

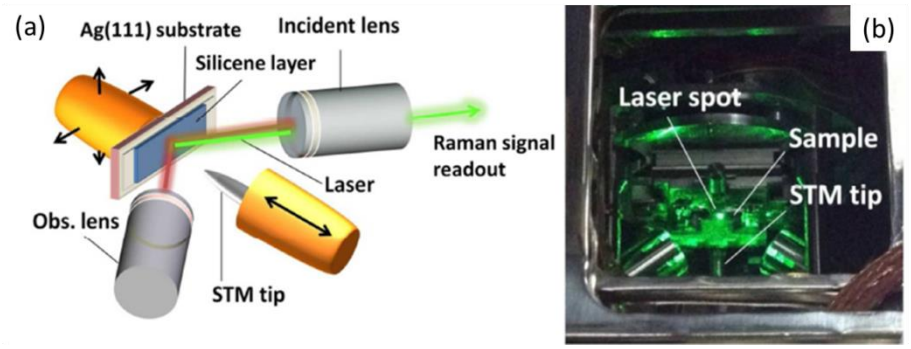

Figure 2.4 (a) Schematic diagram of the low temperature STM system equipped with a Raman attachment that was used in this study. The incident laser is introduced by an incident lens. The laser can be focused by the incident lens, and the optical image can be collected through the observation lens (indicated as Obs. lens in the diagram). The Raman signal is reflected back and is collected by spectrometer which is attached to the incident lens. (b) Actual photograph of the Raman measurement setup in the STM UHV chamber.

A Nd:YAG laser with 532 nm wavelength and a power of about 25 mW was used as the light source, and was positioned outside the chamber on an optical table. The objective lens unit was an aspherical lens driven by xyz-axes piezo actuator. The laser defines the starting point of the optical path through the whole set-up. The endpoint is a spectrograph located outside the UHV chamber, a Raman optical unit (Nanofinder FLEX), an imaging spectrometer, and a cooled CCD detector. The polarization of the incident light could be controlled manually by waveplate and prism in the Nanofinder FLEX.

2.5 ARPES technique

The spectral function provided by ARPES [3] is a fundamental quantity in many-body physics that provides energy and momentum space information about the occupied and unoccupied single-particle states. Thus, ARPES is a useful tool for detecting the electronic structure of materials, and has shed light on the physics of many important materials,

including two-dimensional graphene. Combined with X-ray photoelectron spectroscopy (XPS), ARPES makes use of the photoelectric effect.

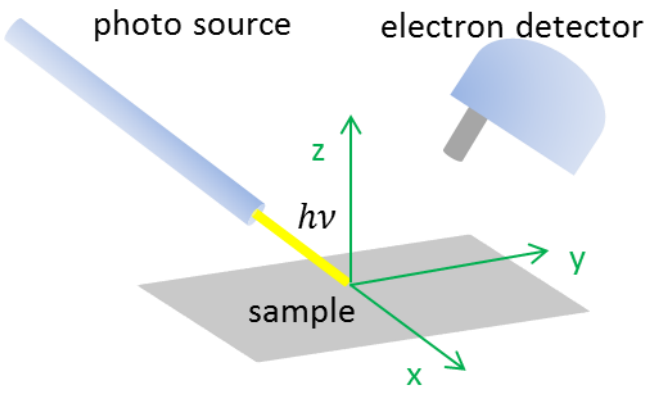

Figure 2.5 Schematic diagram of ARPES measurements.

Figure 2.5 illustrates the layout of the ARPES measurements. The basic principle behind ARPES, the energy conservation law, is described by the Einstein equation:

$$E_{kin} = h\upsilon - E_B - \Phi_{sample} \tag{2.8}$$

where E_{kin} is the kinetic energy of the emitted electrons above vacuum level, E_B corresponds to the electron binding energy difference relative to the Fermi level, and Φ_{sample} is the work function of the sample.

In addition to energy conservation, the law of conservation of momentum is also relevant to the photoemission process as follows [3]:

$$\hbar k_i = \hbar k_f = \sqrt{2mE_f}\sin\theta \tag{2.9}$$

Here, k_i and k_f refer to the initial and outgoing electros momentum, respectively. Thus, combined with the momentum data collected by the ARPES detector, we are able to distinguish the momentum of the electrons inside the solid, in the plane parallel to the surface

of the solid. For two-dimensional materials such as graphene, we can neglect the momentum along the perpendicular direction which simplifies the analysis process [4-6]. By applying both momentum and energy conservation, information about the electron initial momentum and its energy, as well as the underlying electronic structure could be deduced.

The typical set-up for photoemission spectroscopy measurements comprises a light beam, an electron energy analyser, and a data collection system. High soft X-ray photon energies are used in XPS to study core-level excitations (100-2000 eV) and to discriminate the surface states from the bulk states. During the measurement, the sample to be analysed is placed in a vacuum chamber and irradiated with photons lying in the X-ray energy range.

1. G. Binning, H. Rohrer, C. Gerber, and E. Weibel, Phys. Rev. Lett. **49**, 57 (1982).
2. G. Binning, and H. Rohrer, Rev. Mod. Phys. **59**, 615 (1987).
3. J. Braun, Rep. Prog. Phys. **59**, 1267 (1996).
4. A. Bostwick, T. Ohta, T. Seyller, K. Horn, and E. Rotenberg, Nat. Phys. **3**, 36 (2007).
5. S. Y. Zhou, G. H. Gwen, A. V. Fedorov, P. N. First, W. A. de Heer, D. H. Lee, F. Guinea, A. H. Castro Neto, and A. Lanzara, Nat. Mater. **6**, 770 (2007).
6. B. Feuerbacher, B. Fitton, and R F Willis (ed) Photoemission and Electronic Properties of Surfaces (1978).

CHAPTER 3

EPITAXIAL GROWTH MECHANISM OF SILICENE ON AG(111)

The epitaxial growth mechanism of silicene layers fabricated on a Ag(111) surface by MBE deposition is reported in this chapter. The coverage effect and the structural defects have been identified by using STM imaging. It was found that the substrate temperature plays a critical role in determination of the silicene superstructures. Several types of defects are observed in different silicene superstructures, which are most likely induced by the low coverage effect or by interface lattice mismatch between silicene and Ag(111). Furthermore, the silicene sheet prefers to initially arise at the terrace edge of the substrate. Our results imply that the growth mechanism of all silicene superstructures follows the terraces growth mode mode.

3.1 Introduction

Due to their unique nanostructures and electronic states, 2D materials play a crucial role in innovative concepts and pioneering applications. Recently, a novel silicon-based 2D material, namely, silicene, has attracted extensive interest because it is an ideal candidate material for promising applications in electronics, photonics, and other related regions [1-3]. The theoretical simulations predict that silicene possesses a similar electronic band structure to graphene, in other words, silicene is a new massless Dirac Fermion system [4,5], which has been experimentally proved by both STS results and APRES measurements [6,7]. Silicene shows a large spin-orbit coupling (SOC), which allows the emergence of a large energy gap at the Dirac points and results in a detectable QSHE, as well as inherent compatibility with the current semiconductor industry [5-9]. In addition, unlike graphene sheets, the surfaces of which are chemically inert, the Si atoms in silicene sheets possess high chemical activity, which allows potential modulation of their physical, chemical and electronic properties by chemical fictionalization [10]. Although it has been proposed that the substrate temperature

and the surface coverage play the most crucial roles in the determination of silicene superstructures [1], there are few reports on the growth mechanism and the origin of the defects in epitaxial silicene, knowledge of which is highly important before fabrication of large-scale high-quality silicene nanosheets for applications.

In this work, we have studied the epitaxial growth mechanism in silicene with different superstructures. Single and multiple layered silicene sheets were obtained. Out results imply that the silicene sheets preferentially grow from the terrace edges of the Ag(111) silver substrate following the SK growth mode.

3.2 Experiments and methods

All samples used in this work were prepared in the preparation chamber of a low-temperature scanning tunneling microscopy system (LT-STM) (SNOM1400, Unisoku Co.). A clean Ag(111) substrate was prepared by argon ion sputtering and subsequent annealing at 550 ℃ under Ar atmosphere at the pressure (P) of 5×10^{-5} Torr for 3-5 cycles. The silicene monolayers were fabricated by the evaporation of silicon from a heated silicon wafer. The deposition flux was 0.08 monolayers per minute (ML/min). The temperature of the Ag(111) substrate was 450 K, 500 K, and 550 K for the formation of $\sqrt{13}\times\sqrt{13}$, 4×4, and $2\sqrt{3}\times2\sqrt{3}$ phases, respectively. The STM measurements were carried out in UHV ($P < 8\times10^{-11}$ torr) at room temperature. Before STM measurements, the Pt/Ir tip was calibrated on a silver surface on the Si(111) substrate.

3.3 Results and discussion

Figure 3.1 presents STM images of silicene nanosheets with different phases, namely, $\sqrt{13}\times\sqrt{13}$, 4×4, and $2\sqrt{3}\times2\sqrt{3}$ (with respect to Ag(111)). When the substrate temperature is less than 450 K, an amorphous silicon film is detected on the Ag(111) substrate, as shown in Fig. 3.1 (a). When the substrate temperature is between 450 K and 520 K, it is found that $\sqrt{13}\times\sqrt{13}$ phase with close-packed protrusions and the 4×4 phase always coexists over a large area of the silver surface, as shown in Fig. 3.1 (b), indicating the similar formation energies of these two phases. Furthermore, the same periodicity of the two phases (~1.16 nm) is also a vital factor in the coexistence of the two phases. When the substrate temperature is increased above 520 K, the $2\sqrt{3}\times2\sqrt{3}$ phase forms with traces of 4×4 phase. Pure $2\sqrt{3}\times2\sqrt{3}$ phase silicene could be obtained when the substrate temperature is higher than 550 K. A well spread moiré pattern with long-range order over the whole $2\sqrt{3}\times2\sqrt{3}$ silicene surface is shown in Fig. 3.1 (c), which is induced by the lattice mismatch between $2\sqrt{3}\times2\sqrt{3}$ silicene and the Ag(111) substrate. The angle between the orientation of the honeycomb structure and the direction of the moiré pattern is around 30 º, consistent with previous reports [1].

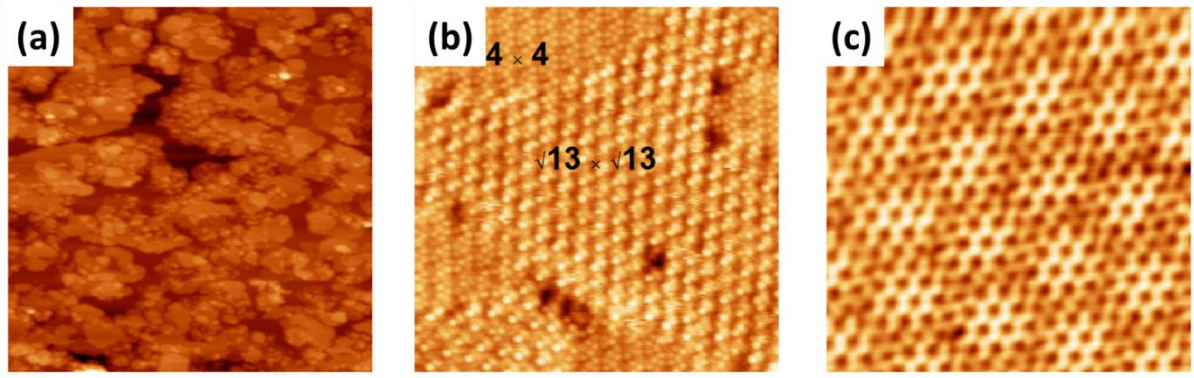

Fig. 3.1 (a) STM topographic image of amorphous layer (scanning area 16 nm×16 nm, V_{bias} = 2.0 V, I = 0.1 nA). (b) STM topographic image of two major phases of silicene, $\sqrt{13}\times\sqrt{13}$ and 4×4, in different domains of the sample as labeled. (scanning area 16 nm×16 nm, V_{bias} = -0.4 V, I = 5 nA). (c) STM images of $2\sqrt{3}\times2\sqrt{3}$ phases of silicene (scanning area 16 nm×16 nm, V_{bias} = -0.8 V, I = 1.5 nA).

Several kinds of defect are observed in different silicene superstructures. Figure 3.2 (a)

displays an STM image of unordered stripes among the bright atoms. These stripe-like defects are caused by grain boundaries between the √13×√13-I and √13×√13-II phases, which possess different atomic structures [11]. The topographic triangle defect, labeled by the green arrows, is observed in the 4×4 phase in Fig. 3.2 (b). This triangle defect, which only appears in the 4×4 phase rather than in the √13×√13 and 2√3×2√3 phases, forms due to the fact that the otherwise perfect honeycomb structure has a deficiency of several atoms in the top layer, as is verified by the STM images. This is attributed to the particular characteristics of 4×4 silicene sheet, which has more Si atoms in the top layer and less average binding energy with the substrate per silicon atom compared with the √13×√13 phase and 2√3×2√3 phase [11]. The high-resolution STM image in Fig. 3.2 (c) displays complete honeycomb rings with a periodic lattice in the bright part of the moiré pattern, but rather defective and distorted rings in the dark region of the moiré pattern. Such a phenomenon has been attributed to the lattice mismatch between the silicene sheet and the silver substrate by DFT simulations [3]. Silicon atoms in the bright part of the moiré pattern have a samll deviation from the positions of the Ag(111) atoms, resulting in a structure that is stable enough to keep its honeycomb rings. The large deviation in the dark part of the moiré pattern gives rise to the an unstable structure and eventually breaks the rings.

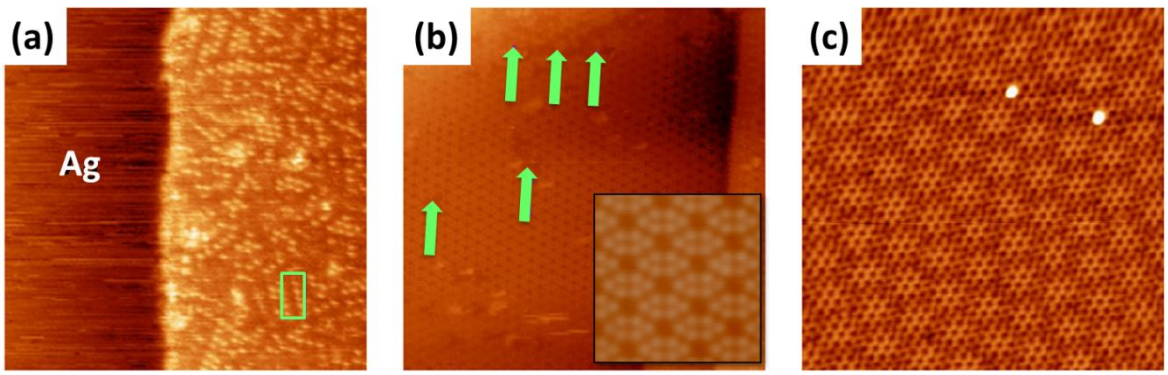

Fig. 3.2 STM images of (a) √13×√13 phase of silicene with stripe-like defects, as labeled by the green rectangle (scanning area 32 nm×32 nm, V_{bias} = -1.2 V, I = 0.8 nA), (b) 4×4 phase of silicene with triangle

phase (scanning area 32 nm×32 nm, V_{bias} = -0.8 V, I = 0.5 nA), (c) 2√3×2√3 phase of silicene with distortion (scanning area 32 nm×32 nm, V_{bias} = -0.8 V, I = 1.5 nA) on Ag(111). The green arrows in (b) label the positions of triangle defects. The inset of (b) shows an enlarged view of the 4×4 phase of silicene.

The Si coverage needed to be tuned in order to investigate the growth mechanism of multi-layer silicene. Topographic images of the amorphous Si and the √13×√13 phase in the submonolayer are shown in Fig. 3.3 (a) and 3.3 (b), respectively. Figure 3 displays clearly that both amorphous Si and the √13×√13 superstructure are grown from a terrace edge of the silver substrate. When the coverage of silicene is more than 1 monolayer (ML), a second layer is formed on the top of the first layer silicene in the form of an island. These islands are also preferentially to be located on the terrace edges of the silver substrate. The inset of Fig. 3.3 (c) shows an enlarged view of the second layer. A new superstructure with a smaller lattice parameter is observed for the second layer in the nanosheets. A more detailed structural analysis will be presented in the Chapter 4. It should be noted that there is no trace of continuity between the first layer and the second layer, demonstrating that the second layer grows after the first layer film has completely covered the silver substrate.

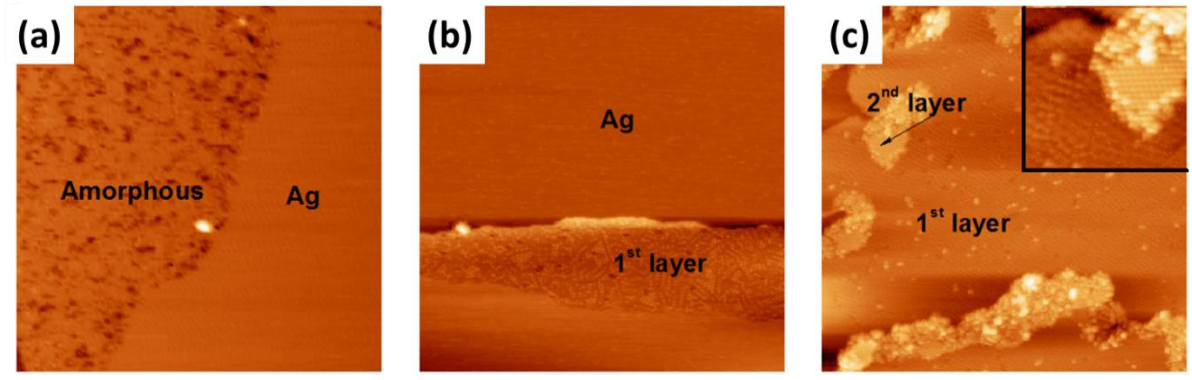

Fig. 3.3 (a) STM image of amorphous Si film (scanning area 80 nm×80 nm, V_{bias} = -1.2 V, I = 0.5 nA). (b) STM image of √13×√13 phase of silicene (scanning area 80 nm×80 nm, V_{bias} = -1.0 V, I = 0.5 nA). (c) STM image of second layer of silicene (scanning area 80 nm×80 nm, V_{bias} = -1.2 V, I = 0.1 nA). The inset of (c) is an enlarged view of the second layer (scanning area 16 nm×16 nm, V_{bias} = -1.2 V, I = 0.1 nA).

There are three epitaxial modes of thin film growth: the Volmer-Weber (VW) mode, the Frank-van der Merwe (FM) mode, and the terraces growth mode. We now introduce several thermodynamic parameters, surface energy of the substrate $\gamma_{substrate}$, surface energy of the outlayer (epitaxial film) $\gamma_{outlayer}$, and interface energy $\gamma_{interlayer}$. $\Delta\gamma$ is defined as: $\Delta\gamma = \gamma_{substrate} - \gamma_{outlayer} - \gamma_{interlayer}$, which determines the growth mode from the viewpoint of thermodynamics [12]. As shown in Fig. 3.4 (a), in the VW growth mode, where $\Delta\gamma \leq 0$ and the lattice mismatch is large between the substrate and the epitaxial film, the films form in three dimensional adatom clusters or islands and cause rough multi-layer structures on the substrate surface, preventing the formation of atomic bonds. For the FM growth mode, $\Delta\gamma \geq 0$ and the atomic bonds form due to the small lattice mismatch between the substrate and the epitaxial film, as shown in Fig. 3.4 (b). In this case, a 2D layer-by-layer growth mode leads to complete film formation prior to the growth of subsequent layers. The terraces growth mode (Fig. 3.4 (c)) is an intermediate process between 2D layer and 3D island growth. In this case, $\Delta\gamma \geq 0$ while lattice mismatch between the substrate and the epitaxial film is large. Thus, the film will first follow the FW mode, and although the strain increases with increasing film thickness. The growth mode changes from the FW mode to the VW mode to release the strain when the thickness reaches a critical value, which depends strongly on the chemical and physical properties. Based on the observation of both complete coverage by the first layer and the fact that amorphous islands and the $\sqrt{13}\times\sqrt{13}$ phase coexist in the second layer, it can be concluded that the silicene growth mechanism belongs to the terraces growth mode, and that the critical layer for the transition from the 2D mode to the 3D model is 1 ML. Furthermore, the lattice parameter of second layer superstructure displays an obvious variation, consistent with the prediction that strain will be released in terraces growth mode.

There is another growth method, namely, van der Waals epitaxy, for the growth of heterojunctions with large lattice mismatch [13,14]. Due to the fact that the length and direction of covalent bonds are hard to change, substrates with covalent dangling bonds on the surface are suitable for the deposition of materials with small lattice mismatch. A buffer layer could be deposited on the substrate with ionic bonds on the surface to gradually vary the lattice parameter. When the substrate is a layered material without dangling bonds, the interaction between the substrate and the film is the van der Waals interaction, where the strain induced by lattice mismatch could be totally released. This method is the so-called van der Waals epitaxy, which has been identified in the growth of graphene [15].

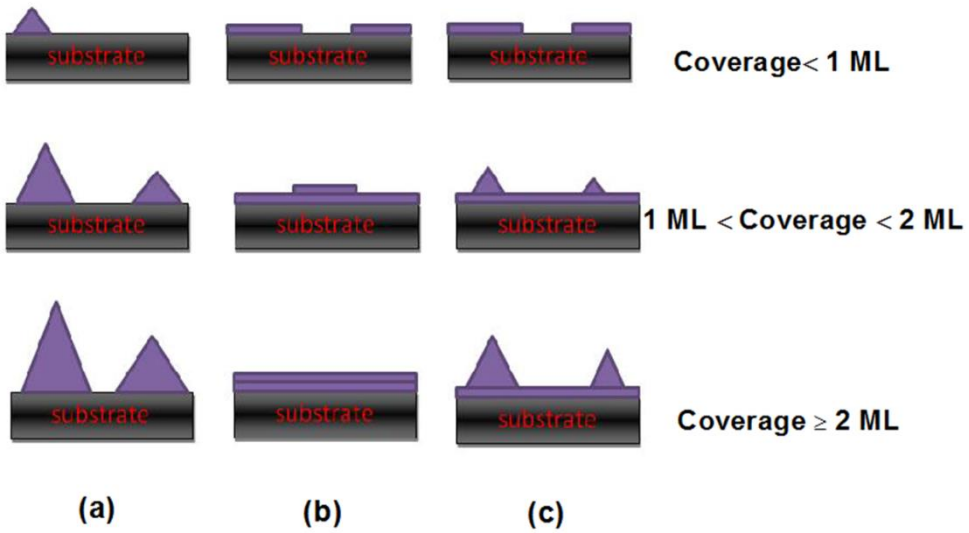

Fig. 3.4 Cross-sectional views of the three primary modes of thin-film growth including (a) Volmer-Weber (VW: island formation), (b) Frank-van der Merwe (FM: layer-by-layer), (c) terraces growth mode. Each mode is shown for several different amounts of surface coverage.

3.4 Summary

In summary, we investigated the influence of substrate temperature and coverage level on

growth dynamic mechanisms for silicene. Defects in the $\sqrt{13}\times\sqrt{13}$ phase are evoked by both the grain boundaries between different phases and low coverage. Deficiencies of atoms in the top layer form the defects in the 4×4 phase, which may be induced by the great number of atoms in the top layer and the weak bonds between the top layer atoms and the silver atoms in the substrate. The lattice mismatch between the silicene and the substrate induces breakages and distortions in the dark part of the moiré pattern in the $2\sqrt{3}\times2\sqrt{3}$ phase. Our results imply that the growth mechanism of silicene is the SK mode, which provides a better understanding of the complex thermodynamics and kinetics at the core of silicene formation, and a route towards fabricating novel nanostructures for application in the microelectronics industry.

1. B. J. Feng, Z. J. Ding, S. Meng, Y. G. Yao, X. Y. He, P. Cheng, L. Chen, and K. H. Wu, Nano Lett. **12**, 3057 (2012).
2. J. F. Gao and J. J. Zhao, Sci. Rep. **2**, 86 (2012).
3. C. -L. Lin, R. Arafune, K. Kawahara, M. Kanno, N. Tsukahara, E. Minamitani, Y. Kim, M. Kawai, and N. Takagi, Phys. Rev. Lett. **110**, 076801 (2013).
4. S. Cahangirov, M. Topsakal, E. Akturk, H. Sahin, and S. Ciraci, Phys. Rev. Lett. **102**, 236804 (2009).
5. C. -C. Liu, W. X. Feng, and Y. G. Yao, Phys. Rev. Lett. **107**, 076802 (2011).
6. L. Chen, C. -C. Liu, B. J. Feng, X. Y. He, P. Cheng, Z. J. Ding, S. Meng, Y. G. Yao, and K. H. Wu, Phys. Rev. Lett. **109**, 056804 (2012).
7. P. De Padova, P. Vogt, A. Resta, J. Avila, I. Razado-Colambo, C. Quaresima, C. Ottaviani, B. Olivieri, T. Bruhn, T. Hirahara, T. Shirai, S. Hasegawa, M. C. Asensio, and G. Le Lay, Appl. Phys. Lett. **102**, 163106 (2013).
8. M. Ezawa, Phys. Rev. Lett. **109**, 055502 (2012).
9. L. Chen, H. Li, B. J. Feng, Z. J. Ding, J. Qiu, P. Cheng, K. H. Wu, and S. Meng, Phys. Rev. Lett. **110**, 085504 (2013).

10. M. Ezawa, Phys. Rev. Lett. **110**, 026603 (2013).

11. H. Enriquez, S. Vizzini, A. Kara, B. Lalmi, and H. Oughaddou, J. Phys.: Condens. Matter **24**, 314211 (2012).

12. J. A. Venables, G. D. T. Spiller, and M. Hanbücken, Rep. Prog. Phys. **47**, 399 (1984).

13. A. Koma, K. Sunouchi, and T. Miyajima, J. Vac. Sci. Technol. B **3**, 724 (1985).

14. A. Koma, Thin Solid Films **216**, 72 (1992).

15. K. S. Kim, Y. Zhao, H. Jang, S. Y. Lee, J. M. Kim, K. S. Kim, J. H. Ahn, P. Kim, J. Y. Choi, and B. H. Hong, Nature **457**, 706 (2009).

CHAPTER 4

INVESTIGATION OF ELECTRON-PHONON COUPLING IN EPITAXIAL SILICENE BY *IN-SITU* RAMAN SPECTROSCOPY

In this chapter, we report on the special coupling between Dirac fermions and lattice vibrations, in other words, EPC, in silicene layers on an Ag(111) surface, which was probed by *in-situ* Raman spectroscopy. The tensile strain, induced by the lattice mismatch between silicene and the substrate, and the charge doping from the substrate, modulates the EPC strength. The Raman spectrum clearly reveals the evolution of defect peaks with increasing coverage by silicene layers. The peaks at low frequency correspond to the different electron scattering modes occurring at the zigzag and armchair edges. This work implies that Raman spectroscopy allows unambiguous, fast, and nondestructive identification of silicene layers, which is critically lacking in this emerging research field so far.

4.1 Introduction

Silicene, the silicon-based counterpart of graphene, has attracted intensive interest due to its unique characteristics and wide range of promising applications [1–4]. Theoretical simulations [5,6] predicted, as was very recently verified by experimental work [7], that silicene possesses a graphene-like electronic structure, in which the charge carriers behave as massless Dirac fermions due to the linear electronic dispersion. The strong SOC indicates that silicene could display a robust QSHE [8]. The interactions between electrons and quantized lattice vibrations, known as EPC, can improve our understanding of many physical phenomena in silicene, including transport behavior, Kohn anomalies, and possible superconductivity. Despite theoretical calculations [9] predicting that free-standing silicene

possesses unique EPC features due to its low-buckled (LB) atomic arrangement, this still needs to be clarified by experiments. It has been an experimental challenge, however, to research and tune the strength of the EPC in this silicon-based 2D Dirac fermion system due to the fact that the first layer of silicene is unstable under ambient atmospheric conditions, and *in-situ* investigations are highly desirable [10]. Raman spectroscopy is a valuable tool that can probe the EPC in an atomic layer and the phonon dynamics associated with 2D Dirac fermions [11]. In silicene, the long-wavelength optical E_{2g} phonon mode at the Γ point of the BZ, corresponding to the relative displacement of nonequivalent neighboring silicon atoms [9], is of specific interest. Due to the buckled structure, any perturbations will be expected to effectively induce direct electronic transitions across the Dirac point, where E_{2g} phonons couple to low-energy excitations.

In this chapter, we focus on *in-situ* Raman scattering studies of phonon modes in epitaxial silicene with different reconstructions on the Ag(111) surface at low temperatures. We reveal that the EPC in silicene can be effectively tuned by strain and doping effects, which is demonstrated by the shift of the E_{2g} phonon mode. Although depressed by electron doping, the EPC in silicene can be significantly enhanced by tensile strain. In addition, our Raman experiments reflect the Dirac fermion characteristics in this unique low-buckled 2D material, which is demonstrated by unique phonon modes correlated to electron scattering at the edge sites.

4.2 Experiments and methods

All samples used in this work were fabricated in a preparation chamber supplied with a low-temperature STM/scanning near-field optical microscopy system (LT-STM-SNOM,

SNOM1400, Unisoku Co.). Clean Ag(111) substrates were prepared by argon ion sputtering and annealed at 800 K for several cycles. The silicene monolayers were then grown on the Ag(111) surfaces by evaporation of silicon from a heated silicon wafer. *In-situ* Raman spectra were acquired on the silicene samples from the same areas as in the STM measurements. Raman laser irradiation (λ = 532 nm) was delivered through a single-mode optical fiber into the measurement chamber of the STM-SNOM system. A schematic diagram and product image of the *in-situ* UHV Raman/STM system is shown in Fig. 4.1 (a) and (b), respectively. All the measurements were carried out in UHV at 77 K. ARPES characterizations were performed at the photoelectron spectroscopy station in the Beijing Synchrotron Radiation Facility (BSRF) using a SCIENTA R4000 analyzer. A monochromatized He-I light source (21.2 eV) was used for the band dispersion measurements.

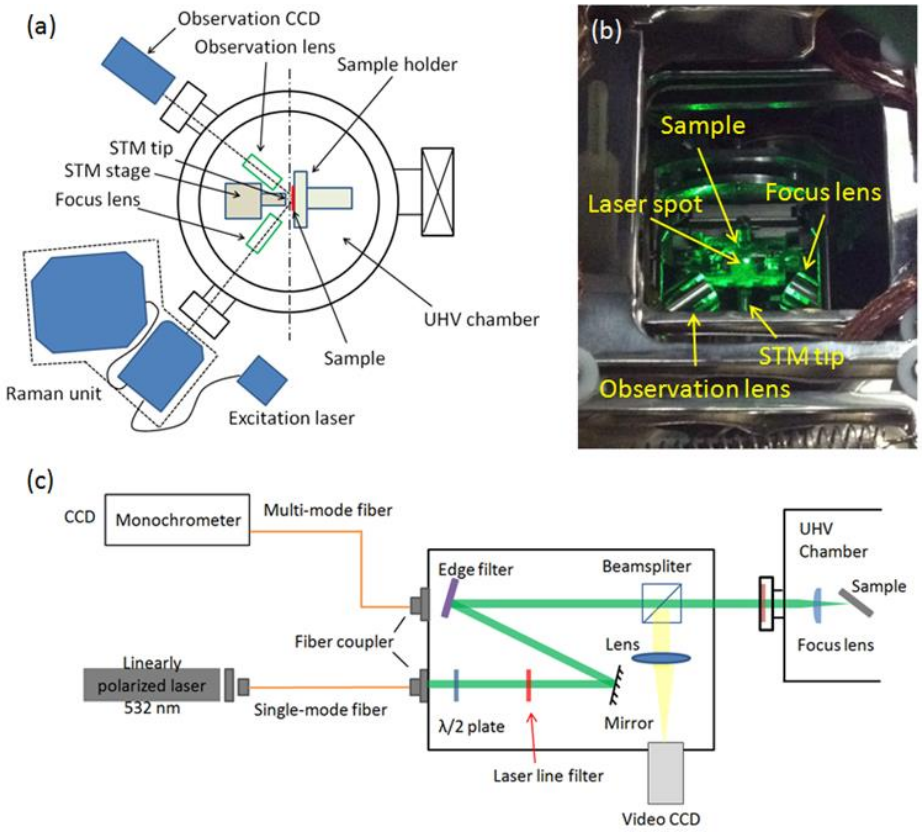

Fig 4.1 (a) Schematic illustration of in-situ UHV Raman/STM system setup. (b) Photograph of UHV Raman/STM measurement chamber. (c) Schematic diagram of Raman system.

4.3 Results and Discussion

4.3.1 STM images

Monolayer silicene with different phases can be obtained by varying the Si coverage and the Ag(111) substrate temperature during deposition. A comprehensive study on the growth mechanism of silicene on the Ag(111) surface can be found in chapter 3 [12]. Figure 4.2 displays typical STM images of silicene layers in different phases that were grown on Ag(111). Epitaxial silicene shows a mixed $\sqrt{13}\times\sqrt{13}/4\times4$ reconstruction with respect to 1×1 Ag(111) (or 3×3 reconstruction with respect to 1×1 silicene) (lattice constant a = 1.14 nm) in the first monolayers (see chapter 3) when the substrate was kept within the the temperature range from 450 to 480 K during deposition, as shown in Fig. 4.2 (a). From the second layer, only the $\sqrt{3}\times\sqrt{3}$ reconstruction (with respect to 1×1 silicene) with a much smaller lattice constant (a = 0.64 nm), consistent with a previous report [13], can be detected [Fig. 4.2 (b)]. It should be noted that the value of the $\sqrt{3}\times\sqrt{3}$ silicene unit cell is obviously smaller than that of the $\sqrt{3}\times\sqrt{3}$ Ag/Si(111) (~0.69 nm) [14], confirming the formation of silicene superstructure rather than the presence of $\sqrt{3}\times\sqrt{3}$ Ag and Si(111). Due to the fact that $\sqrt{3}\times\sqrt{3}$ multilayer silicene can be fabricated on a 4×4 silicene layer, as demonstrated in previous work [11,15], and on a $\sqrt{13}\times\sqrt{13}$ silicene layer, as shown in this work, both 4×4 and $\sqrt{13}\times\sqrt{13}$ silicene could be treated as the buffer silicene layer for the formation of $\sqrt{3}\times\sqrt{3}$ silicene. By carefully keeping the substrate temperature at 550 K during deposition [7],$\sqrt{3}\times\sqrt{3}$ monolayer silicene, which is treated as a second or subsequent layer in other reports [10–12,15], can be also epitaxially grown on a bare Ag(111) surface without a buffer silicene layer, as shown in Fig. 4.2 (c).

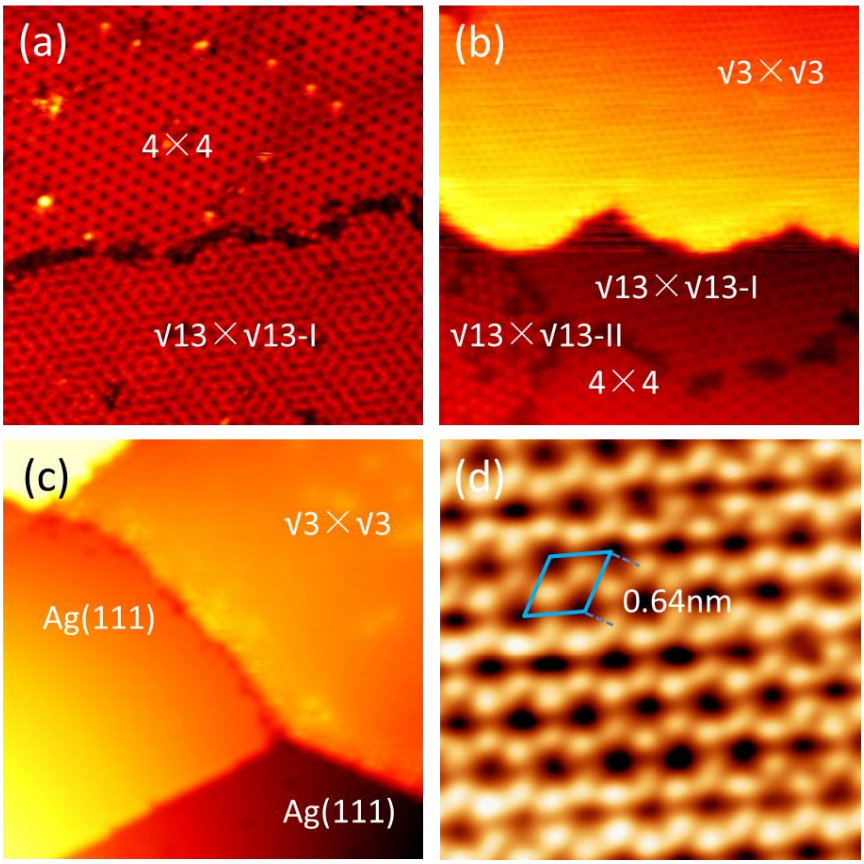

Fig. 4.2 STM images of silicene layers in different phases: (a) mixed √13×√13/4×4, (b) √3×√3 silicene grown on a√13×√13/4×4 buffer layer, (c) √3×√3 silicene grown on an Ag(111) substrate (30 nm × 30 nm, V_{bias} = −1.0 V, I = 1 nA), and (d) enlarged view of √3×√3 silicene. The rhombus marks the unit cell of √3×√3 silicene, which is used to calculate the lattice parameter of√3×√3 silicene (5 nm × 5 nm, V_{bias} = 0.5V, I = 4nA).

4.3.2 Raman results and electronic structure of silicene

A typical Raman spectrum of the √13×√13/4×4 layer is shown in Fig. 4.3 (a). The first-order asymmetric peak located at 530 cm^{-1} can be attributed to the zone-center E_{2g} vibrational mode [16,17]. The shoulder peak from 495 to 508 cm^{-1} is evoked by the quantum confinement effect, which is a common feature for silicon substance in morphologies with small dimensions, such as microcrystalline silicon [18] and silicon nanowires [19]. Because the intensity is affected by the amount of boundary defects in the √13×√13/4×4 silicene layer,

the peak at 230 cm^{-1} is assigned to the "*D*" peak. Figure 4.3 (b) displays the Raman spectra for $\sqrt{3}\times\sqrt{3}$ silicene with different coverage grown on the $\sqrt{13}\times\sqrt{13}/4\times4$ layer. The thickness of this superstructure is 0.32 nm, the same as that in previous reports [20]. The extent of second layer (SL) coverage by the $\sqrt{3}\times\sqrt{3}$ silicene layer is listed. Based on the fact that the $\sqrt{3}\times\sqrt{3}$ silicene is heaped upon the $\sqrt{13}\times\sqrt{13}/4\times4$ layer in a three-dimensional island mode [10–12,15,20,21], 1 SL should actually correspond to a $\sqrt{3}\times\sqrt{3}$ silicene sample with multilayer thickness. A much stronger E_{2g} mode in $\sqrt{3}\times\sqrt{3}$ silicene was observed at 530 cm^{-1} than from the $\sqrt{13}\times\sqrt{13}/4\times4$ layer. Five Raman peaks at lower frequency from 200 to 500 cm^{-1} (marked as D_1–D_5) were detected in the samples with low coverage. These peaks vanished when the coverage was more than 1 SL. The same features were also observed in Raman spectra of a $\sqrt{3}\times\sqrt{3}$ silicene monolayer grown on Ag(111) without the $\sqrt{13}\times\sqrt{13}/4\times4$ layer [Fig. 4.3 (c)], implying that the low-frequency Raman modes were not the result of interlayer interactions between different silicene layers. ARPES measurements on epitaxial $\sqrt{3}\times\sqrt{3}$ silicene show a Dirac point located at an energy ~ 0.33 eV below the Fermi level, consistent with previous work [15,21], as shown in Fig. 4.4 (c). This energy shift is not large enough to block the excitation of electrons by photons with energy up to 2.3 eV (532 nm). Here, $\sqrt{13}\times\sqrt{13}/4\times4$ silicene, however, hybridizes strongly with the Ag(111) surface atoms, forming a hybridized metallic surface state [22]. These different electronic structures of the silicene layers on Ag(111) surfaces indeed reveal the fact that the interactions between Si and Ag are stronger in $\sqrt{3}\times\sqrt{3}/4\times4$ silicene, but very weak in $\sqrt{3}\times\sqrt{3}$ silicene. Thus, the Raman signal is depressed in $\sqrt{13}\times\sqrt{13}/4\times4$ silicene. There is doubt as to whether the observed 2D silicon layers are true silicene or just reconstructions of the Si(111) surface. Based on this point, we carried out Raman measurements on the Si(111) surface, as shown in Fig. 4.3 (a). A clear first-order Raman peak (E_{2g} mode) is located at 520 cm^{-1}, which is lower by a value of 10 cm^{-1} than that of the silicene E_{2g} peak (530 cm^{-1}). Two broad Raman peaks at 300 cm^{-1} and 970 cm^{-1} are

assigned to the 2TA (transverse acoustic) and 2TO (transverse optical) modes in Si(111), which are both absent from the Raman spectra of silicene. In addition, no Raman signal of Ag(111) could be detected resulting from Rayleigh scattering. Hence, the E_{2g} and D Raman peaks of the silicene layers reflect distinct phonon modes that are different from these in Si(111), conforming the formation of the epitaxial silicene layers on the Ag(111) surface.

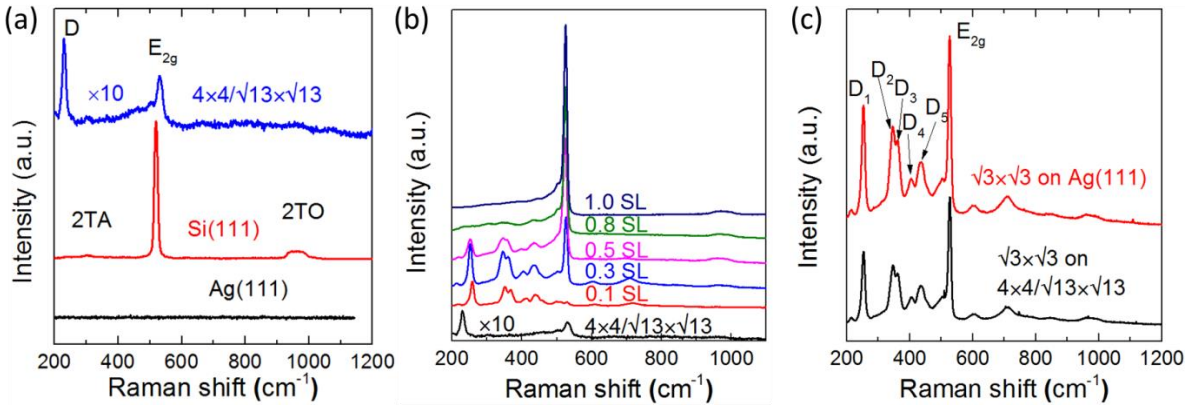

FIG. 4.3 (a) Raman spectra of the Ag(111) substrate, Si(111), and a √13×√13/4×4 buffer layer. (b) Raman spectra of √3×√3 silicene grown on √13×√13/4×4 buffer layers with different coverage. SL denotes the extent of coverage of the √3×√3 silicene layer. (c) Raman spectra of a √3×√3 silicene layer (coverage of 0.3 ML) grown on an Ag(111) surface and on a √13×√13/4×4 buffer layer, respectively.

Figure 4.4 (a) displays an enlarged view of the E_{2g} peaks for √3×√3 superstructures with different coverage. The E_{2g} mode frequency (570 cm^{-1}) of free-standing (FS) silicene [23] is marked as a reference. The actual positions of the E_{2g} peaks can be obtained by a Gaussian-Lorentz peak fitting, as shown in Fig. 4.4 (b). It can be seen that the position of the E_{2g} peak (530 cm^{-1}) was decreased to a lower wavenumber in epitaxial silicene, which is the same as in previous reports, where it was measured by an *ex-situ* method [10,13]. It should be noted that the E_{2g} mode in 2D materials can be modulated by strain [24–29]. The *in-plane* Si-Si distance d_{in} can be calculated from the distance a between the centers of two neighboring honeycombs, as shown in Fig. 4.2 (d), according to the equation $d_{in} = a/3 = 2.2$

Å [1,4]. Considering the vertical buckling distance $d_B \sim 0.8$ Å, the actual Si-Si bond length of the epitaxial √3×√3 silicene is around 2.35 Å. Tensile strain should be present in the √3×√3 silicene layers, as can be seen by comparing the smaller Si-Si bond length of 2.24 Å in FS silicene. The frequency shift of the E_{2g} mode in strained silicene can be described as [26,27]

$$\Delta\omega = \omega_{strain} - \omega_0 = -\frac{nv\omega_0(a_{strain}-a_0)}{a_0} = b\varepsilon, \quad (4.1)$$

where ω_{strain} and ω_0 are the frequencies of the E_{2g} mode in strained and FS silicene, respectively, n is the dimensionality of the material, v is the Grüneisen constant, b is the strain-shift coefficient, and a_{strain} and a_0 are the *in-plane* lattice parameters of the strained and FS silicene layers, respectively. The *in-plane* strain, $\varepsilon = (a_{strain} - a_0)/a_0 = \Delta a/a_0$, is around 0.05, which was obtained from the Si-Si bond lengths for both the strained and FS silicene. The detailed structural parameters are listed in Table 4.1. The frequency of the E_{2g} mode in silicene is downshifted to 520 cm^{-1} by taking the coefficient b = -832 cm^{-1} [27,30,31], which is smaller than that in our Raman spectra (530 cm^{-1}) but comparable to the E_{2g} mode frequency of Si(111). Therefore, there must be another issue affecting E_{2g} phonon frequency.

TABLE 4.1 Detailed structural parameters of free-standing (FS) silicene and low-buckled (LB) silicene: range of Si-Si bond lengths for experimental results (d^{exp}_{Si-Si}) and calculation results (d^{cal}_{Si-Si}), the average Si-Si bond length (d_a) used for the calculation of *in-plane* strain ($\varepsilon = d_a(\mathrm{LB}) - d_a(\mathrm{FS})/d_a(\mathrm{FS})$) of LB silicene grown on Ag(111) substrate compared to of FS silicene.

Type	d^{exp}_{Si-Si}	d^{cal}_{Si-Si}	d_a	ε	E_{2g} peak
FS	N/a	2.24 Å [9,28]	2.24 Å	0	570 cm^{-1} [9]
LB	2.32~2.38 Å	2.28~2.40 Å [2,7]	2.35 Å	5 %	530 cm^{-1}

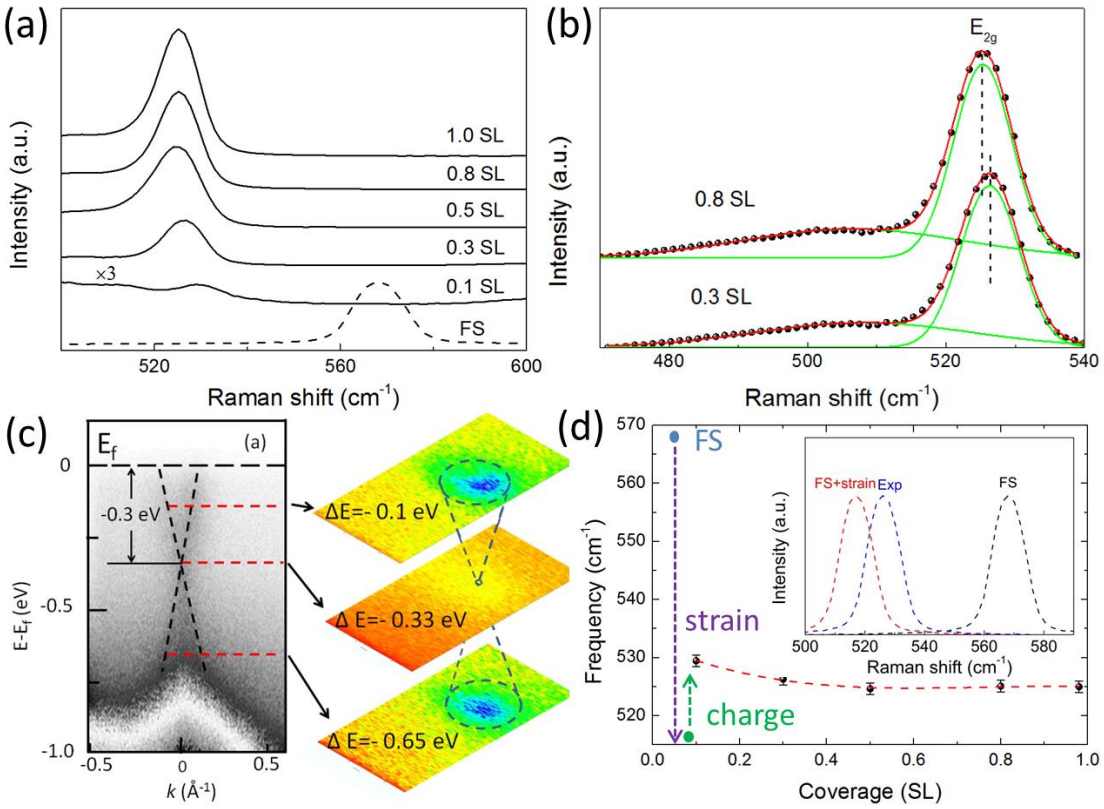

Fig. 4.4 (a) Enlarged view of the Raman spectrum of the E_{2g} peak for samples with different coverage and with the frequency ranging from 500 to 600 cm^{-1}. The E_{2g} mode frequency (570 cm^{-1}) of free-standing (FS) silicene is marked as a reference [9]. (b) The fitting results on the E_{2g} peak for 0.3 and 0.8 SL samples. The dashed lines are used to mark the position of the E_{2g} mode. (c) ARPES results for an epitaxial $\sqrt{3}\times\sqrt{3}$ silicene layer. The left side shows that two faint linear dispersed bands cross at the BZ center Γ point. The right side displays constant-energy cuts of the spectral function at different energy levels, implying Dirac cone structure origin of both bands, which can be assigned to linear π and π^* states of $\sqrt{3}\times\sqrt{3}$ silicene. The Dirac point is located at around 0.33 eV below the Fermi level, indicating that the electron-doping effect is attributed to the silver substrate. (d) The frequency of E_{2g} mode as a function of sample coverage. Both (d) and the inset of (d) figures are drawn to illustrate the strain and doping effects on the E_{2g} peak position in $\sqrt{3}\times\sqrt{3}$ silicene, where the strain effect softens the frequency, while charge doping upshifts the E_{2g} mode.

In fact, electron or hole doping in silicene could induce a hardening of the mode frequency in silicene [9,11], e.g., the E_{2g} mode will shift to a higher frequency resulting from charge

doping effect. The ARPES results verify that the Dirac point of √3×√3 silicene grown on Ag(111) is located at ~0.33 eV below the Fermi surface due to electron doping from the silver substrate, as shown in Fig. 4.4 (c). The E_{2g} vibration at the zone center (Γ point) couples with Dirac fermions at the zone boundary (K points), which is allowed by silicene lattice symmetry. The carriers residing in the honeycomb lattice mutually interact with the E_{2g} mode through dynamical perturbations due to the creation and annihilation of virtual long-wavelength electron-hole pairs across the gapless Dirac point. The energy range of the virtual electron-hole pairs allowed by the Pauli principle is decided by the level of the Fermi energy (E_F). The E_{2g} mode in silicene is hardened due to the raising of the E_F of silicene by electron doping. The upshift in the value of E_{2g} frequency is about 10 cm^{-1}, consisting well with previous simulation results [9]. Figure 4.4 (d) is a schematic diagram of both strain and doping effects on the position of the E_{2g} Raman peak in √3×√3 phase.

It should be noted that the EPC strength depends principally on the phonon frequencies in 2D materials [32,33]. The EPC can be generally characterized by a dimensionless parameter $\gamma = N_F V_{ep}$, where N_F is the electron density of states (DOS) and V_{ep} is the mean electron-phonon coupling potential at the Fermi level [33]. The value of γ is proportional to ω^{-2} ($\gamma \sim \omega^{-2}$) [32,33]. This relationship results from the zero-point oscillation amplitude induced by large deformation and the energy reconstruction in the perturbation theory. Both of the two factors correspond exactly to the strain effect that is present in 2D materials. Thus, the value of ω reflects the EPC strength. According to the E_{2g} peak shift value from 570 cm^{-1} (FS) to 520 cm^{-1} (strained silicene), the enhancement of the EPC strength in silicene could be up to 20%. The enhancement of the EPC is of particular interest because its strength gives rise to superconductivity in Bardeen-Cooper-Schrieffer (BCS) superconductors. The enhanced EPC strength in silicene may support recent observations on the existence of a superconducting gap in silicene layers [34].

In graphene, the armchair and zigzag edges induce two Raman-active D and D' modes resulting from the intervalley and intravalley scattering of quasiparticles in Dirac cones, respectively [35–37]. As a similar Dirac fermion system, silicene should also possess such features in Raman spectroscopy, as shown in the inset of Fig. 4.5 (a). In our results, five distinct Raman peaks in the low wave-number range (220–470 cm^{-1}) were observed in the samples with coverage of less than 1 SL, as shown in Fig. 4.3 (b).

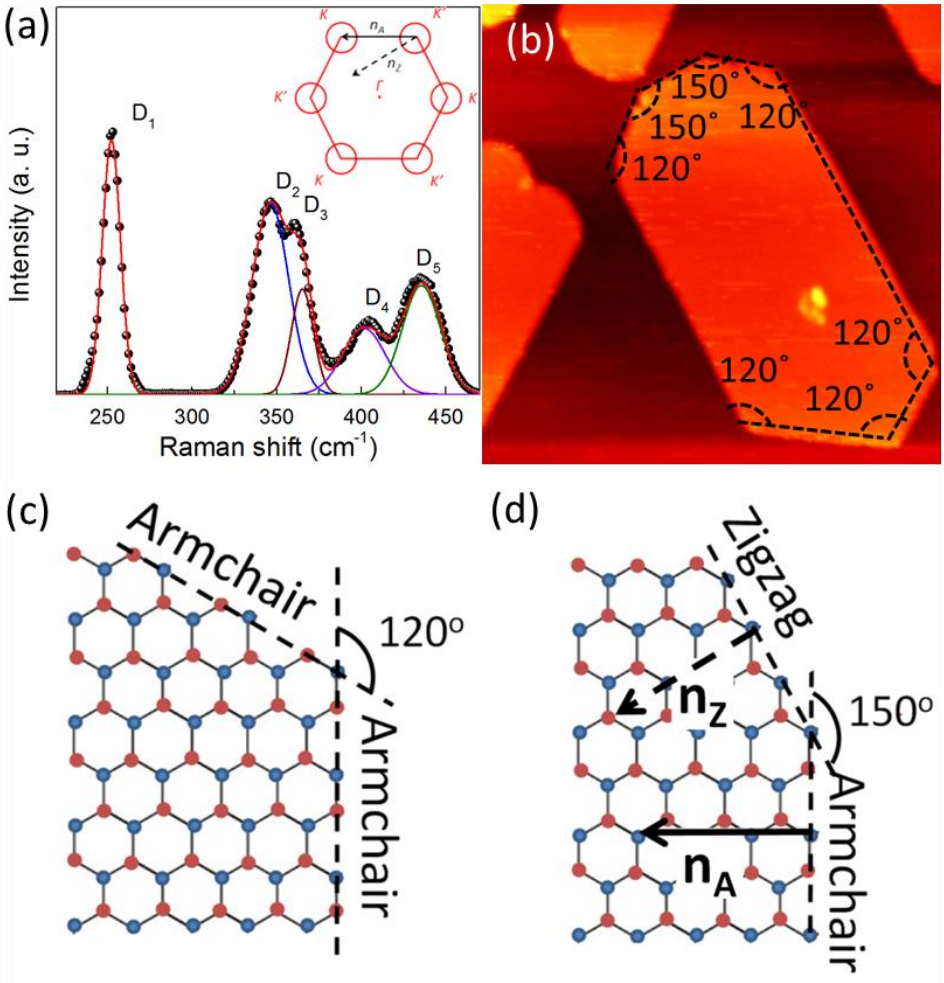

Fig. 4.5 (a) Fitted Raman spectra of √3×√3 silicene layers with coverage of 0.3 SL in the frequency range of 220–470 cm^{-1}, in which the Raman peaks due to edges are marked as D_1–D_5. (b) STM image of two typical arrangements of the edges: armchair/zigzag and armchair/armchair, resulting in two edge angles of 150 °and 120 °, respectively. (c), (d) Atomic structures of armchair and zigzag edges. Only the armchair edge supports elastic intervalley electrons scattering in the Brillouin zone, as indicated in the inset of (a).

Figure 4.6 shows fitted Raman peaks of silicene layers with different coverage. The fitted Raman spectrum of the buffer-layer silicene is shown in Fig. 4.6 (a), in which three peaks, at 468cm^{-1}, 505 cm^{-1}, and 531 cm^{-1}, can be identified in the frequency range from 400 cm^{-1} to 560 cm^{-1}. Besides the E_{2g} peak and a peak due to the quantum confinement effect at 505 cm^{-1}, the broad peak at 468 cm^{-1} is assigned to the 2*D* peak, due to the emergence of the *D* peak at 230 cm^{-1} [see Fig. 4.2 (a)], similar to the *ex-situ* Raman results [28]. The *D* peak and 2*D* peak are contributed by the first and the second order zone-boundary phonons that are activated by defects [38], e.g. the domain boundaries observed in STM. The intensities of the *D* and 2*D* peaks are weakened by increasing coverage of the second $\sqrt{3}\times\sqrt{3}$ silicene layer and eventually become negligible in the 0.5 SL sample, which indicates their origins in the buffer layer instead of the top $\sqrt{3}\times\sqrt{3}$ layer, as shown in Fig. 4.6 (c). The Raman peak due to quantum confinement can be observed at low frequency for all the samples, which further confirms the nanosized silicene domains observed by STM. In 0.1 SL $\sqrt{3}\times\sqrt{3}$ silicene grown on the buffer layer, four peaks ranging from 480 cm^{-1} to 550 cm^{-1} can be fitted that are attributed to the $4\times4/\sqrt{13}\times\sqrt{13}$ buffer layer and the second $\sqrt{3}\times\sqrt{3}$ layer with low coverage, as shown in Fig. 4.6 (d). The other two peaks are due to the E_{2g} mode and the low-frequency tail induced by the quantum confinement effect for $\sqrt{3}\times\sqrt{3}$ silicene. The E_{2g} mode of the $4\times4/\sqrt{13}\times\sqrt{13}$ buffer layer and the $\sqrt{3}\times\sqrt{3}$ silicene is marked as E^1_{2g} and E^2_{2g}, respectively. The E^1_{2g} peak becomes negligible when the coverage of the second layer is more than 0.3 SL, as shown in Fig. 4.6 (d). These results suggest that $\sqrt{3}\times\sqrt{3}$ silicene shows much higher peak intensity than the $4\times4/\sqrt{13}\times\sqrt{13}$ phase. Figure 4.6 (b) shows the normalized intensity of the D_1 to D_5 peaks as a function of $\sqrt{3}\times\sqrt{3}$ silicene coverage. The ratio of peak intensities remains almost the same in $\sqrt{3}\times\sqrt{3}$ silicene layers with different coverage, indicating that all these peaks have the same origin. The intensities of these five peaks increase with increasing coverage up to 0.3 SL, then decrease when the coverage is greater than 0.5 SL, and

eventually become negligible in the sample with coverage higher than 0.8 SL. We propose that these peaks are induced by the edge defects in silicene. In √3×√3 silicene samples, the ratio of the edges compared to the sample area first increases with increasing silicene domain size. After reaching a critical coverage, the ratio of edge components decreases, leading to the lower peak intensity [37-39].

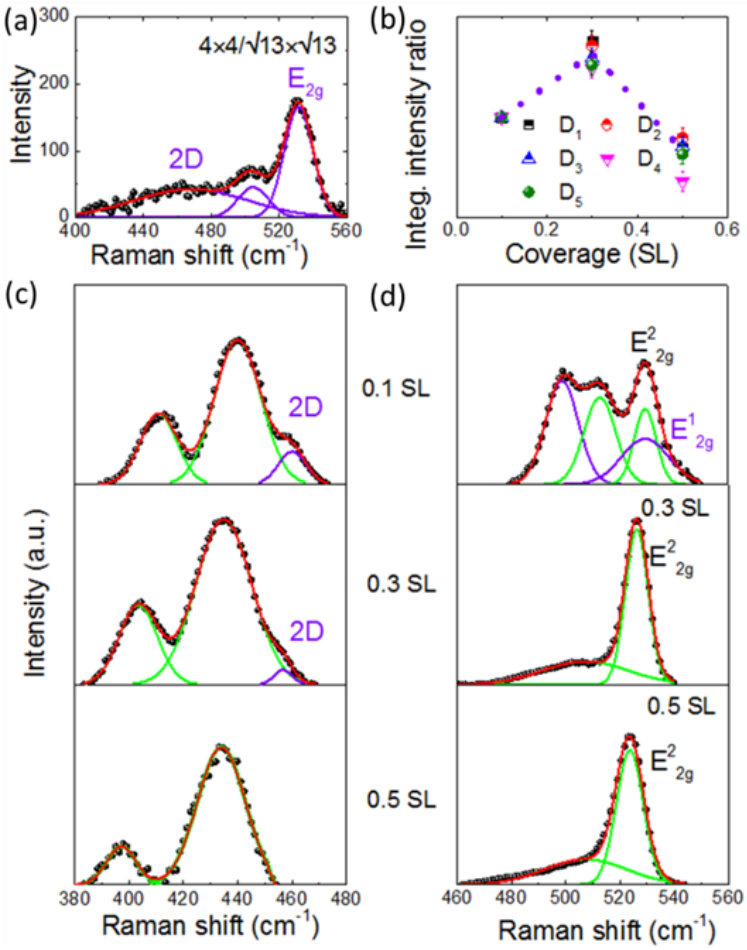

Fig 4.6 (a) Raman spectrum of 4×4/√13×√13 silicene buffer layers in the frequency range of 400cm^{-1} to 560 cm^{-1}. Experimental data, fitted Raman peaks, and fitted Raman spectrum are in black, purple, and red, respectively. (b) The intensities of edge Raman peaks show a strict dependence on silicene coverage. (c) Fitted Raman spectra of √3×√3 phase samples with coverage from 0.1 to 0.5 SL grown on 4×4/√13×√13 buffer layers in the frequency range of 380 cm^{-1} to 480 cm^{-1}. Experimental data, fitted Raman peaks, and fitted Raman spectra are in black, green (purple), and red, respectively. (d) Fitted Raman spectra of √3×√3

phase samples for coverage from 0.1 to 0.5 SL grown on 4×4/√13×√13 buffer layers in the frequency range of 460 cm^{-1} to 560 cm^{-1}. Experimental data, fitted Raman peaks, and fitted Raman spectra are in black, green (purple), and red, respectively. E^1_{2g} and E^2_{2g} represent the double-resonance E_{2g} peak for the 4×4/√13×√13 and √3×√3 silicene layers, respectively.

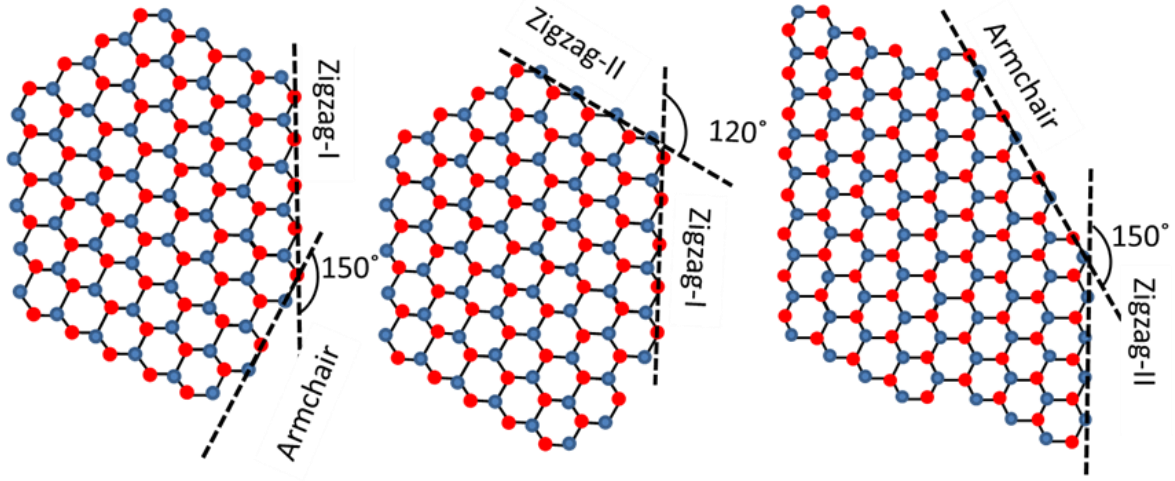

Fig. 4.7 Three kinds of possible edges existing in √3×√3 silicene. The red and blue balls represent the up-buckled and down-buckled Si atoms, respectively.

Since the intensities of these peaks can be scaled well with each other and show a strong dependence on the coverage, the peaks are most likely associated with the effects of edges. There are two types of edges for materials with a honeycomb structure, armchair edges and zigzag edges. Due to the low buckled structure of silicene, it is hard to image the atomic arrangements at the edge positions by STM measurements. Two different angles, 150˚ for ZA and 120˚ for AA, are shown in Fig. 4.5 (b), which helps to distinguish the two types of edges. Due to the low-buckled structure of silicene, the structure symmetry is further reduced in contrast to planar graphene. For example, two zigzag edge structures could possibly exist in √3×√3 silicene layers, as shown in Fig. 4.7. One only consists of up-buckled atoms and the other one only consists of down-buckled atoms. Consequently, more vibrational modes induced by the various edge arrangements are expected in silicene Raman spectroscopy,

consisting well with the emergence of the D_1–D_5 peaks in our results. The edge-induced Raman peaks reflect the unique buckled characteristic of silicene. Tip-enhanced Raman spectroscopy is likely to advance insights into the edge effects on phonon modes in this low-buckled 2D material.

4.4 Summary

In summary, silicene layers with different structures and coverage have been fabricated and identified by *in-situ* UHV Raman spectroscopy and STM. The intrinsic phonon modes for different silicene structures are identified. We found that the EPC strength in silicene could be significantly enhanced due to the lattice mismatch between the silicene layers and the substrate. The Raman spectroscopy results demonstrate the effects of coverage, strain, charge doping, and defects on silicene's phonon modes, and allows unambiguous, high-throughput, nondestructive identification of epitaxial silicene.

1. B. J. Feng, Z. J. Ding, S. Meng, Y. G. Yao, X. Y. He, P. Cheng, L. Chen, and K. H. Wu, Nano Lett. **12**, 3057 (2012).
2. J. F. Gao, and J. J. Zhao, Sci. Rep. **2**, 86 (2012).
3. C. -L. Lin, R. Arafune, K. Kawahara, M. Kanno, N. Tsukahara, E. Minamitani, Y. Kim, M. Kawai, and N. Takagi, Phys. Rev. Lett. **110**, 076801 (2013).
4. P. Vogt, P. De Padova, C. Quaresima, J. Avila, E. Frantzeskakis, M. C. Asensio, A. Resta, B. Ealet, and G. Le Lay, Phys. Rev. Lett. **108**, 155501 (2012).
5. S. Cahangirov, M. Topsakal, E. Aktürk, H. Sahin, and S. Ciraci, Phys. Rev. Lett. **102**, 236804 (2009).
6. C.-C. Liu, W. X. Feng, and Y. G. Yao, Phys. Rev. Lett. **107**, 076802 (2011).

7. L. Chen, C. -C. Liu, B. J. Feng, X. Y. He, P. Cheng, Z. J. Ding, S. Meng, Y. G. Yao, and K. H. Wu, Phys. Rev. Lett. **109**, 056804 (2012).
8. M. Ezawa, Phys. Rev. B **87**, 155415 (2013).
9. J. -A. Yan, R. Stein, D. M. Schaefer, X. -Q. Wang, and M. Y. Chou, Phys. Rev. B **88**, 121403 (2013).
10. P. De Padova, C. Ottaviani, C. Quaresima, B. Olivieri, P. Imperatori, E. Salomon, T. Angot, L. Quagliano, C. Romano, A. Vona, M. Muniz-Miranda, A. Generosi, B. Paci, and G. Le Lay, 2D Mater. **1**, 021003 (2014).
11. N. B. Kopnin and E. B. Sonin, Phys. Rev. Lett. **100**, 246808 (2008).
12. X. Xun, J. C. Zhuang, Y. Du, S. Eilers, G. Peleckis,W. K. Yeoh, X. L. Wang, S. X. Dou, and K. H. Wu, Proceedings of 2014 International Conference on Nanoscience and Nanotechnology (ICONN) (IEEE, New York, 2014), 28–30 (2014).
13. P. Vogt, P. Capiod, M. Berthe, A. Resta, P. De Padova, T. Bruhn, G. Le Lay, and B. Grandidier, Appl. Phys. Lett. **104**, 021602 (2014).
14. Y. G. Ding, C. T. Chan, and K. M. Ho, Phys. Rev. Lett. **67**, 1454 (1991).
15. P. De Padova, P. Vogt, A. Resta, J. Avila, I. Razado-Colambo, C. Quaresima, C. Ottaviani, B. Olivieri, T. Bruhn, T. Hirahara, T. Shirai, S. Hasegawa, M. C. Asensio, and G. Le Lay, Appl. Phys. Lett. **102**, 163106 (2013).
16. A. Gupta, G. Chen, P. Joshi, S. Tadigadapa, and P. C. Eklund, Nano Lett. **6**, 2667 (2006).
17. R. Arafune, C. -L. Lin, K. Kawahara, N. Tsukahara, E. Minamitani, Y. Kim, N. Takagi, and M. Kawai, Surf. Sci. **608**, 297 (2013).
18. Z. Iqbal and S. Vepřek, J. Phys. C: Solid State Phys. **15**, 377 (1982).
19. B. B. Li, D. P. Yu, and S. -L. Zhang, Phys. Rev. B **59**, 1645 (1999).

20. P. De Padova, J. Avila, A. Resta, I. Razado-Colambo, C. Quaresima, C. Ottaviani, B. Olivieri, T. Bruhn, P. Vogt, M. C. Asensio, and G. Le Lay, J. Phys.: Condens. Matter **25**, 382202 (2013).
21. E. Salomon, R. El Ajjouri, G. Le Lay, and T. Angot, J. Phys.: Condens. Matter **26**, 185003 (2014).
22. D. Tsoutsou, E. Xenogiannopoulou, E. Golias, P. Tsipas, and A. Dimoulas, Appl. Phys. Lett. **103**, 231604 (2013).
23. J. Yan, Y. B. Zhang, P. Kim, and A. Pinczuk, Phys. Rev. Lett. **98**, 166802 (2007).
24. F. Speck, J. Jobst, F. Fromm, M. Ostler, D. Waldmann, M. Hundhausen, H. B. Weber, and Th. Seyller, Appl. Phys. Lett. **99**, 122106 (2011).
25. J. Röhrl, M. Hundhausen, K. V. Emtsev, Th. Seyller, R. Graupner, and L. Lay, Appl. Phys. Lett. **92**, 201918 (2008).
26. D. J. Lockwood and J. -M. Baribeau, Phys. Rev. B **45**, 8565 (1992).
27. R. -P. Wang, G. -W. Zhou, Y. -L. Liu, S. -H. Pan, H. -Z. Zhang, D. -P. Yu, and Z. Zhang, Phys. Rev. B **61**, 16827 (2000).
28. E. Cinquata, E. Scalise, D. Chiappe, C. Grazianetti, B. van den Broek, M. Houssa, M. Fanciulli, and A. Molle, J. Phys. Chem. C **117**, 16719 (2013).
29. E. Scalise, M. Houssa, G. Pourtois, B. van den Broek, V. Afanas'ev, and A. Stesmans, Nano Res. **6**, 19 (2013).
30. E. Anastassakis, A. Cantarero, and M. Cardona, Phys. Rev. B **41**, 7529 (1990).
31. S. Nakashima, T. Mitani, M. Ninomiya, and K. Matsumoto, J. Appl. Phys. **99**, 053512 (2006).
32. W. McMillan, Phys. Rev. **167**, 331 (1968).
33. C. Si, Z. Liu, W. H. Duan, and F. Liu, Phys. Rev. Lett. **111**, 196802 (2013).
34. L. Chen, B. J. Feng, and K. H. Wu, Appl. Phys. Lett. **102**, 081602 (2013).

35. L. G. Cançado, M. A. Pimenta, B. R. A. Neves, M. S. S. Dantas, and A. Jorio, Phys. Rev. Lett. **93**, 247401 (2004).

36. R. Saito, G. Dresselhaus, and M. S. Dresselhaus, Phys. Rev. B **61**, 2981 (2000).

37. C. Casiraghi, A. Hartschuh, H. Qian, S. Piscanec, C. Georgi, A. Fasoli, K. S. Novoselov, D. M. Basko, and A. C. Ferrari, Nano. Lett. **9**, 1433 (2009).

38. A. C. Ferrari, J. C. Meyer, V. Scardaci, C. Casiraghi, M. Lazzeri, F. Mauri, S. Piscanec, D. Jiang, K. S. Novoselov, S. Roth, and A. K. Geim, Phys. Rev. Lett. **97**, 187401 (2006).

39. Z. H. Ni, H. M. Wang, Y. Ma, J. Kasim, Y. H. Wu, and Z. X. Shen, ACS Nano **2**, 1033 (2008).

CHAPTER 5

TUNING THE BAND GAP IN SILICENE BY OXIDATION

In this chapter, we report that monolayer silicene grown on Ag(111) surfaces features a band gap that is tunable by oxygen adatoms from semimetallic to semiconducting type. We find that the adsorption configurations and amounts of oxygen adatoms on the silicene surface are the critical factors for band gap engineering, which is determined by the different buckling degrees in $\sqrt{13}\times\sqrt{13}$, 4×4, and $2\sqrt{3}\times2\sqrt{3}$ superstructures. The Si-O-Si bonds are the most energy-favored species formed on $\sqrt{13}\times\sqrt{13}$, 4×4, and $2\sqrt{3}\times2\sqrt{3}$ structures under oxidation, which is verified by *in-situ* Raman spectroscopy as well as first-principles calculations. The silicene monolayers retain their structures when fully covered by oxygen adatoms. Our work demonstrates the feasibility of tuning the band gap of silicene with oxygen adatoms, which, in turn, expands the base of available two-dimensional electronic materials for devices with properties that cannot be realized with graphene oxide.

5.1 Introduction

As a new allotrope of silicon in a two-dimensional honeycomb structure, silicene has attracted intensive research interest due to its novel physical and chemical properties [1-10]. Theoretically, the prediction of strong spin-orbit coupling in silicene allows a spin-orbit band gap of 1.55 meV at the Dirac point and induces a detectable QSHE [9-13]. The electronic π- and π^*-bands resulting from the Si p_z orbital disperse linearly to cross at the Fermi level (E_F), leading to massless Dirac fermion characteristic electrons [12,13]. Thus, electrons in silicene possess a large Fermi velocity, which has been recently verified by observation of pronounced quasiparticle interference patterns in STM images [12]. Additionally, its excellent

scalability and compatibility with current silicon-based nanotechnology have made silicene a fascinating candidate for the design of novel electronic components and interconnects on the nanometer scale [14].

Despite its notable properties, the intrinsic zero band gap property of silicene hinders its applications in electronic devices which require controllable conductivities through logic gates. Therefore, a tunable band gap in silicene would be highly desirable. Conventionally, chemical doping, selective functionalization, and the introduction of defects have been adopted to modulate band structures in 2D zero-gap materials. In graphene, these approaches can only be performed at edges or surface defects, however, due to the inertness of sp^2 hybridized carbon atoms, while those carbon atoms that are located at the edges or at defects are more reactive, hindering the functionality of graphene [15]. In contrast, silicon atoms prefer to adopt sp^3 hybridization over sp^2 in silicene, leading to high chemical activity on the surface and allowing tunability of the electronic states by chemical functionalization [16,17]. Due to its capability of breaking the symmetry, oxygen is one of the feasible species for chemical functionalization, such as with the energy gap opening at E_F in 2D materials [15]. Therefore, controllable oxidation could be expected to modulate electronic states in silicene. It provides an opportunity for realizing various electronic structures in silicene, offering the possibility of exploring silicene-based electronic devices, such as in gate oxides. Furthermore, oxidation of silicene layers is expected to be one of the major steps toward effective introduction of oxygenated functional groups into the Si network. Nevertheless, the high chemical reactivity of silicene prevents controllable oxidation by conventional chemical routes, such as the solvent casting method, thus hindering progress in such research.

In this work, we report a study of band gap tuning in different silicene buckling structures by controllable oxidation processes, using STM combined with *in-situ* Raman spectroscopy. The

connection between buckled silicene structures and oxygen adatoms is found by the aid of DFT calculations. We show that the detailed bonding configurations of oxygen adatoms on the silicene surface are determined by the buckling structures. The oxygen adatoms can effectively tune the band gap, causing the gap opening. Silicene possibly keeps its honeycomb structure even after the surface is fully covered by oxygen adatoms. Importantly, the surface of silicene shows much higher chemical reactivity than that of the edge, distinguishing it from the case of graphene [15].

5.2 Experiments and methods

5.2.1 Sample preparation

All samples used in this work were synthesized *in-situ* in the preparation chamber of a low-temperature UHV scanning tunneling microscopy/scanning near-field optical microscopy system (LT-STM-SNOM) (SNOM1400, Unisoku Co.). A clean Ag(111) substrate was prepared by argon ion sputtering and subsequent annealing at 800 K for several cycles. The silicene monolayers were deposited by the evaporation of a heated silicon wafer. The deposition flux was around 0.08 monolayers per minute (ML/min). The temperature of the Ag(111) substrate was 450 K, 500 K, and 550 K for the formation of $\sqrt{13}\times\sqrt{13}$, 4×4, and $2\sqrt{3}\times2\sqrt{3}$ superstructures, respectively. Silicene oxide samples were fabricated by *in-situ* oxidation of silicene monolayers with a varying O_2 dose. The Langmuir (L) is used as the unit of exposure of O_2, *i.e.*, 1 L is an exposure of 10^{-6} Torr O_2 in 1 s. The STM combined with Raman spectroscopy measurements was carried out in UHV ($< 8\times10^{-11}$ torr) at 77 K with Pt/Ir tips. In order to achieve maximum quality images and the best *dI*/*dV* signal, the tips were firstly annealed by electron-beam heating in the preparation chamber, which allowed

re-crystallization of tip apex. Then, the tips were further sharpened and calibrated on a clean Ag(111) surface. STM topographic images were obtained under constant current mode with an active distance feedback loop. *In-situ* Raman spectra were collected for silicene and silicene oxides with a laser wavelength of 532 nm^{-1}.The laser was focused on the sample by an incident lens driven by a piezo motor. Before each experiment, the Raman system was calibrated on a Si(111) standard sample. Extreme care was taken in order to avoid any sample damage or laser induced heating during Raman measurements. Such conditions were successfully achieved, which is evidenced by the fact that the surface structures of samples were not changed before, during, or after the Raman measurements. The incident power during Raman measurements was varied between ~5 mW and ~0.5 mW. No significant spectral change, expect for the Raman signal intensity, was observed in this range.

5.2.2 Characterization

The STM and Raman spectroscopy measurements were carried out in UHV at 77 K. STS differential conductance (dI/dV) (where I is current and V is voltage) measurements were carried out with lock-in detection by applying a modulation of 20 mV to the tunnel voltage at the frequency of 973 Hz. The differential conductance maps were obtained by recording an STS spectrum at each spatial pixel during STM topographic measurements. Before the STS measurements, the Pt/Ir tip was first calibrated on a silver surface. The Raman spectra were acquired using a laser excitation of 532 nm (2.33 eV) delivered through a single-mode optical fiber.

5.2.3 DFT calculation

Ab initio calculations were performed using DFT and the plane wave basis, as realized in the Vienna *Ab Initio* Simulation Package (VASP) [18]. The electron-ion interactions were

characterized by projector augmented wave (PAW) potentials [19]. The generalized gradient approximation (GGA) with the Perdew-Burke-Ernzerhof (PBE) functional was adopted to define the exchange-correlation interaction [20]. A kinetic energy cutoff of 400 eV for the plane-wave basis and a convergence criterion of 10^{-4} eV for the total energies were carefully tested and adopted in all calculations. The configurations for the superstructures of silicene on the Ag(111) surface were results from a previous simulation by Gao and Zhao [4].

5.3 Results and discussion

5.3.1 Oxidation sites on silicene in different phases

There are different reconstructions of epitaxial monolayer silicene on the Ag(111) surface, which could be controlled by the substrate temperature during deposition. Figure 5.1 shows single-layer silicene in three typical structures, namely, $\sqrt{13}\times\sqrt{13}$, 4×4, and $2\sqrt{3}\times2\sqrt{3}$ (with respect to Ag(111)) grown on Ag(111) surfaces at different substrate temperatures. Due to the similar formation energies, $\sqrt{13}\times\sqrt{13}$ and 4×4 superstructures always coexist with each other when the substrate temperature is located between 450 and 520 K during deposition, as shown in Fig. 5.1 (a). When the substrate temperature is as high as 550 K, the pure $2\sqrt{3}\times2\sqrt{3}$ silicene structure could be obtained (Figure 5.1 (b)). High-resolution STM images for each structure are displayed in Figure 5.1 (c-e). All silicene structures show distinctive buckled forms. The topmost Si atoms in a buckled structure are defined as the “top-layer” (TL) and the other atomic layers with low height levels are defined as “bottom-layer” (BL). Unlike the sp^2 hybridization for carbon in graphene, silicon atoms exhibit the energetically favored sp^3 hybridization [21], which is responsible for these low-buckled structures [22]. On the Ag(111) surface, various buckling degrees are evoked by variations in lattice mismatch and interaction

between the silicene superstructures and the substrate, as shown in Fig. 5.1 (f). The metal passivation effect induced by the Ag(111) surface also affects the buckling of silicene on the BL Si side due to the hybridization between the p_z electrons of BL Si atoms and the 4*d* electrons of Ag(111). Therefore, the value of buckling varies from 0.86 Å for the 4×4 phase to 1.40 Å for the √13×√13 superstructure [23].

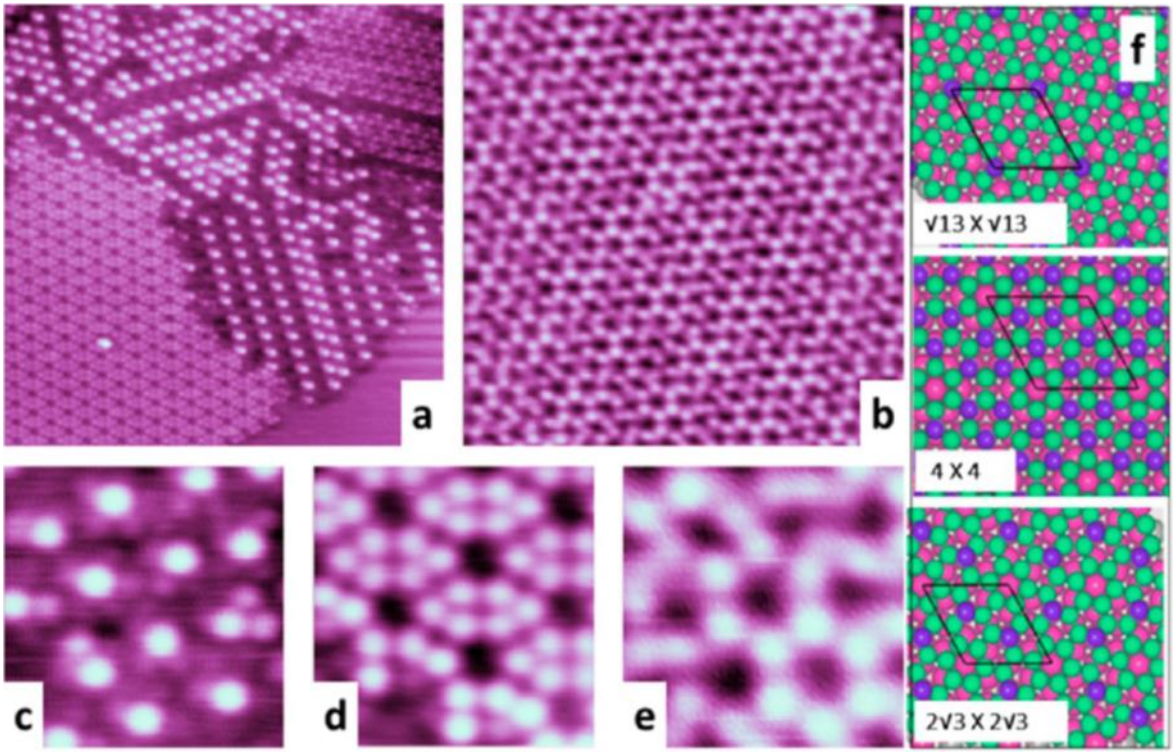

Fig. 5.1 Topographic images of silicene monolayers grown on Ag(111): (a) STM topographic image of two major coexisting phases of silicene, √13×√13 and 4×4 (scanning area 16 nm×16 nm, V_{bias} = -0.5 V, I = 4 nA). (b) STM image of silicene 2√3×2√3 phase (scanning area 10 nm×10 nm, V_{bias} = -0.8 V, I = 4 nA). (c-e) High-resolution STM images of √13×√13, 4×4, and 2√3×2√3 phases, respectively (scanning area 2 nm×2 nm, V_{bias} = -0.02 V, I = 5 nA). (f) Schematic illustrations of various phases of silicene monolayers on Ag(111). Purple and green balls represent TL and BL Si atoms, respectively. Pink atoms represent Ag balls in the substrate.

For √13×√13 phase, only one Si atom out of the 14 total Si atoms per unit cell resides on the top site in the buckled structure. In contrast, there are six TL atoms out of 18 Si atoms per

unit cell in the 4×4 structure, leading to a “flower-like” pattern in STM images. In the 2√3×2√3 phase, Si atoms are in a “three-fold” or “bridge” position on the Ag(111) surface; hence, there are two topmost atoms out of 14 Si atoms per unit cell. The distances between nearest neighboring TL Si atoms are 5.46 Å, 2.51 Å, and 3.67 Å for the √13×√13, 4×4, and 2√3×2√3 superstructures, respectively. TL Si atoms are expected to be highly active in epitaxial silicene on Ag(111) due to the unsaturated bond. BL Si atoms, in contrast, are relatively more stable, due to the passivating effect of the free electrons from the substrate.

Figure 5.2 (a-c) presents typical STM images of silicene layers in √13×√13, 4×4, and 2√3×2√3 structures that were exposed to 10 Langmuir (L) O_2. The marked isolated protrusions in these STM images are clearly different from the clean silicene surface in Fig. 5.1. The protrusions are higher than for TL Si atoms. The interpretation of these protrusions is obtained from the STS maps of *dI*/*dV*, which is determined by the local density of states, and from *in-situ* Raman spectroscopy, which reflects the vibrational modes of chemical bonds. By comparative study of the STM topographic and spectroscopic images, we find that the atomic-scale protrusions on silicene show an extremely low density of states over much of the energy range studied, indicating localized electrons at these positions, as shown in Fig. 5.2 (d-f). Such a large difference in DOS cannot be simply attributed to a possible impurity-induced structural distortion at the TL Si atoms. The bright protrusions are most likely raised by oxygen adatoms, due to the fact that they always appear after oxidation, but never for pure silicene layers. To justify this observation, we carried out *in-situ* Raman spectroscopic measurement on samples after exposing them to oxygen, as shown in Fig. 5.2 (g). The spectra show a clear broad shoulder at lower wavenumbers (450cm^{-1}-510 cm^{-1}) following the silicene signature E_{2g} peak. This peak is associated with the Si-O bonds due to its position and broadness [22,24]. With increasing oxygen dose, the intensity of the shoulder peak is enhanced in all the silicene structures, confirming that these bright protrusions are

adsorbed oxygen atoms on the silicene surface.

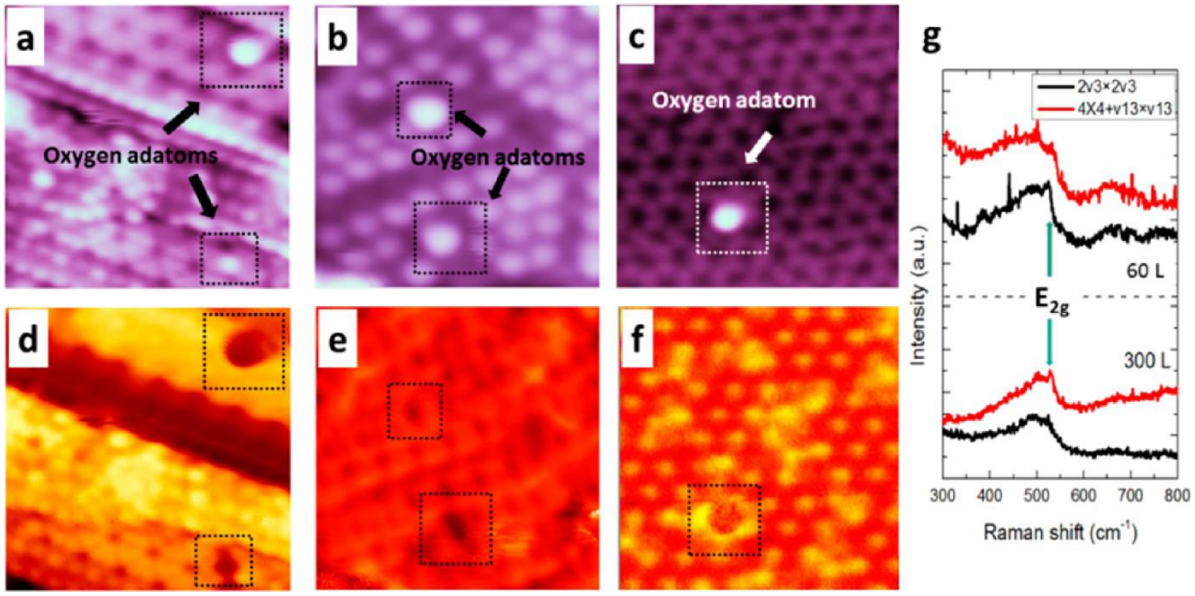

Fig. 5.2 STM images of oxygen adatoms on silicene in (a) $\sqrt{13}\times\sqrt{13}$, (b) 4×4, and (c) $2\sqrt{3}\times2\sqrt{3}$ phases grown on Ag(111) substrate (scanning area 4 nm×4 nm, V_{bias} =-0.2 V, I = 4 nA). The bright protrusions are attributed to oxygen adatoms in each STM image, which are indicated by the arrows. (d-f) Corresponding STS mappings to STM images (a-c), respectively. (g) *In-situ* Raman spectra for silicene oxidized under different oxygen doses. An obvious broad shoulder at lower wavenumber to the E_{2g} peak indicates the formation of Si-O bonds.

The oxygen adatoms could be located on bridge sites, resulting in the configuration of double-atom-bonding overbridging O atoms (O^d). The O^d is a major configuration in the partially oxidized situation for all three silicene phases, as shown in Fig. 5.3 (a-c). The heights of oxygen adatoms residing on silicene layers are different, however, as displayed by the STM images in Fig. 5.3 (d). The height of oxygen adatoms on $\sqrt{13}\times\sqrt{13}$ and $2\sqrt{3}\times2\sqrt{3}$ silicene layers is higher than that of adatoms on 4×4 silicene by about 1 Å. The distances between nearest neighboring TL Si atoms are 5.46 and 3.67 Å for $\sqrt{13}\times\sqrt{13}$ and $2\sqrt{3}\times2\sqrt{3}$ silicene, respectively, distances which are twice long as the typical Si-O bond lengths in bulk SiO_2 (varies from 1.58 Å to 1.62 Å). Thus, both TL and BL Si atoms are involved in

silicon-oxygen bonds as Si(BL)-O^{d}-Si(TL). In this case, oxygen adatoms prefer to reside beside TL Si rather than BL Si, as shown in Fig. 5.4. By contrast, the distance between nearest neighboring TL Si atoms in 4×4 silicene is 2.51 Å, indicating different buckling from the other two superstructures. DFT calculations indicate that TL Si atoms in 4×4 silicene could be transfered to BL Si atoms under oxidation to minimize the total energy. Therefore, Si(BL)-O^{d}-Si(BL) is also a possible configuration for overbridging oxygen adatoms.

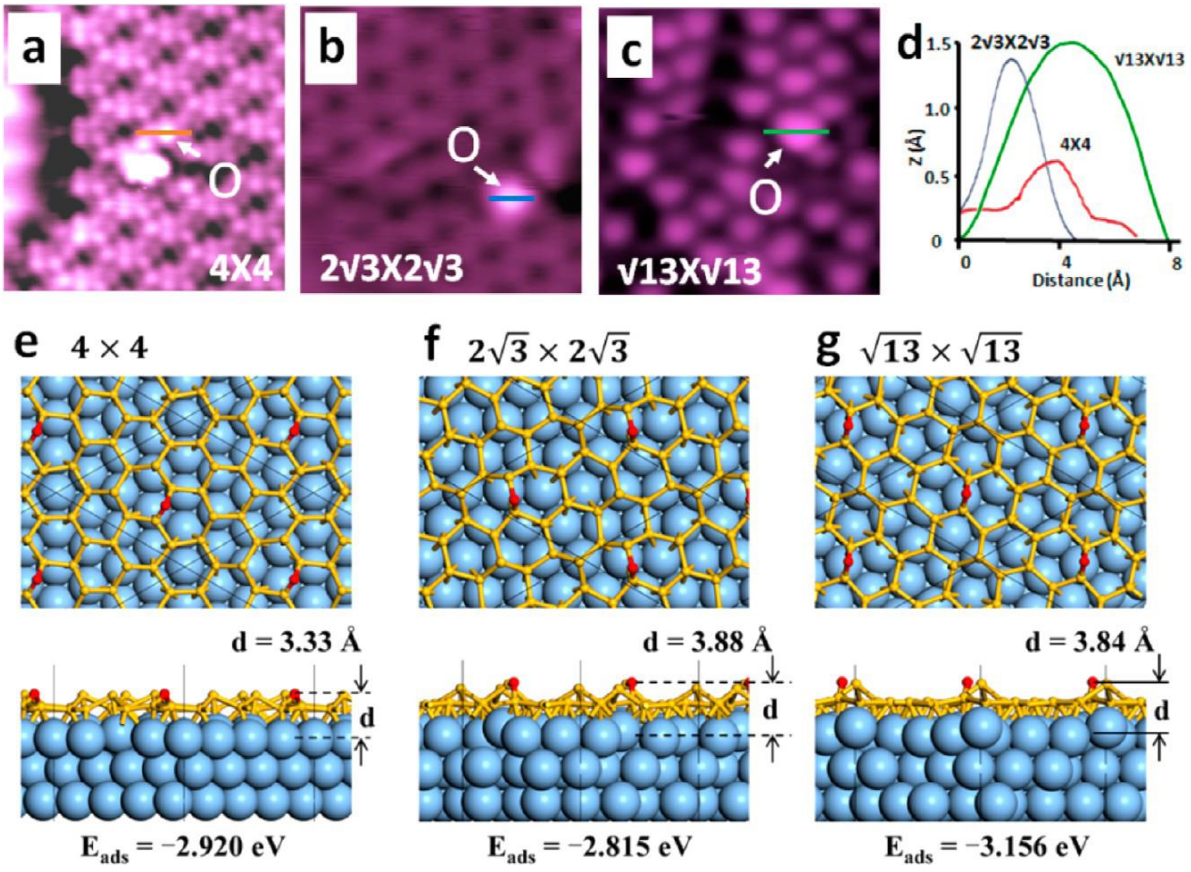

Fig. 5.3 STM and STS images of oxidized silicene in (a) 4×4, (b) 2√3×2√3, and (c) √13×√13 structures (scanning area 4 nm×4 nm, V_{bias} = -0.2 V, I = 4 nA). The oxygen adatoms prefer to reside on TL Si atoms in the initial oxidation. (d) Line profiles of oxygen adatoms on silicene corresponding to the lines in the STM images in (a)-(c). DFT simulations (top and side views) of atomic structures for oxygen adatoms on Ag(111) supported silicene monolayers in different superstructures: (e) 4×4, (f) 2√3×2√3, (g) √13×√13. The black rhombuses in the top views represent the unit cell. Red, oxygen; yellow, silicon; blue, silver.

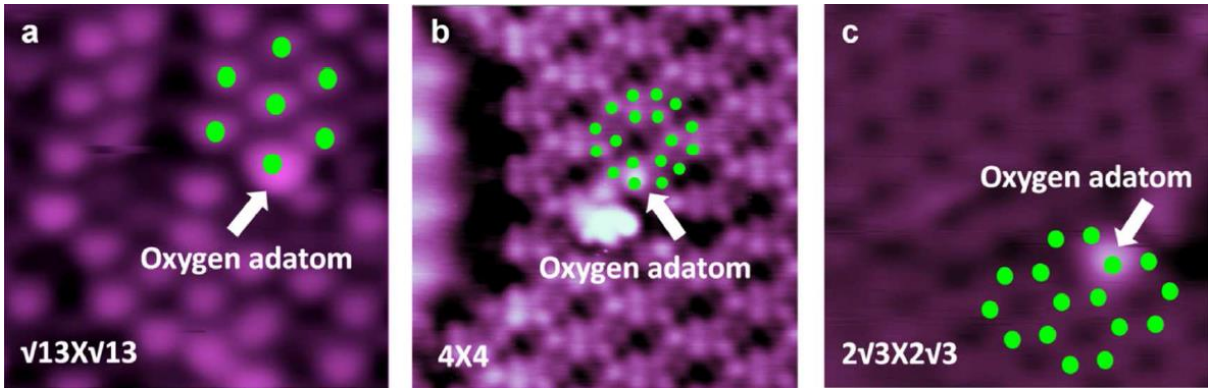

Fig. 5.4 STM images of oxygen adatoms on silicene in different phases, (a) $\sqrt{13}\times\sqrt{13}$, (b) 4×4 and (c) $2\sqrt{3}\times2\sqrt{3}$, on Ag(111) substrate. The bright protrusions are attributed to oxygen adatoms in each STM image. The green spots correspond to toplayer Si atoms in silicene. They indicate that oxygen adatoms prefer to reside near the toplayer silicon atoms in buckled silicene at the initial oxidization stage.

Our measurements revealed that silicene monolayers with different structures show different oxidation behavior. It was found that for all three structures, the initial stage of oxidation always begins in the top-layer (TL) silicon atoms in the buckled silicene monolayer, namely, $\sqrt{13}\times\sqrt{13}$, 4×4, and $2\sqrt{3}\times2\sqrt{3}$. This would indicate that the energy required for the adsorption of oxygen adatoms might be lower for TL silicon atoms as compared to the bottom-layer (BL) silicon. It is interesting that oxygen adatoms prefer to reside on the surface of silicene rather than the edge, which is totally different from the case of graphene, as shown in Fig. 5.5 and Fig. 5.6. This can be explained from the hybridization point of view. In the case of carbon in graphene, sp^2 hybridization is more energetically stable for honeycomb structures, but sp^3 is the energetically favored form of silicon in silicene. As a result, dangling bonds are expected on the silicene surface as well as at the edge. Once consideration of the interaction between silicon and silver atoms is taken into account, it is clear that the edge Si atoms are likely to have stronger bonding with Ag than the Si atoms at the surface. The energy barrier for absorption of oxygen adatoms, therefore, is lower at the surface. Further investigations, such as by Kelvin probe force microscopy, are required, however, in order to fully understand the

oxygen bonding features on silicene. These experiments will be carried out in the near future.

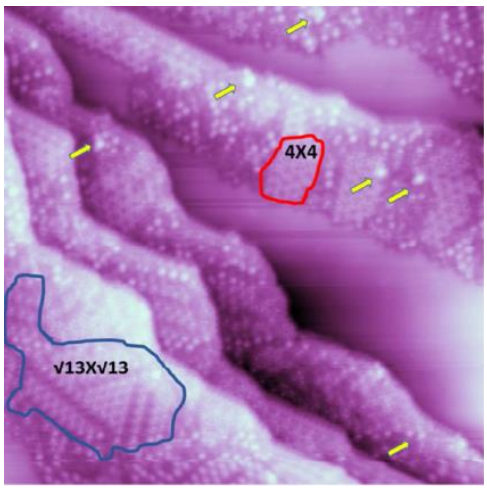

Fig. 5.5 STM image of √13×√13 and 4×4 mixed-structured oxidized silicene layers on Ag(111). The coverage of silicene is 0.6 ML, which was specifically designed to study the different roles of the edge and the surface during oxidation. Typical √13×√13 and 4×4 areas are circled in blue and red, respectively. The oxygen adatoms are marked by yellow arrows. All oxygen adatoms prefer to reside on the surface instead of the edge, which indicates that the energy barrier for adsorption of oxygen adatoms on the surface is lower than on the edge. (Sample was exposed to 10 L of O_2 before STM measurement. Scanning area 26×26 nm^2, V_{bias} = -0.15 V, I = 5 nA.)

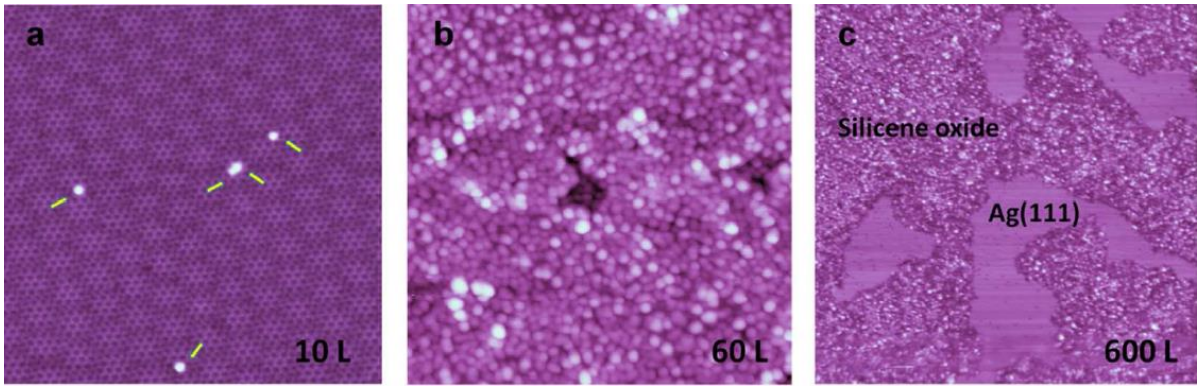

Fig. 5.6 STM images of 2√3×2√3 silicene structures after oxidation under (a) 10 L O_2, (b) 60 L O_2 and (c) 600 L O_2. Shrinkage of silicene oxide results in the exposure of the bare Ag(111) surface in (c). (V_{bias}= 0.8 V, I = 2 nA)

5.3.2 DFT calculations of adsorption energies

The above assumption on oxygen adsorption configurations is further verified by the DFT calculations, in which oxygen adatoms prefer to adsorb on the bridge sites of silicene for all three configurations upon relaxation. The equilibrium structures and adsorption energies for individual oxygen adatoms on silicene monolayers in the three typical superstructures are shown in Fig. 5.7 (e-g). The adsorption energy, E_{ads}, for an oxygen adatom on silicene is defined as:

$$E_{ads} = E_{tot} - E_{Si-Ag} - \frac{1}{2}E_{O_2} \quad (5.1)$$

where E_{tot} is the total energy of the entire system of Ag(111)-supported silicene with one oxygen adatom; E_{Si-Ag} is the total energy of the silicene superstructure on Ag(111); E_{O_2} is the energy of an oxygen molecule in gas phase. Negative adsorption energy means that the oxidation of silicene is exothermic. The calculated adsorption energy could be as low as -3 eV, indicating that silicene sheets in these three superstructures can be easily oxidized. Due to its having the largest amplitude of adsorption energy, the $\sqrt{13}\times\sqrt{13}$ phase seems to be most easily oxidized. The distance between the oxygen adatom and the Ag(111) surface can be measured by a height parameter *d* (see Fig. 5.3 (e-g)), where the average height of all Ag atoms in the first layer of the slab model is taken as reference. Among the three superstructures considered, the 4×4 has the lowest height of 3.33 Å compared to those of the $\sqrt{13}\times\sqrt{13}$ (d = 3.84 Å) and $2\sqrt{3}\times2\sqrt{3}$ (d = 3.88 Å) structures. The relative height difference is in good accordance with experimental results by STM, as shown in Fig. 5.3 (d). It should be noted that the DFT simulations are only able to qualitatively model the experimental observations. We only considered one oxygen adatom per unit cell within the periodic boundary condition for each superstructure, leading to a difference between the realistic

situation and simulated results in terms of both the concentration and spatial distribution of the oxygen atoms. Nonetheless, the differences between the various oxidized silicene superstructures revealed from DFT simulations would be still valid.

5.3.3 Electronic structure of silicene layers with oxygen adatoms

The previous reports predicted that the band structure of silicene could be tailored into various types, including semimetals, semiconductors, and insulators, by chemical functionalization methods such as oxidation [25,26]. The STM and STS results on partially oxidized silicene layers on Ag(111) are displayed in Fig. 5.7, where a series of spectra were collected along lines cut across the oxygen adatoms on the three silicene superstructures. The magnitude of the gap shows significant variation among the different superstructures. It should be noted that the gap is larger at oxygen adatom sites and becomes smaller when the locations are well away from the adsorption sites. Nevertheless, the gap still persists at a lateral distance of 3 nm around oxygen adatoms, indicating the large effective area of oxygen adatoms for the electronic structure of silicene. Considering that the average distances between neighboring oxygen adatoms on silicene in each structure are less than 3 nm, we realize that the gap is opened over the whole silicene surface, even with a low oxygen dose of 20 L. The oxygen adatoms do not show an ordered structure, causing fluctuation of the gap value at different sites on the oxidized silicene surface. In 4×4 silicene, the gap varies from 0.18 to 0.30 eV under an oxygen dose of 20 L. The most typical gap value is about 0.18 eV, as shown in Fig. 5.7 (b), while $\sqrt{13}\times\sqrt{13}$ and $2\sqrt{3}\times2\sqrt{3}$ structures show band gap values of 0.11-0.14 eV and 0.15-0.18 eV, respectively, as shown in Fig. 5.7 (a,c). These values for the band gaps are in qualitative agreement with the DFT simulations, as shown in Fig. 5.8. Due to the semimetal zero gap characteristic of pure silicene for each phase, the STS results clearly demonstrate that there is a band gap opening associated with the amount of oxygen

adatoms. The band gap is increased with the incresing oxygen dose. The gap of oxidized silicene is homogeneous when the oxygen dose is greater than 30 L, as shown in Fig. 5.7. The values of the band gaps are 0.18 eV, 0.9 eV, and 0.22 eV for the $\sqrt{13}\times\sqrt{13}$, 4×4, and $2\sqrt{3}\times2\sqrt{3}$ structures, respectively, under oxidation when the oxygen dose is up to 60 L. These values are significantly smaller than that of the semiconducting band gap in bulk silicon.

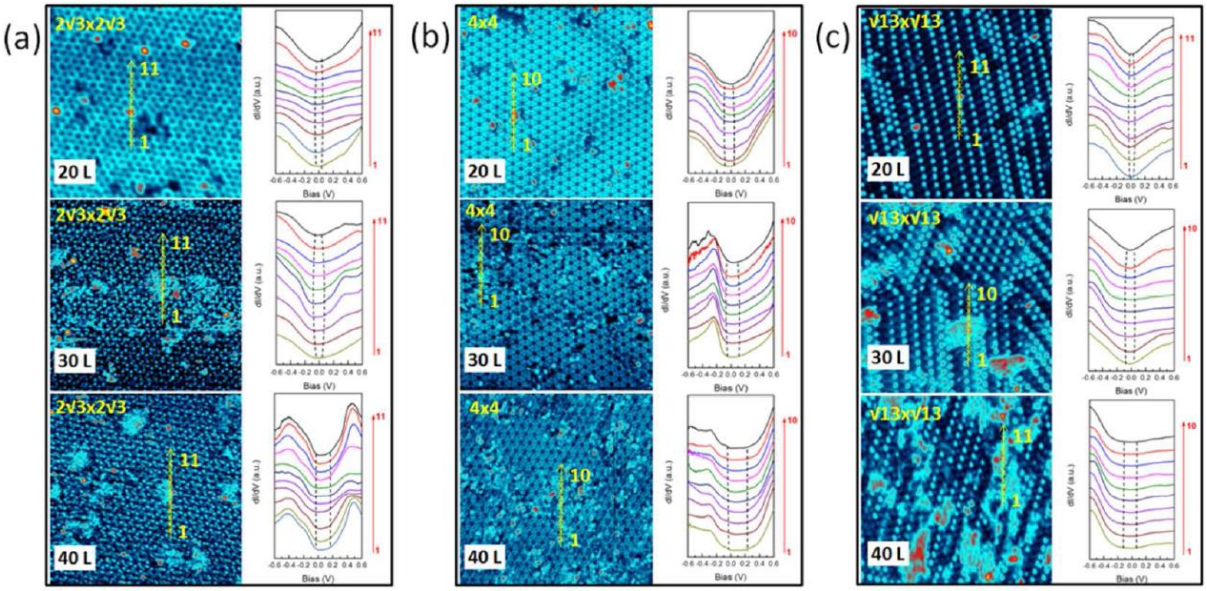

Fig. 5.7 STM images (left) and spatial STS dI/dV curves (right) measured on (a) $2\sqrt{3}\times2\sqrt{3}$, (b) 4×4, and (c) $\sqrt{13}\times\sqrt{13}$ silicene layers oxidized under various oxygen doses from 20 L to 40 L. Tunneling spectra (dI/dV curves) were obtained along a line indicated by the arrows in the corresponding STM topographic images on their left. The dashed lines in each STS result illustrate the value of the band gap. STM images were obtained at V_{bias} = -0.8 V, I = 0.6 nA. Scanning area was 24×24 nm^2. The oxygen adatoms appear as bright protrusions on the silicene layers.

While the gap opens homogeneously for oxidized silicene, small differences in occupied and unoccupied states can be observed, which are most likely due to the inhomogeneous LDOS induced by disordered oxygen adatoms. It is proposed that the conduction band of partially oxidized silicene mainly arises from the Si *p*-orbital and the O *p*-orbital, and that the valence band originates from the O *p*-orbital [26]. The width of the band gap is mainly affected by the

adsorption sites of oxygen adatoms. Since the valence band of silicene oxide mainly originates from the *p*-orbital of O, the dangling bonds of TL Si in oxidized 4×4 silicene are fully saturated by oxygen adatoms, resulting in the largest gap in oxidized silicene among the three structures. Unpaired electrons in oxidized √13×√13 and 2√3×2√3 silicene layers, however, contribute a narrow gap under low oxygen doses. Through varying the oxygen dose, we found that the band gaps are indeed tunable and dominated by the number of oxygen adatoms. Interestingly, oxygen adatoms prefer to be accommodated at the surface of silicene rather than the edge, in contrast to graphene [27], which is most likely due to the dangling bonds on the edge Si atoms, which are passivated by the Ag(111) surface.

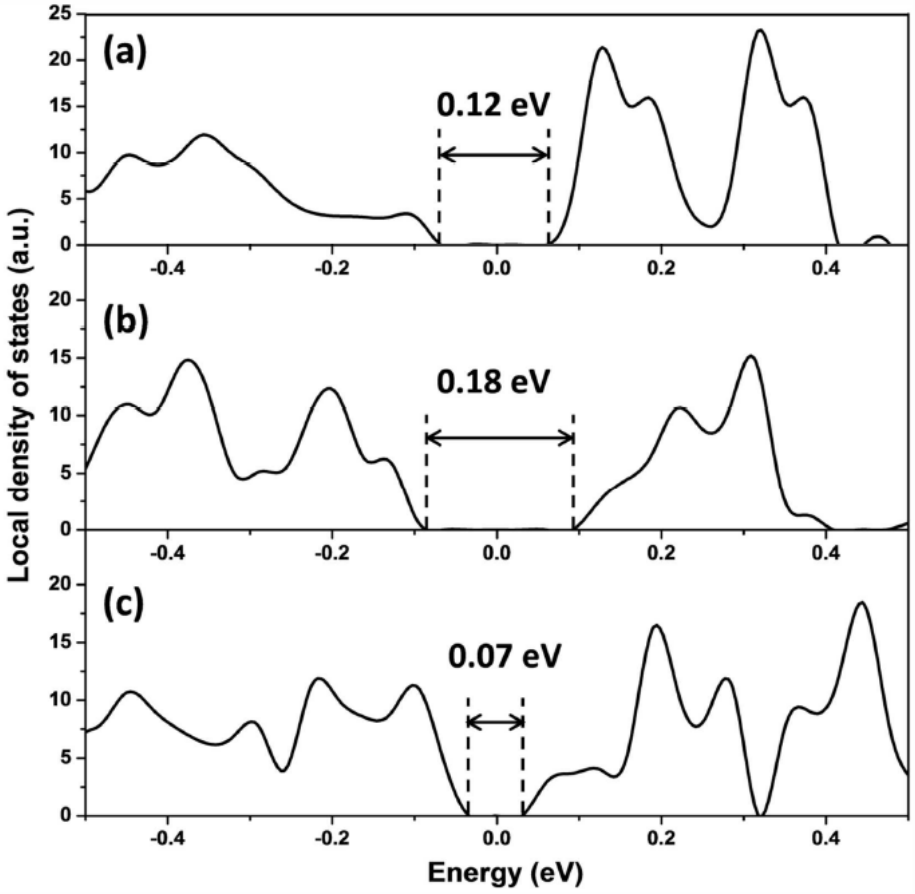

Fig. 5.8 DFT calculated density of states of (a) √13×√13, (b) 4×4 and (c) 2√3×2√3 silicene layers with oxygen adatoms (oxygen dose is 10 L).

Recent studies have claimed that the minimum oxygen dose for silicene oxidization is as high as 1000 L [25]. It is still unclear, however, how oxygen adatoms associate with silicene layers, especially for their structure before oxidation, which is crucial for further chemical functionalization. Figure 5.9 shows STM results on silicene exposed to different oxygen doses, *i.e.*, 10 L, 60 L, and 600 L, respectively. The surface of silicene in the $2\sqrt{3}\times2\sqrt{3}$ structure is fully covered by oxygen adatoms at the oxygen dose of 60 L, as shown in Fig. 5.9 (b). The adatoms exhibit an amorphous-like disordered nature rather than a distinct structure. The insets in Fig. 5.9 display the corresponding fast Fourier transform (FFT) pattern for each sample. Interestingly, clear FFT patterns with bright symmetric spots were observed for $2\sqrt{3}\times2\sqrt{3}$ silicene exposed to 10 L and 60 L O_2, implying that partially oxidized silicene maintains the hexagonal honeycomb structure. On the other hand, the FFT pattern displays a typical amorphous feature, indicating the full oxidation of $2\sqrt{3}\times2\sqrt{3}$ silicene phase when the oxygen dose was increased up to 600 L. Furthermore, it is worth noting that some areas of bare Ag(111) substrate were exposed in the fully oxidized silicene, which had not been reported in either experimental or theoretical work before. The binding energy between the epitaxial silicene layer and the Ag(111) surface is about 0.7 eV [28], which is much smaller than that for the Si-O bond [29]. The oxygen thus prefers to first bond with the Si atoms in the silicene rather than the Ag atoms in the substrate. The energy required for the oxygen adsorption on Ag(111) is much higher than that on the Si surface with dangling bonds. Thus, bare Ag(111) surface rather than silver oxide is expected to appear in the fully oxidized silicene sample [28,30,31]. Due to the characteristic sp^3 hybridization of Si, energetically stable Si-O-Si bonds would be expected when silicene is exposed to a high oxygen dose (600 L).

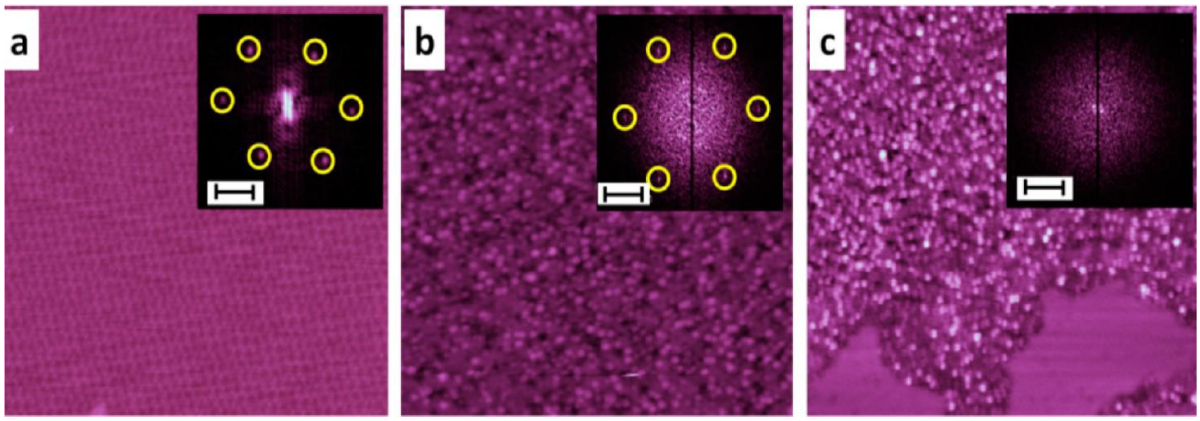

Fig. 5.9 STM images of $2\sqrt{3}\times2\sqrt{3}$ silicene oxidized under (a) 10 L O_2, (b) 60 L O_2, and (c) 600 L O_2. The insets display the corresponding FFT patterns. Bare Ag(111) surface can be seen in the bottom area of (c). The scale bar in each inset stands for 1/nm.

5.4 Summary

In summary, an electronic band gap in monolayer silicene on Ag(111) substrate was produced by oxidation and verified by STM combined with *in-situ* Raman spectroscopy studies. O^d is the most energetically favored configuration for oxygen adsorption on the surfaces of all three silicene superstructures. The different buckled structures lead to different heights of oxygen adatoms on the silicene. The size of the band gap could be modulated from semimetallic to semiconducting type, which can overcome the zero-gap disadvantage of silicene. In fully oxidized silicene, the buckled silicene structure vanishes, with subsequent crumpling of the sample as well as exposure of bare Ag(111) surface areas.

1. B. J. Feng, Z. J. Ding, S. Meng, Y. G. Yao, X. Y. He, P. Cheng, L. Chen, and K. H. Wu, Nano Lett. **12**, 3057 (2012).

2. L. Meng, Y. L. Wang, L. Z. Zhang, S. X. Du, R. T. Wu, L. F. Li, Y. Zhang, G. Li, H. T. Zhou, W. A. Hofer, and H. J. Gao, Nano Lett. **13**, 685 (2013).
3. A. Fleurence, R. Friedlein, T. Ozaki, H. Kawai, Y. Wang, and Y. Yamada-Takamura, Phys. Rev. Lett. **108**, 245501 (2012).
4. J. F. Gao and J. J. Zhao, Sci. Rep. **2**, 861 (2012).
5. A. Kara, H. Enriquez, A. P. Seitsonen, L. C. L. Y. Voon, S. Vizzini, B. Aufray, and H. Oughaddou, Surface Sci. Rep. **67**, 1 (2012).
6. B. Lalmi, H. Oughaddou, H. Enriquez, A. Kara, S. Vizzini, B. Ealet, and B. Aufray, Appl. Phys. Lett. **97**, 223109 (2010).
7. A. O'Hare, F. V. Kusmartsev, and K. I. Kugel, Nano Lett. **12**, 1045 (2012).
8. A. Resta, T. Leoni, C. Barth, A. Ranguis, C. Becker, T. Bruhn, P. Vogt, and G. Le Lay, Sci. Rep. **3**, 2399 (2013).
9. P. Vogt, P. De Padova, C. Quaresima, J. Avila, E. Frantzeskakis, M. C. Asensio, A. Resta, B. Ealet, and G. Le Lay, Phys. Rev. Lett. **108**, 155501 (2012).
10. J. -A. Yan, R. Stein, D. M. Schaefer, X. -Q. Wang, and M. Y. Chou, Phys. Rev. B **88**, 121403 (2013).
11. L. Chen, H. Li, B. J. Feng, Z. J. Ding, J. Qiu, P. Cheng, K. H. Wu, and S. Meng, Phys. Rev. Lett. **110**, 085504 (2013).
12. L. Chen, C. -C. Liu, B. J. Feng, X. Y. He, P. Cheng, Z. J. Ding, S. Meng, Y. G. Yao, and K. H. Wu, Phys. Rev. Lett. **109**, 056804 (2012).
13. C. -C. Liu, W. X. Feng, and Y. G. Yao, Phys. Rev. Lett. **107**, 076802 (2011).
14. R. Quhe, R. Fei, Q. Liu, J. Zheng, H. Li, C. Xu, Z. Ni, Y. Wang, D. Yu, Z. Gao, and J. Lu, Sci. Rep. **2**, 853 (2012).
15. A. K. Geim and K. S. Novoselov, Nat. Mater. **6**, 183 (2007).

16. S. Cahangirov, M. Topsakal, E. Aktürk, H. Sahin, and S. Ciraci, Phys. Rev. Lett. **102**, 236804 (2009).
17. J. F. Gao, J. F. Zhang, H. S. Liu, Q. F. Zhang, and J. J. Zhao, Nanoscale **5**, 9785 (2013).
18. G. Kresse and J. Furthmüller, Phys. Rev. B **54**, 11169 (1996).
19. G. Kresse and D. Joubert, Phys. Rev. B **59**, 1758 (1999).
20. J. P. Perdew, K. Burke, and M. Ernzerhof, Phys. Rev. Lett. **77**, 3865 (1996).
21. A. C. Ferrari, J. C. Meyer, V. Scardaci, C. Casiraghi, M. Lazzeri, F. Mauri, S. Piscanec, D. Jiang, K. S. Novoselov, S. Roth, and A. K. Geim, Phys. Rev. Lett. **97**, 187401 (2006).
22. E. Cinquata, E. Scalise, D. Chiappe, C. Grazianetti, B. van den Broek, M. Houssa, M. Fanciulli, and A. Molle, J. Phys. Chem. C **117**, 16719 (2013).
23. H. Enriquez, S. Vizzini, A. Kara, B. Lalmi, and H. Oughaddou, J. Phys.: Condens. Matter **24**, 314211 (2012).
24. A. Hartstein, J. C. Tsang, D. J. Dimaria, and D. W. Dong, Appl. Phys. Lett. **36**, 836 (1980).
25. D. Chiappe, C. Grazianetti, G. Tallarida, M. Fanciulli, and A. Molle, Adv. Mater. **24**, 5088 (2012).
26. R. Wang, X. Pi, Z. Ni, Y. Liu, S. Lin, M. Xu, and D. Yang, Sci. Rep. **3**, 3507 (2013).
27. Z. Liu, K. Suenaga, P. J. F. Harris, and S. Iijima, Phys. Rev. Lett. **102**, 015501 (2009).
28. W. X. Li, C. Stampfl, and M. Scheffler, Phys. Rev. B, **65**, 075407 (2002).
29. R. Q. Zhang, T. S. Chu, H. F. Cheung, N. Wang, and S. T. Lee, Phys. Rev. B **64**, 113304 (2001).
30. D. Beeman, R. Tsu, and M. F. Thorpe, Phys. Rev. B **32**, 874 (1985).
31. U. Höfer, A. Puschmann, and D. Coulman, Surf. Sci. **211**, 948 (1989).

CHAPTER 6

EFFECTS OF OXYGEN ADSORPTION ON THE SURFACE STATE OF EPITAXIAL SILICENE ON AG(111)

Epitaxial silicene shows a strong interaction with the substrate that dramatically affects its electronic structure. The role of electronic coupling in the chemical reactivity between the silicene and the substrate is still unclear so far. In this chapter, we report the reconstructions and hybridized electronic structures of epitaxial 4×4 silicene (with respect to Ag(111)) on Ag(111) by using STM and ARPES. The hybridization between Si and Ag induces a metallic surface state, which can gradually decay by oxygen adsorption. XPS results reveal the decoupling of Si-Ag bonds as well as the relatively great oxygen resistance of the Ag(111) surface after oxygen treatment. First-principles calculations have also illustrated the evolution of the electronic structure of silicene during oxidation. It has been demonstrated experimentally and theoretically that the high chemical activity of 4×4 silicene is attributable to the Si p_z state, while the Ag(111) substrate exhibits relatively inert chemical behavior.

6.1 Introduction

Silicene, one single layer of silicon atoms packed in a honeycomb structure, has been predicted to be a new 2D Dirac-fermion material [1–3]. Due to the linear energy-momentum dispersion relation at the Dirac point, the electrons in silicene behave as massless charge carriers exhibiting an ultra-fast transport velocity [4–6]. Its strong SOC makes silicene a promising candidate material for the QSHE [5] and gives it compatibility with current Si-based device technologies. To date, epitaxial growth is the only method to produce silicene on certain metal substrates [7–9]. The electronic structure of such epitaxial silicene is

therefore significantly modified by a strong coupling with the substrate, annihilating its Dirac-fermion characteristics [10]. On the other hand, epitaxial silicene in different superstructures may show various exotic physical and chemical properties due to new surface states resulting from hybridization between Si and the underlying metal substrate. DFT simulations have predicted that in 4×4 silicene [with respect to Ag(111)] on Ag(111), wave functions derived from the Si 3*p* orbitals are delocalized into the substrate. The strong coupling, accompanied by the charge transfer from the substrate to the silicon, breaks the symmetry and modulates the band structure of 4×4 silicene. Consequently, a surface metallic band was observed in 4×4 silicene on Ag(111) by ARPES measurements [11]. This metallic band would induce higher chemical reactivity in the silicene, especially on the surface rather than the edges, potentially facilitating silicene functionalization. The chemical properties associated with such a hybrid electronic state in 4×4 silicene are still unknown, which is an obstacle to potential applications of silicene. Due to the high chemical activity, oxygen could be used to probe and modulate local electronic states at the atomic level in 2D materials via the adsorption process. It is well accepted that the local electronic structure can be modulated from the zero-gap state to a semiconducting state by changing the oxygen dose and the adsorption sites of oxygen adatoms in graphene [12], reflecting the intrinsic electronic properties of graphene. Silicene possesses high chemical reactivity towards oxygen, providing a feasible way to research its surface electronic structures by using the oxygen adatom as a chemical probe [1]. The hybrid surface metallic state in 4×4 silicene on Ag(111) would be perturbed by oxygen adatoms via the formation of covalent bonds between oxygen atoms and silicon atoms (or silver atoms). Modulation of electronic states in silicene by oxygen adatoms is also expected, which is crucial for application in electronic devices.

In this work, we report the effects of oxygen adsorption on the surface state of epitaxial 4×4 silicene on Ag(111), as determined by STM and ARPES at the atomic level. The hybridized

surface metallic state is found to be highly sensitive to oxygen adatoms. It is revealed that the Shockley surface state on Ag(111) can be revived after the covered silicene is oxidized. DFT simulations imply that the high chemical reactivity of 4×4 silicene results from the Si p_z state, consistent with the experimental results.

6.2 Experimental methods

6.2.1 Sample preparation

The silicene layers were deposited on Ag(111) substrate by the evaporation of a heated silicon wafer in a preparation chamber attached to a low temperature (LT)-STM system under UHV (< 5×10^{-11} torr). A clean Ag(111) substrate was prepared by Ar^+ sputtering, followed by annealing at 550 ˚C for several cycles. The deposition flux of Si was 0.08 monolayers per minute (ML/min). The temperature of the Ag(111) substrate was kept at 220 ˚C during deposition. Oxygen molecules were introduced onto the silicene surface by a leak valve. The Langmuir (L) is used as the unit of exposure of O_2, where 1 L is defined as exposure to 10^{-6} torr O_2 in one second.

6.2.2 STM and STS characterizations

The STM and STS measurements were carried out on a LT-STM system (SNOM1400, Unisoku Co.) in UHV (< 8×10^{-11} torr) at 77 K. STS differential conductance (dI/dV) (where I is current and V is voltage) measurements were conducted with lock-in detection by applying a small modulation of 20 mV to the tunnel voltage at 973 Hz. Before STS measurements, the Pt/Ir tip was calibrated on a silver surface.

6.2.3 ARPES and XPS characterizations.

In-situ ARPES and XPS characterizations were conducted at a photoelectron spectroscopy station in the Beijing Synchrotron Radiation Facility (BSRF) using a SCIENTA R4000 analyzer. A monochromatized He-I light source with energy of 21.2 eV was applied for the band dispersion measurements. The total energy resolution was set at 15 meV, and the angular resolution was set to ~ 0.3˚, giving momentum resolution of ~ 0.01 $A^{\circ -1}$. The XPS experiments were performed at Beamline 4B9B, and the variable photon energies used were referenced to a fresh Au polycrystalline film. Photons, located at 700 eV, 500 eV, and 180 eV, were used to excite the Ag-3*d* and Si-2*p* electrons in the samples, and the energy resolutions were around 0.4 meV, 0.3 meV, and 0.15 meV, respectively. All the XPS data are fitted using the XPS Peak 4.1 software package. All the background subtraction was calculated by the ‘‘Shirley + Linear’’ background approach. All XPS peaks were fitted by Gaussian-Lorentzian functions. The silicene samples used in the ARPES and XPS characterizations were prepared under the same conditions as in STM and STS characterizations.

6.2.4 DFT calculation details

We performed DFT simulations and *ab initio* molecular dynamics (AIMD) simulations using the VASP [13–15]. The exchange-correlation PBE functional and the ion-electron interaction as described by the projector augmented wave method were used [16,17]. A plane-wave basis set with an energy cut-off of 400 eV was used with a Monkhorst-Pack *k*-point mesh of 13×13×1 for the geometry optimization and the Γ point for the AIMD. The 4×4 silicene/Ag(111) system was modelled using details published previously [18]. To simulate adsorption of oxygen in this system, we initially put oxygen atoms in top sites above the Si atoms at 1/2ML coverage. A geometry optimization was calculated using medium precision, following by high precision. During the optimization process, the bottom 2 layers of Ag atoms were kept fixed, while all other atoms were allowed to relax until the total energy

converged to < 10^{-4} eV, and the Hellmann–Feynman force on each of the atoms was allowed to relax to < 0.03 eV $Å^{-1}$. An *ab-initio* molecular dynamics simulation of 7 ps, using a time step of 1 fs, showed that the Si layer becomes disordered and starts to delaminate from the Ag surface and to form a silicon oxide type structure.

6.3 Results and discussion

6.3.1 STM and STS results of oxidized 4×4 silicene

Figure 6.1 shows 15×15 nm^2 STM topographical images of the Ag(111) surface and a 4×4 silicene monolayer epitaxially grown on the substrate. Quantum-interference patterns are clearly visible on the Ag(111) surface, as shown in Fig. 6.1 (a). Electrons in the two dimensional surface states can be scattered by surface point defects, leading to periodic spatial oscillations of LDOS [19]. The LDOS can be used to classify a 2D electron gas, due to the fact that interference will occur if the 2D electron wave travels towards a scattering defect and encounters the backscattered wave [20]. In Fig. 6.1 (a), the quantum-interference pattern with a period of several tens of angstroms reflects the nature of the 2D electron wave in the Ag(111) substrate. The 4×4 silicene has a lattice constant of 1.06 nm, as shown in Fig. 6.1 (b). The low-buckled configuration can be verified by the different heights of the Si atoms at the edges. The height of buckling is 0.86 Å in 4×4 silicene, distinguishing it from the calculated value for free-standing 1×1 silicene [21,22]. This is evoked by the metal passivation effect of the Ag(111) surface, which affects the buckling of silicene through bonding between Si and Ag(111). There was no quasiparticle interference pattern (QPI) that could be observed in the as-grown silicene layer, implying the absence of Dirac fermion characteristics in epitaxial 4×4 silicene. Theoretical works have predicted that the

hybridization between Si and Ag induces symmetry breaking in 4×4 silicene, and suppresses the Dirac quasiparticles [10,11]. The strong coupling, accompanied by the charge transfer, modulates the electronic structure of silicene on Ag(111). In order to reveal the nature of the hybridization state, we introduced oxygen molecules onto the 4×4 silicene surface by a leak valve in precise doses at 77 K.

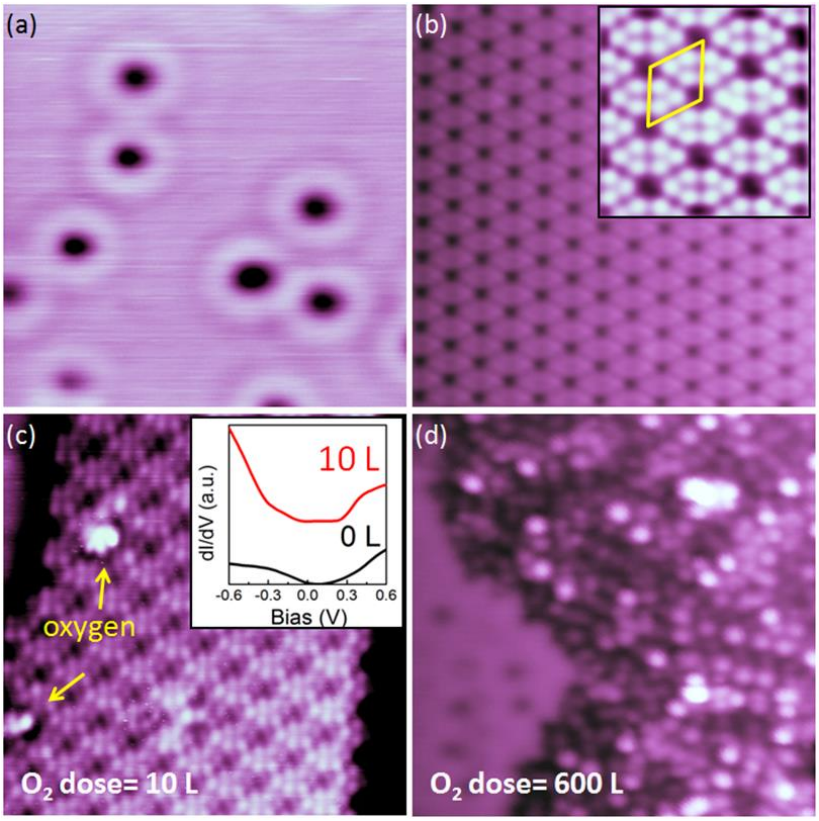

Fig. 6.1 Topographical images of Ag(111) substrate and 4×4 silicene grown on Ag(111). (a) STM topographical image of clean Ag(111) substrate, where a clear quantum-interference pattern due to point defects appears (scanning area 15 nm×15 nm, V_{bias} = -0.2 V, I = 4 nA). (b) STM topographical image of 4×4 silicene on Ag(111) (scanning area 15 nm×15 nm, V_{bias} = -0.8 V, I = 2 nA). Inset is an enlarged view of an area 4 nm×4 nm in size. (c) STM image of silicene layer oxidized by oxygen with a dose of 10 L. O adatoms prefer to reside at bridge sites. Inset contains the comparative STS spectra of silicene and silicene oxide samples. (d) STM images of the 4×4 silicene oxidized under 600 L O_2. The bare Ag(111) surface can be seen in the bottom left area of (d).

Figure 6.1 (c) and (d) shows typical STM images of silicene layers after exposure to 10 L and 600 L O_2, respectively. At the low oxygen dose level, the oxygen adatoms prefer to reside on a bridging site forming a Si(TL)-O-Si(BL) configuration. The Si-O bonds significantly modulate the surface metallic band in silicene on Ag(111). As shown in the inset of Fig. 6.1 (c), a gapped electronic state was identified in STS measurements performed at the oxygen adatom sites. The surface metallic band is tuned to semiconducting-like behavior. When the oxygen dose is increased up to 600 L, the silicene layer is oxidized and forms a disordered structure, as shown in Fig. 6.1 (d). Furthermore, some areas of bare Ag(111) substrate were exposed. Interestingly, the QPI pattern is revived on the Ag(111) surface with the same oscillating period as that on clean Ag(111) surfaces, indicating that the Ag(111) substrate is inert compared to 4×4 silicene in the process of oxidization.

6.3.2 Electronic structure of oxidized 4×4 silicene by ARPES measurements

Figure 6.2 displays the ARPES results on occupied states along the Γ-M_{Ag} and Γ-K_{Ag} directions of 4×4 silicene/Ag(111) for samples both before and after oxidization, in order to determine the details of the surface electronic structures as well as the cause of the electronic hybridization between the silicene and the Ag(111) substrate. Figure 6.2 (d) shows the reciprocal spaces BZ of (1×1) Ag(111) (blue hexagon) and (4×4) silicene (orange hexagons). Note that the M_{Ag} and K_{Ag} points of Ag(111) coincide with the Γ and K_{Si} points of 4×4 silicene in the BZ. Figure 6.2 (a) displays the Shockley surface state (SSS) of the Ag(111) substrate at the BZ centre Γ point (k = 0 $Å^{-1}$). The SSS originates primarily from surface states of nearly free electrons and is associated with the special boundary conditions introduced by the metal/vacuum interface [23]. The typical bulk *sp*-band of Ag is located across the Fermi level [11] at k = 1.15 $Å^{-1}$. With increasing silicene coverage, the SSS and *sp*-band of Ag become faint and eventually disappear at the moment when the Ag(111)

surface is fully covered by the silicene layer, as shown in Fig. 6.2 (b). The weak Ag *sp*-band is still visible, implying that this band remains stable after Si deposition. There is a clear new "∩"-shaped state with a top point located exactly at M_{Ag} point, or Γ point for 4×4 silicene. Furthermore, the "∩"-shaped state displays variation along the Γ-K_{Ag} direction, as shown in Fig. 6.2 (e), where the band crosses the Fermi surface at the K_{Ag} (K_{Si}) point. The results for band structures along both the Γ-M_{Ag} and the Γ-K_{Ag} directions are consistent with the previous reports [11], demonstrating that the new "∩"-shaped state should be ascribed to a hybridization between Si and Ag orbitals resembling the π-band dispersion in graphene [11]. The apex of the state at k = 1.28 $Å^{-1}$ in Fig. 6.2 (b) is about 0.15 eV below the Fermi level. The value is at the saddle point of the surface state and midway between two adjacent K_{Ag} (K_{Si}) points. It should be noted that this feature, which appears only after Si deposition, is absent from clean Ag(111) spectra and has been associated with a Ag(111)-related surface band. The predicted Dirac cone has been observed in different √3×√3 silicene with respect to 1×1 silicene, which was formed as a second layer on 4×4 silicene grown on Ag(111) substrate [24,25], and it was revealed that √3×√3 silicene is a true 2D Dirac-fermion material. A strong electron doping (*n*-type) effect has been revealed in multilayer √3×√3 silicene that originates from the Ag(111) substrate, as indicated by both ARPES and STS measurements [6,24]. Consequently, the Fermi level in multilayer silicene is raised by about 0.3 eV, even though there is hybridized state can be detected. Therefore, the electronic structure of monolayer 4×4 silicene is totally dissimilar to that of multilayer √3×√3 silicene. High surface chemical activity could be expected in 4×4 silicene due to its lower work function, which is induced by the metallic hybridized surface band (HSB) in 4×4 silicene compared with that of √3×√3 silicene. Figure 6.2 (c) and (f) displays ARPES images on an oxidized 4×4 silicene/Ag(111) sample under an oxygen dose of 600 L along the Γ-M_{Ag} and Γ-K_{Ag} directions, respectively. The two ARPES results show band structures that are similar to each other.

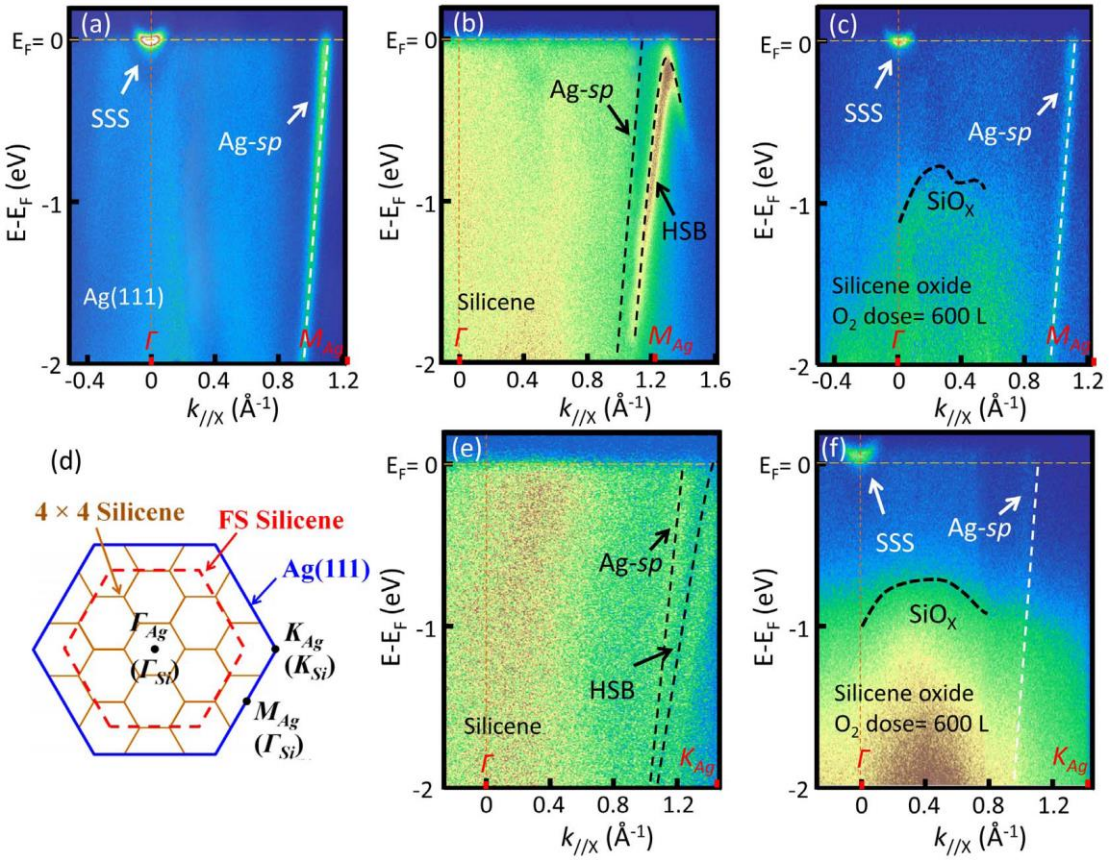

Fig. 6.2 Energy vs. *k* dispersion measured by ARPES for (a) clean Ag(111) surface, (b) 4×4 silicene grown on Ag(111), and (c) oxidized silicene on Ag(111), respectively. SSS in (a) and (b) denotes the Shockley surface state. HSB in (b) denotes the hybrid surface band. (d) Schematic diagram of the BZ for 4×4 silicene grown on Ag(111): blue and orange honeycomb structures correspond to Ag(111) and 4×4 silicene, respectively. (e) 4×4 silicene grown on Ag(111) along the Γ-K_{Ag} direction, and (f) oxidized silicene on Ag(111) along the Γ-K_{Ag} direction, respectively.

The disappearance of the signature of metallic HSB is combined with the presence of well-defined SSS bands in the oxidized silicene/Ag(111) sample. The intensities of the states belonging to Ag(111) are weak because the Ag(111) surface is still partly covered by silicene oxide. Moreover, an asymmetric band with its highest energy level at about -0.6 eV can be perceived in Fig. 6.2 (c). STS measurements on areas of the Ag(111) surface and silicene oxide in the same sample were carried out to clarify the derivation of this asymmetric band. An energy gap with the value of 1.2 eV was opened up in silicene oxide sites, while the

Ag(111) displayed typical metallic characteristics. Thus, the asymmetric state is attributed to the valence band (VB) resulting from silicene oxide. These results are consistent with the STM observations shown in Fig. 6.1 (d), where amorphous silicene oxide shields most of the Ag(111) surface. Due to the extreme surface sensitivity of SSS in metal, the SSS reflects modifications of the surface atomic and electronic properties [26,27]. The revived SSS in the ARPES results for the oxidized sample indicates that oxygen would preferentially react with Si atoms rather than silver atoms if the oxygen dose is low. Consequently, 4×4 silicene chemically protects the surface states of Ag(111) against oxygen molecules. The disappearance of the HSB in Fig. 6.2 (c) and (f) demonstrates that the bonding between Si and Ag is broken after oxidation.

6.3.3 XPS spectra for oxidization effect

A detailed XPS characterization of the chemical bond states in the samples was carried out to investigate the influence of oxygen adatoms on the hybridization between Ag(111) and 4×4 silicene. Figure 6.3 (a) and (b) shows Ag 3*d* core level XPS spectra for 4×4 silicene deposited on an Ag(111) sample before and after oxidization, respectively. The experimental data points are plotted with black dots, while the fitted curves are displayed by red lines. For the bare Ag(111) substrate, the Ag $3d_{3/2}$ and $3d_{5/2}$ peaks located at 371.5 eV and 365.5 eV originate from Ag-Si bonds. A downward energy shift with a value of ~ 0.7 eV for the Ag 3*d* orbitals is detected after the deposition of silicene, implying that the chemical activity of silicene is higher than that of the pure Ag-Ag bonds arising from Ag^0. Peak splitting of the Ag 3*d* line was observed after exposure to 600 L oxygen, as shown in Fig. 6.3 (b). The peaks could be decomposed into two components, arising from the Ag-Ag bonds and the Ag-Si bonds, respectively. The dramatic fall in intensity of the Ag-Si bonds and recovery of the Ag-Ag bonds demonstrate that Ag-Si bonds are broken after the oxygen treatment. Furthermore, no

Ag-O chemical structure is present in the XPS spectrum, indicating that oxygen molecules most likely bond to silicon atoms, consisting with the resurgence of the QPI pattern in Fig. 6.1 (d). Figure 6.3 (c) and (d) displays Si 2*p* core level spectra for the sample before and after oxidization, respectively. The fitting results for the Si 2*p* line, as shown in Fig. 6.3 (c), manifests the existence of two groups of bonding components, labelled as Si1 and Si2, respectively. The energy gap between the two peaks in each group is a constant value, indicates that the two fitting peaks in each group are attributable to two Si $2p_{3/2}$ and $2p_{1/2}$ peaks, respectively. The Si2 peaks located at a binding energy around 98.8 eV are correlated with elemental silicene, consistent with a previous report [28]. Since there are no other elements introduced in the process of deposition, combined with the fitting results of Ag-Si bonding in Fig. 6.3 (a) and (b), the Si1 group is ascribed to Si-Ag bonding. After the oxygen treatment, clear silicon oxide peaks appear. The binding energy value (101.6 eV) is lower than the peak position of SiO_2-like binding energy (102.3 eV) [29], implying lower valence states of the Si-O bonds compared with Si^{4+}. The low valence of Si-O bonds agrees well with our STM results and a previous report [30], implying that the oxygen adatoms are the most energetically favourable on the surface of silicene. The intensity of the peaks correlated to the Si-Ag bonds shows a significant decrease in the presence of silicon oxide peaks. The change in peak intensity demonstrates that the main role of oxygen adatoms is to decouple the Si-Ag bonds rather than the Si-Si bonds. The XPS results agree with our STM and ARPES results, confirming the decoupling of Si-Ag bonds after oxygen treatment, as well as the strong relatively oxygen resistance of the Ag(111) surface.

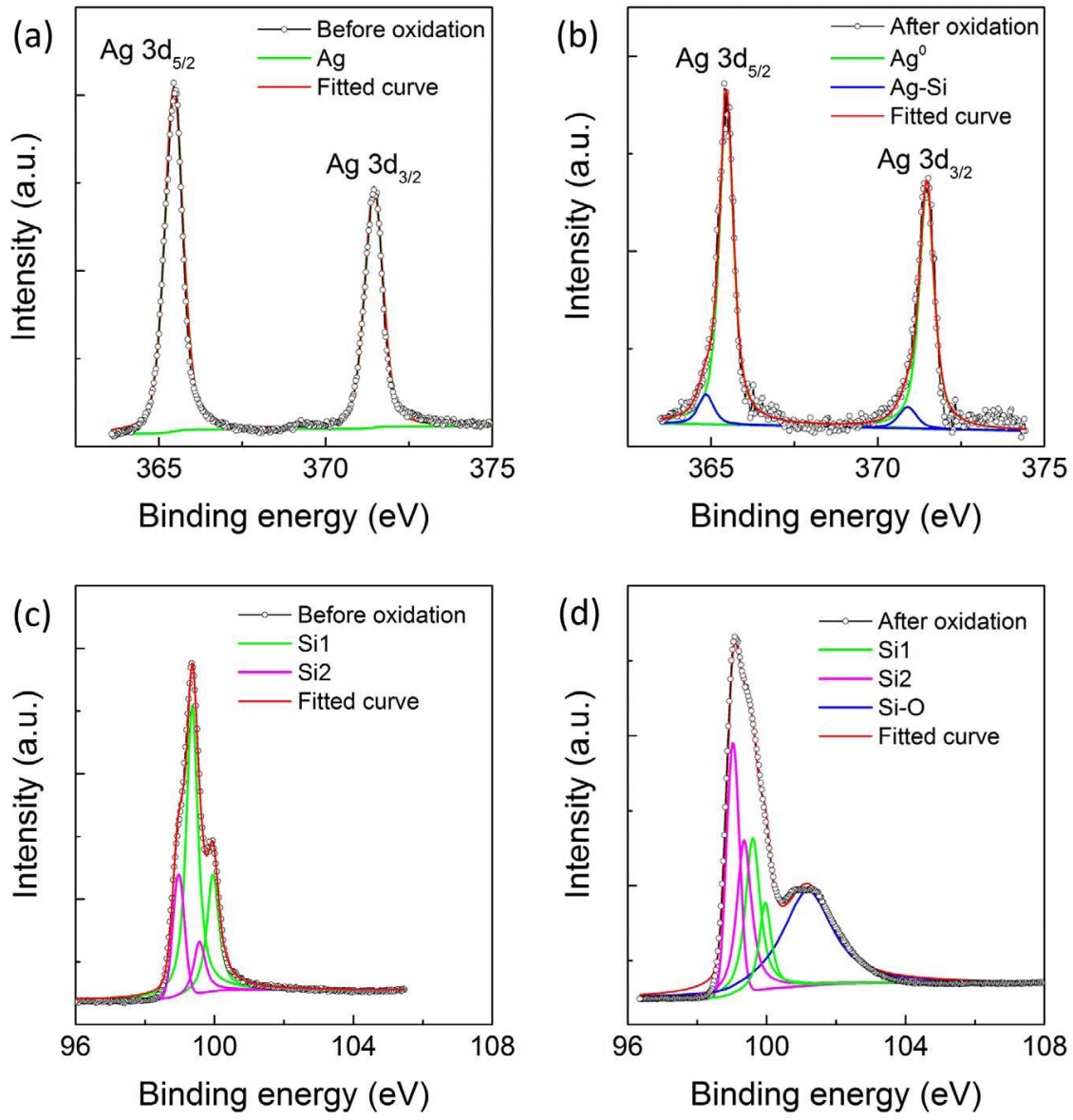

Fig. 6.3 Representative Ag 3*d* core level XPS spectra of 4×4 silicene on Ag(111) (a) before and (b) after oxidation, respectively. Si 2*p* core level XPS spectra of 4×4 silicene on Ag(111) (c) before and (d) after oxidation. The spectra imply that the 4×4 silicene layer is oxidized and decoupled from Ag(111) under the high oxygen dose (600 L).

6.3.4 DFT simulations of SSS and HSB

Finally, we carried out DFT calculations to investigate the revived SSS on Ag(111) and to reveal the origins of the VB in silicene oxide, as shown in Fig. 6.4. The first step in our simulation was to modulate the superstructure of silicene grown on Ag(111). One atomic

layer of silicene was put on top of 3 layers of 4×4 Ag(111). The simulated structure shows exhibits same reconstruction as in our STM results, as shown in Fig. 4(a). The Ag *d*-state and the Si *p*-state make the heaviest contributions to the DOS at the Fermi level (E_F), implying that the metallic HSB should indeed be ascribed to the p_z electrons of Si atoms and the 4*d* electrons of the Ag(111) substrate. We then put 0.5 ML oxygen on the stabilized silicene surface. After running the molecular dynamics simulation for 7 ps, the singly coordinated Si atoms transfer to bridge sites, demonstrating that there is an energy barrier for the other O atoms to move to more highly coordinated sites on silicene. Meanwhile, the Si atomic layer becomes disordered, indicating that the silicene oxide layer starts to decouple from the underlying Ag(111) substrate. The disordering of the Si overlayer evoked by oxygen adatoms is in excellent agreement with the STM images demonstrating the amorphous nature of silicene oxide. Figure 6.4 (c) shows the simulated DOS on 4×4 silicene with 0.5 ML oxygen coverage. The deep-level band (< -2 eV) is primarily contributed by Ag *d*-states. The DOS close to E_F, however, contains Ag, Si, and O orbitals, as displayed in the inset of Fig. 6.4 (c). It should be pointed out that the Si 3*p* states and O 2*p* states form a new band below E_F, although Si and O contribute partly to the DOS at E_F. The top of this band is at -0.4 eV, matching well with the asymmetric band (-0.6 eV) in the ARPES results [Fig. 6.2 (c) and (f))]. Therefore, this shallow band is ascribed to the VB of partially oxidized silicene. It should be noted that 0.5 ML oxygen is not enough to oxidize the whole silicene monolayer, so that the hybridization between Si and Ag still exists in some regions and could be detected in the STM and ARPES results. For areas of silicene oxide, the SSS would be revived due to the decoupling between the silicene overlayer and the Ag(111). The Ag state at the Fermi level could be contributed by both the metallic HSB and the revived SSS.

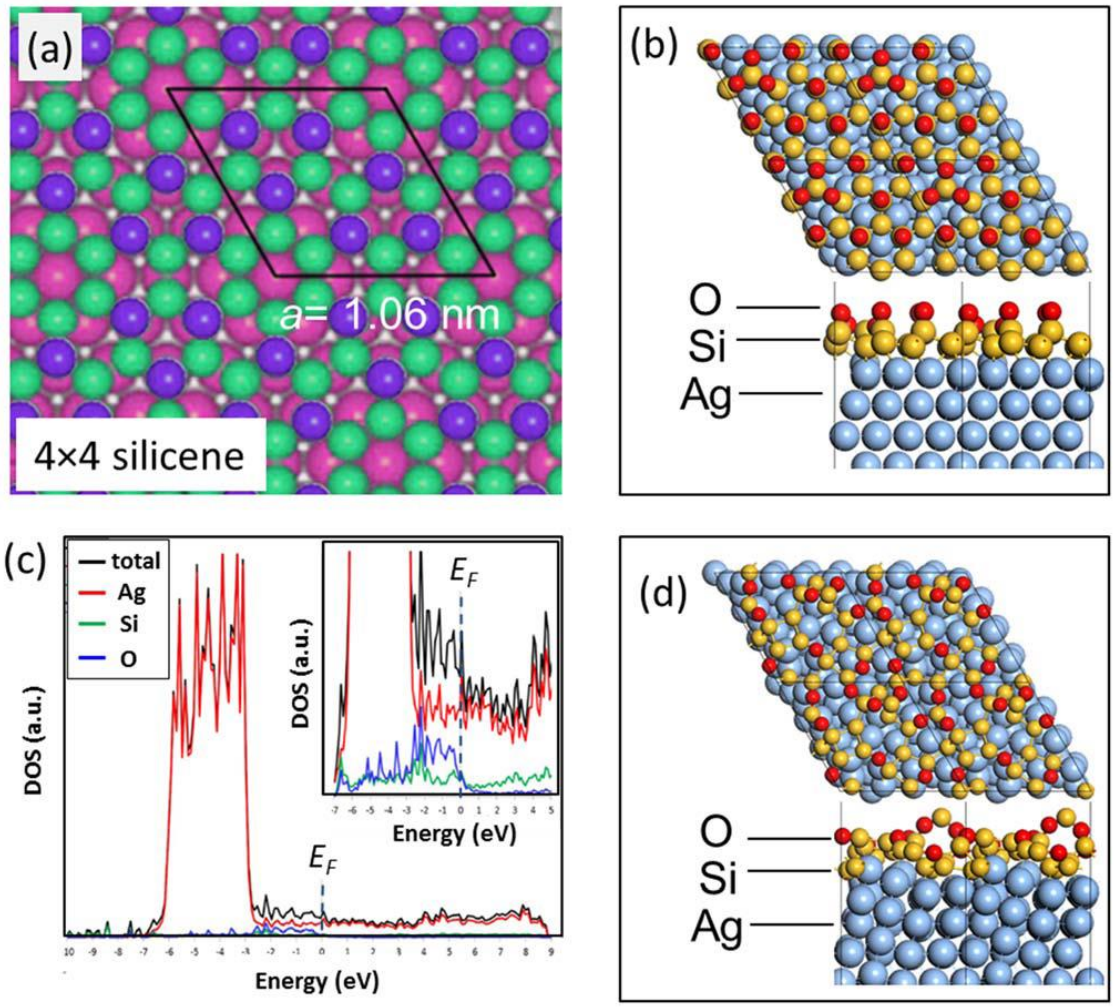

Fig. 6.4 (a) DFT-simulated structure of 4×4 silicene on Ag(111) substrate, with the black rhombus showing the unit cell. (b) Initial adsorption sites of oxygen adatoms on silicene. (c) Simulated DOS of oxidized silicene with oxygen coverage of 1/2ML. The inset shows an enlarged view of the DOS close to the Fermi level. (d) The energy favoured stable adsorption sites after running the molecular dynamics simulation for 7 ps. Oxygen adatoms prefer to form Si-O-Si bonds at bridge sites in the 4×4 silicene surface. Red, yellow, and blue balls in (b) and (d) label oxygen, silicon, and silver atoms, respectively.

As mentioned above, 4×4 silicene on Ag(111) shows high chemical reactivity towards oxygen, which is the property that has been utilized to further functionalize epitaxial silicene layers. The binding energy between the epitaxial silicene layer and the Ag(111) surface, which is about 0.7 eV [31], is much smaller than that for Si-O (between 4.0 and 12.0 eV) [32]. The oxygen thus tends to bond firstly with Si atoms in the silicene rather than Ag atoms

in the substrate. Moreover, the energy of oxygen adsorption on the Ag(111) surface is much higher than that on the Si surface with dangling bonds (p_z orbital). Therefore, bare Ag(111) surface rather than silver oxide appears in the fully oxidized silicene sample [31,33]. Due to the typical sp^3 hybridization of Si, energetically favoured Si-O-Si bonds would be expected when silicene is exposed to a high oxygen dose (600 L). The Si-O bond length in oxidized 4×4 silicene on Ag(111) is around 1.63 Å, which is derived from our DFT simulations, and is much smaller than the bond length of Si-O in SiO_2 (~ 1.70 Å). Consequently, the silicene layer crumples after oxidation, leading to the presence of some "silicene-free" areas. Our theoretical and experimental results also give a clue that the silicene oxide layer could possibly detach from the Ag(111) substrate and form quasi-freestanding amorphous nanosheets. By analogy with graphene, it is proposed that reducing these quasi-freestanding nanosheets may provide a feasible way to achieve free-standing silicene nanosheets (or reduced silicene oxide).

6.4 Summary

In conclusion, we have studied the oxidation effects on the structure and electronic properties of 4×4 silicene on Ag(111). After oxidation, the silicene oxide exhibits an amorphous structure with a semiconductor-like band structure. By combining DFT calculations and ARPES results, it was proved that the 2D metallic surface state in 4×4 silicene on Ag(111) should be ascribed to the hybridization of Si p_z and Ag 3*d* states. The hybridization is broken, and the Ag(111) Shockley surface state could be revived after the silicene is oxidized. This surface band demonstrates high chemical activity, facilitating chemical functionalization of silicene layers.

1. S. Cahangirov, M. Topsakal, E. Aktürk, H. Şahin, and S. Ciraci, Phys. Rev. Lett. **102**, 236804 (2009).
2. G. G. Guzmán-Verri and L. C. Lew Yan Voon, Phys. Rev. B **76**, 075131 (2007).
3. S. Lebègue and O. Eriksson, Phys. Rev. B **79**, 115409 (2009).
4. A. Kara, H. Enriquez, A. P. Seitsonen, L. C. L. Y. Voon, S. Vizzini, B. Aufray, and H. Oughaddou, Surface Sci. Rep. **67**, 1 (2012).
5. C. -C. Liu, W. X. Feng, and Y. G. Yao, Phys. Rev. Lett. **107**, 076802 (2011).
6. L. Chen, C. -C. Liu, B. J. Feng, X. Y. He, P. Cheng, Z. J. Ding, S. Meng, Y. G. Yao, and K. H. Wu, Phys. Rev. Lett. **109**, 056804 (2012).
7. B. J. Feng, Z. J. Ding, S. Meng, Y. G. Yao, X. Y. He, P. Cheng, L. Chen, and K. H. Wu, Nano Lett. **12**, 3057 (2012).
8. P. Vogt, P. De Padova, C. Quaresima, J. Avila, E. Frantzeskakis, M. C. Asensio, A. Resta, B. Ealet, and G. Le Lay, Phys. Rev. Lett. **108**, 155501 (2012).
9. L. Meng, Y. L. Wang, L. Z. Zhang, S. X. Du, R. T. Wu, L. F. Li, Y. Zhang, G. Li, H. T. Zhou, W. A. Hofer, and H. J. Gao, Nano Lett. **13**, 685 (2013).
10. C. -L. Lin, R. Arafune, K. Kawahara, M. Kanno, N. Tsukahara, E. Minamitani, Y. Kim, M. Kawai, and N. Takagi, Phys. Rev. Lett. **110**, 076801 (2013).
11. D. Tsoutsou, E. Xenogiannopoulou, E. Golias, P. Tsipas, and A. Dimoulas, Appl. Phys. Lett. **103**, 231604 (2013).
12. A. K. Geim and K. S. Novoselov, Nat. Mater. **6**, 183 (2007).
13. G. Kresse and J. Furthmüller, Phys. Rev. B **54**, 11169 (1996).
14. G. Kresse and J. Furthmüller, Comput. Mater. Sci. **6**, 15 (1996).
15. G. Kresse and J. Hafner, Phys. Rev. B **47**, 558 (1993).
16. P. E. Blöchl, Phys. Rev. B **50**, 17953 (1994).

17. J. P. Perdew, K. Burke, and M. Ernzerhof, Phys. Rev. Lett. **77**, 3865 (1996).

18. T. Morishita, M. J. S. Spencer, S. Kawamoto, and I. K. Snook, J. Phys. Chem. C **117**, 22142 (2013).

19. M. F. Crommie, C. P. Lutz, and D. M. Eigler, Science **262**, 218 (1993).

20. M. F. Crommie, C. P. Lutz, and D. M. Eigler, Nature **363**, 524 (1993).

21. J. -A. Yan, R. Stein, D. M. Schaefer, X. -Q. Wang, and M. Y. Chou, Phys. Rev. B **88**, 121403 (2013).

22. E. Scalise, M. Houssa, G. Pourtois, B. van den Broek, V. Afanas'ev, and A. Stesmans, Nano Res. **6**, 19 (2013).

23. A. Krönlein, J. Kemmer, P. J. Hsu, and M. Bode, Phys. Rev. B **89**, 155413 (2014).

24. P. De Padova, P. Vogt, A. Resta, J. Avila, I. Razado-Colambo, C. Quaresima, C. Ottaviani, B. Olivieri, T. Bruhn, T. Hirahara, T. Shirai, S. Hasegawa, M. C. Asensio, and G. Le Lay, Appl. Phys. Lett. **102**, 163106 (2013).

25. J. Avila, P. De Padova, S. Cho, I. Colambo, S. Lorcy, C. Quaresima, P. Vogt, A. Resta, G. Le Lay, and M. C. Asensio, J. Phys.: Condens. Matter **25**, 262001 (2013).

26. T. Andreev, I. Barke, and H. Hövel, Phys. Rev. B **70**, 205426 (2004).

27. H. Hövel, B. Grimm, and B. Reihl, Surf. Sci. **477**, 43 (2001).

28. A. Molle, C. Grazianetti, D. Chiappe, E. Cinquanta, E. Cianci, G. Tallarida, and M. Fanciulli, Adv. Funct. Mater. **23**, 4340 (2013).

29. F. J. Himpsel, F. R. McFeely, A. Taleb-Ibrahimi, J. A. Yarmoff, and G. Hollinger, Phys. Rev. B **38**, 6084 (1988).

30. Y. Du, J. C. Zhuang, H. S. Liu, X. Xu, S. Eilers, K. H. Wu, P. Cheng, J. J. Zhao, X. D. Pi, K. W. See, G. Peleckis, X. L. Wang, and S. X. Dou, ACS Nano **8**, 10019 (2014).

31. W. X. Li, C. Stampfl, and M. Scheffler, Phys. Rev. B **65**, 075407 (2002).

32. R. Q. Zhang, T. S. Chu, H. F. Cheung, N. Wang, and S. T. Lee, Phys. Rev. B **64**, 113304 (2001).

33. U. Höfer, A. Puschmann, and D. Coulman, Surf. Sci. **211**, 948 (1989).

CHAPTER 7

QUASI-FREE-STANDING EPITAXIAL SILICENE ON AG(111) BY OXYGEN INTERCALATION

Silicene is a monolayer allotrope of silicon atoms arranged in a honeycomb structure with massless Dirac fermion characteristics, similar to graphene [1-5]. It is favourable for the development of silicon-based multifunctional nanoelectronic and spintronic devices operated at room temperature [6-8] due to its strong spin-orbit coupling. Nevertheless, until now, silicene could only be epitaxially grown on conductive substrates. The strong silicene-substrate interaction may depress its superior electronic properties [9,10]. Here, we report a quasi-free-standing silicene layer that has been successfully obtained through oxidization of bilayer silicene on the Ag(111) surface. The oxygen atoms intercalate into the underlayer of silicene, which can isolate the top layer of silicene from the substrate. In consequence, the top layer of silicene exhibits the signature of a 1×1 honeycomb lattice and hosts massless Dirac fermions due to much less interaction with the substrate. Furthermore, the oxidized silicon buffer layer is expected to serve as an ideal dielectric layer for electric gating in electronic devices. These findings are relevant for the future design and application of silicene-based nanoelectronic and spintronic devices.

7.1 Introduction

Silicene, in a similar way to graphene, is expected to exhibit exciting and rich physics from theoretical calculations, including massless Dirac fermions, the QSHE, and possible superconductivity [1-8,11,12]. In equilibrium low-buckled silicene, silicon atoms adopt sp^2/sp^3 mixed hybridization states [13], and it requires an appropriate substrate to saturate its

out-of-plane dangling bonds. This seems to be the reason why monolayer silicene sheets must be fabricated on only a few conductive substrates by the epitaxial growth method [2-5]. The strong silicene-substrate interaction, however, may greatly depress the superior electronic properties in this 2D material [9,10]. For example, the hybridization between Ag and Si orbitals results in a surface metallic band and depresses the Dirac fermion characteristics in an epitaxial silicene layer on an Ag(111) surface [10]. Moreover, the conductive substrate makes it difficult to modulate the Fermi level of silicene by electric gating, and thus, hinders integration of silicene into microelectronic devices. Hence, how to eliminate or minimize substrate effects on the structural and electronic characteristics of epitaxial silicene has become a critical issue for the development of silicene devices. Although some theoretical proposals have been put forward to achieve quasi-free-standing silicene on inert substrates [14-16], so far there has been barely any experimental success.

In bilayer silicene on Ag(111), the top $\sqrt{3}\times\sqrt{3}$ layer (with respect to 1×1 silicene) is considered to be fabricated on the $\sqrt{13}\times\sqrt{13}/4\times4$ layer [with respect to 1×1 Ag(111)] underneath [17]. Therefore, the lower $\sqrt{13}\times\sqrt{13}/4\times4$ layer can be regarded as a buffer layer. Convincing experimental evidence suggests that the $\sqrt{3}\times\sqrt{3}$ layer has more sp^2 hybridization states and excellent chemical stability [18], while the $\sqrt{13}\times\sqrt{13}/4\times4$ layer is highly sensitive to ambient gases, especially O_2 [19-21]. Recently, elimination of the graphene-substrate interaction has been achieved by exfoliating epitaxial graphene from the SiC(0001) surface by using hydrogen or fluorine intercalation into the buffer layer [22,23]. Motivated by such a successful strategy, the interaction between the top $\sqrt{3}\times\sqrt{3}$ silicene layer and the metal substrate is expected to be effectively reduced by an appropriate intercalation into the buffer $\sqrt{13}\times\sqrt{13}/4\times4$ silicene layer, which, in turn, may allow the top layer to recover the intrinsic properties of silicene.

In this chapter, oxidization of bilayer silicene was conducted on Ag(111), and it was found that the oxygen molecules intercalate into the $\sqrt{13}\times\sqrt{13}/4\times4$ buffer layer of silicene. As a result, the top layer of silicene exhibits the signature of the 1×1 lattice structure of "free-standing" silicene and shows a robust Dirac fermion characteristic with less electron doping, which were revealed by STM and XPS measurements. Combined with first-principles calculations, we demonstrate that the top layer of silicene can act as quasi-free-standing silicene with weakened interaction with the substrate. Our study establishes a novel and simple way to obtain quasi-free-standing silicene on the substrate. Additionally, the silicon oxide buffer layer may be used as the dielectric layer for possible construction of field effect transistors (FETs) directly on the metal substrate.

7.2 Materials and methods

7.2.1 Sample preparation

The silicene layers were fabricated by the deposition of silicon atoms on the Ag(111) substrate from a heated silicon wafer in a preparation chamber attached to an *in-situ* STM/Raman system under UHV ($< 1\times10^{-10}$ torr). A clean Ag(111) substrate was prepared by argon ion sputtering and subsequently annealed at 550 ˚C for several cycles. The deposition flux of Si was 0.08 monolayers per minute (ML/min). The temperature of the Ag(111) substrate was kept at 220 ˚C during deposition. An *in-situ* oxygen intercalation process was carried out by introducing oxygen molecules into the preparation chamber at a sample temperature of 200 ˚C. The Langmuir (L) was used as the unit of exposure to O_2, *i.e.*, 1 L is an exposure of 10^{-6} torr O_2 in one second.

7.2.2 Characterization of structural and electronic properties

The STM and Raman spectroscopy measurements were carried out using a low-temperature UHV STM/scanning near-field optical microscopy system (LT-UHV-STM-SNOM) (SNOM1400, Unisoku Co.) in UHV (< 8×10^{-11} torr) at 77 K. The Raman spectra were acquired using laser excitation of 532 nm (2.33 eV) delivered through a single-mode optical fibre at 77 K in UHV. The spot size of the incident laser in *in-situ* Raman spectroscopy was about 3 μm in diameter. *In-situ* ARPES and XPS characterizations were performed at the photoelectron spectroscopy station in the Beijing Synchrotron Radiation Facility (BSRF) using a SCIENTA R4000 analyzer. A monochromatized He-I light source (21.2 eV) was used for the band dispersion measurements. The total energy resolution was set to 15 meV, and the angular resolution was set to ~ 0.3˚, which gives a momentum resolution of ~0.01 π/a. The XPS experiments were performed at Beamline 4B9B, and variable photon energies were referenced to a fresh Au polycrystalline film. The spot size of the incident radiation in XPS is about 1 mm in diameter.

7.2.3 DFT calculations

Ab initio calculations were performed using DFT and a plane wave basis with cut-off energy of 400 eV, as implemented in VASP [24]. The electron-ion interactions were represented by PAW potentials [25]. The PBE functional was adopted to describe the exchange-correlation interaction [26]. To properly take into account the long-range van der Waals interactions in layered structures, the DFT-D3 scheme [27] was used. The Ag(111) surface was modelled by a three-layer slab model with a vacuum space of more than 12 Å, which was cleaved from a face-centred cubic (fcc) solid silver bulk with an experimental lattice constant of 2.89 Å. Within the constrained supercell, the slab model was further relaxed, with the bottom layer fixed to mimic a semi-infinite solid. The monolayer 4×4 silicene/Ag(111) superstructure was composed of 3×3 silicene cells and 4×4 Ag(111) cells. Bilayer silicene was further

constructed by putting a √3×√3 silicene layer on top of the 4×4 silicene/Ag(111). To simulate oxygen adsorption on pristine bilayer silicene, a 2×2 supercell of the √3×√3 silicene/4×4 silicene/Ag(111) structure with lattice constant of 23.12 Å and a total of 192 silver atoms plus 150 silicon atoms was adopted. Similarly, a 2×2 supercell of monolayer 4×4 silicene on Ag(111) was also considered. To model oxygen intercalation, a slab of 4×4 Ag(111) supercell with 48 silver atoms, a buffer layer of SiO_x with 22 silicon atoms and 42 oxygen atoms, and a top 1×1 silicene layer with 18 silicon atoms were combined to construct the silicene/SiO_x/Ag(111) hybrid structure, which was relaxed by an AIMD simulation at 550 K for 10 ps, followed by geometry optimization. Note that the SiO_x buffer layer is thicker than the pristine 4×4 silicene layer, based on our experimental observation that the height of the oxygen-intercalated silicene area is higher than that of the pristine silicene area.

7.3 Results and discussion

7.3.1 Observation of 1×1 lattice induced by oxygen intercalation

Figure 7.1 (a) shows an STM image of pristine √3×√3 silicene supported by the √13×√13/4×4 buffer layer on Ag(111). In the pristine sample, the exposed buffer silicene layer shows three distinct structures, *i.e.*, 4×4, √13×√13R13.9˚(-I), and √13×√13R13.9˚(-II) [28]. The top layer of silicene exhibits √3×√3 lattice with a lattice constant a = 0.64 nm, which is approximately √3 times that of the 1×1 silicene structure (a = 0.38 nm) [29]. Figure 7.1 (b) is a STM image of a single piece of silicene island with a √3×√3 top layer, collected after the sample was exposed to oxygen with a dose of 600 Langmuir (L). The bright area of the island is higher than the dark area by about 0.9 Å, as shown in Fig. 7.1 (c). The high-resolution STM image [Fig. 7.1 (d)] reveals that the structural features of the √3×√3

reconstruction in the higher area are weaker than in the dark area [Fig. 7.1 (e)]. It is found that the higher area forms from the edge of a √3×√3 silicene flake. More importantly, the higher area exhibits the signature of a 1×1 lattice of "free-standing" silicene. To the best of our knowledge, this is the first experimental observation of a 1×1 lattice in silicene. We further increased the oxygen dose up to 1200 L, and the corresponding STM image [Fig. 7.1 (f)] shows that the exposed √13×√13/4×4 layer changes to an amorphous form, while the √3×√3 silicene clearly retains intact. The higher degree of buckling of Si atoms in the √13×√13/4×4 silicene layer [19] enables surface dangling bonds to easily react with oxygen. Consequently, crumpled amorphous silicon oxide (SiO_x) is formed, leading to exposure of the bare Ag(111) surface, which was also observed in our previous study [19]. Considering the √3×√3 top layer sitting on the √13×√13/4×4 layer, we conjecture that the oxygen atoms are intercalated between the two silicene layers and react with the underlying √13×√13/4×4 layer. That is why the surface of the √3×√3 top layer remains intact and the oxidized area of the √3×√3 layer is higher than the unoxidized area. The increased height reflects the fact that the oxidizing process of the √13×√13/4×4 layer follows the conventional oxidation of silicon, in which the volume of SiO_x is increased upon oxidation.

It is necessary to describe the structure of silicene in detail to make our statements clear. Due to the buckled structure of silicene, silicon atoms are displaced alternatively in a direction perpendicular to the plane. In this case, the silicon atoms can be classified as upper buckled atoms and lower buckled atoms. Only the upper buckled atoms could be observed in the STM measurements due to the large degree of buckling. Figure 7.2 (a) and (b) present a schematic model illustrating the honeycomb structure of the √3×√3 superstructure. It can be found that all the silicon atoms in √3×√3 silicene are arranged in a form of honeycomb-like structure, *i.e.*, the 1×1 silicene honeycomb structure, with the arrangement of upper buckled silicon atoms reflecting the √3×√3 superstructure, indicating that the √3×√3 superstructure is derived

from 1×1 silicene. We repeated our experiments for oxygen-intercalated silicene, where the intercalated region exhibits a clear signature of the 1×1 lattice of "free-standing" silicene (Fig. 7.1 (d)), and the non-intercalated region retains the √3×√3 superstructure (Fig. 7.1 (e)). Thus, the observation of a 1×1 lattice of "free-standing" silicene in the oxidized area of the √3×√3 layer suggests that the interactions between the top layer of silicene and the underlying silicene/silicon oxide or Ag(111) substrate are weakened by oxidization.

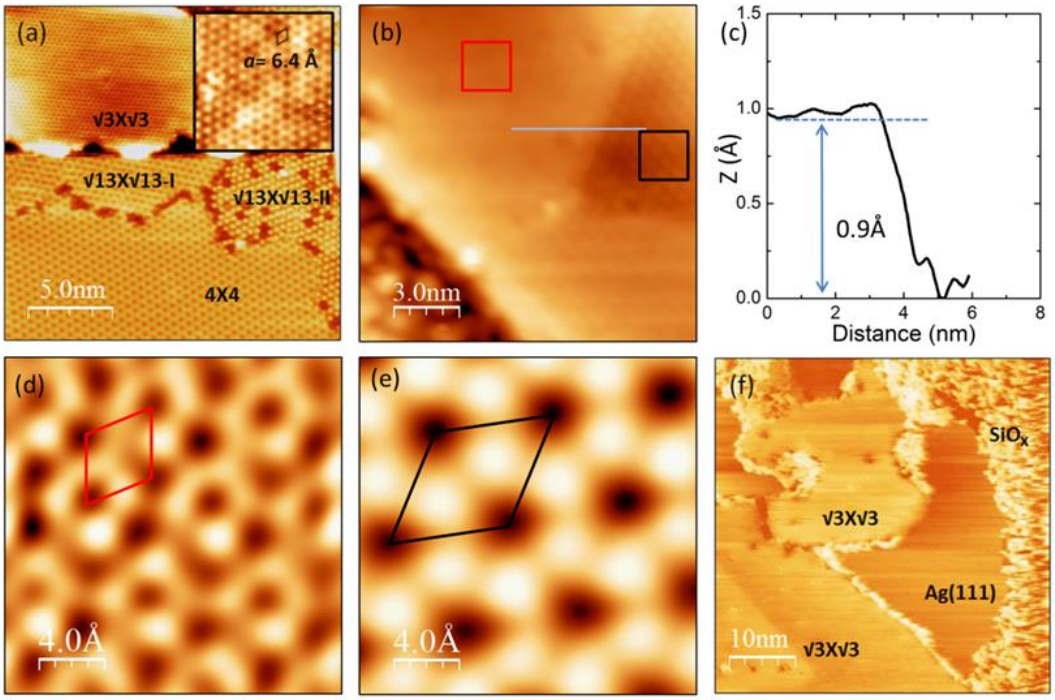

Fig. 7.1 Topographic images of pristine and oxygen intercalated epitaxial silicene grown on Ag(111). (a) STM topographic image of pristine √3×√3 silicene that was formed on a √13×√13/4×4 buffer layer. Inset is a high-resolution image of √3×√3 silicene, which demonstrates a honeycomb structure with a lattice constant of 0.64 nm (V_{bias} = –0.8 V, I = 0.2 nA); (b) oxygen intercalated √3×√3 silicene after an oxygen dose of 600 L (V_{bias} = 0.6 V, I = 2 nA); (c) line profile for the straight line in panel (b); (d) and (e) enlarged STM images of intercalated region (red frame in panel (b)) and non-intercalated √3×√3 silicene (black frame in panel (b)), respectively. The red rhombus and black rhombus stand for the unit cell of 1×1 silicene and √3×√3 silicene, respectively (V_{bias} = 3 mV, I = 4 nA); (f) oxygen intercalated silicene layers after an oxygen dose of 1200 L, in which the buffer layer is fully oxidized, while the √3×√3 silicene shows

robust structural stability against oxygen intercalation (V_{bias} = –1.2 V, I = 0.1 nA).

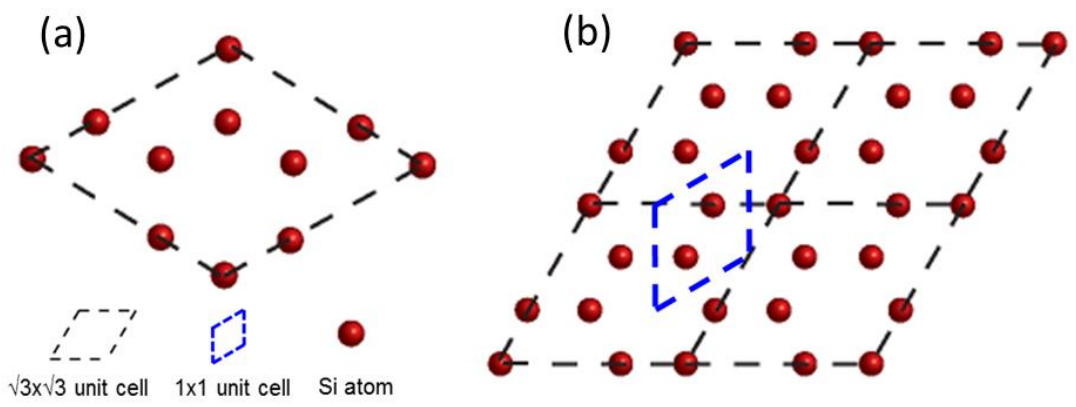

Fig. 7.2 (a) and (b) STM images of intercalated region and non-intercalated region of √3×√3 silicene, respectively. The blue rhombus and black rhombus stand for the unit cells of 1×1 silicene and √3×√3 silicene, respectively (V_{bias} = 3 mV, I = 4 nA).

7.3.2 XPS of oxygen-intercalated √3×√3 silicene

To corroborate the oxidization model sketched in Fig. 7.2, a detailed analysis of the chemical bonds was conducted by XPS and Raman spectroscopy. Si 2*p* and Ag 3*d* core level spectra were collected for the pristine and oxygen-treated silicene samples, as shown in Fig. 7.3. Different components contributing to the spectra were decomposed by a curve-fitting procedure [10]. Figure 7.3 (a) shows Ag 3*d* core level spectra collected from the pristine silicene sample and intercalated samples treated with various oxygen doses. The Ag $3d_{3/2}$ and $3d_{5/2}$ peaks at 374.1 eV and 368.2 eV, respectively, originate from the Ag(111) substrate. A downward energy shift (~ 0.7 eV) for the Ag 3*d* orbital is observed in the silicene/Ag(111) sample, where chemical bonds form between the Ag(111) substrate and the silicene buffer layer, indicating that the chemical activity of the silicene buffer layer is higher than that for the pure Ag-Ag bonds in the Ag(111) substrate. After oxygen intercalation, shifts of the Ag peaks towards higher energy are observed. This makes it manifest that oxygen intercalation

breaks Ag-Si bonds, and as a result, the XPS peaks corresponding to the Ag 3*d* core level are restored to the Ag-Ag state. Moreover, no Ag-O chemical structure is present in the XPS spectrum, which implies that oxygen molecules do not react with Ag(111). Figure 7.3 (b) shows Si 2*p* core level spectra for the samples before and after oxygen treatment. The fitting of the Si 2*p* lines clearly shows that there are two groups of bonding components, *i.e.*, Group I (labelled as Si_1 and Si_2) and Group II (labelled as Si_3 and Si_4), respectively. The energy gap of the two peaks in each group is a constant value, indicating that the fitted peaks in each group are respectively related to the Si $2p_{3/2}$ and $2p_{1/2}$ peaks. We assign the Group I and Group II peaks to Si-Si bonds in the top $\sqrt{3}\times\sqrt{3}$ layer and in the $\sqrt{13}\times\sqrt{13}/4\times4$ buffer layer, respectively, because the positions of the Si_1 and Si_2 peaks remain the same before and after oxygen intercalation, while the Si_3 and Si_4 peaks show obvious shifts towards higher energy after oxygen intercalation. This is consistent with the fact that $\sqrt{3}\times\sqrt{3}$ silicene layers are resistant to oxidization, while the $\sqrt{13}\times\sqrt{13}/4\times4$ buffer layer possesses high reactivity to oxygen molecules. Note that Si-O peaks are clearly present after oxygen treatment. The binding energy value (101.6 eV) is lower than the peak position of SiO_2-like binding energy (102.3 eV), indicating that the valence states of the Si-O bonds are lower than Si^{4+}. Therefore, the silicene is not fully oxidized to SiO_2, in agreement with the STM and ARPES findings. The intensity of the peaks related to the $\sqrt{13}\times\sqrt{13}/4\times4$ silicene layers is significantly reduced after the emergence of the Si-O peak. The variation in the peak intensity reveals that oxygen molecules prefer to react with Si atoms in the buffer layer, as demonstrated by the oxidized $\sqrt{13}\times\sqrt{13}/4\times4$ buffer layer with much less top $\sqrt{3}\times\sqrt{3}$ silicene (< 0.1 ML) in the bottom panel of Fig. 7.3 (b).

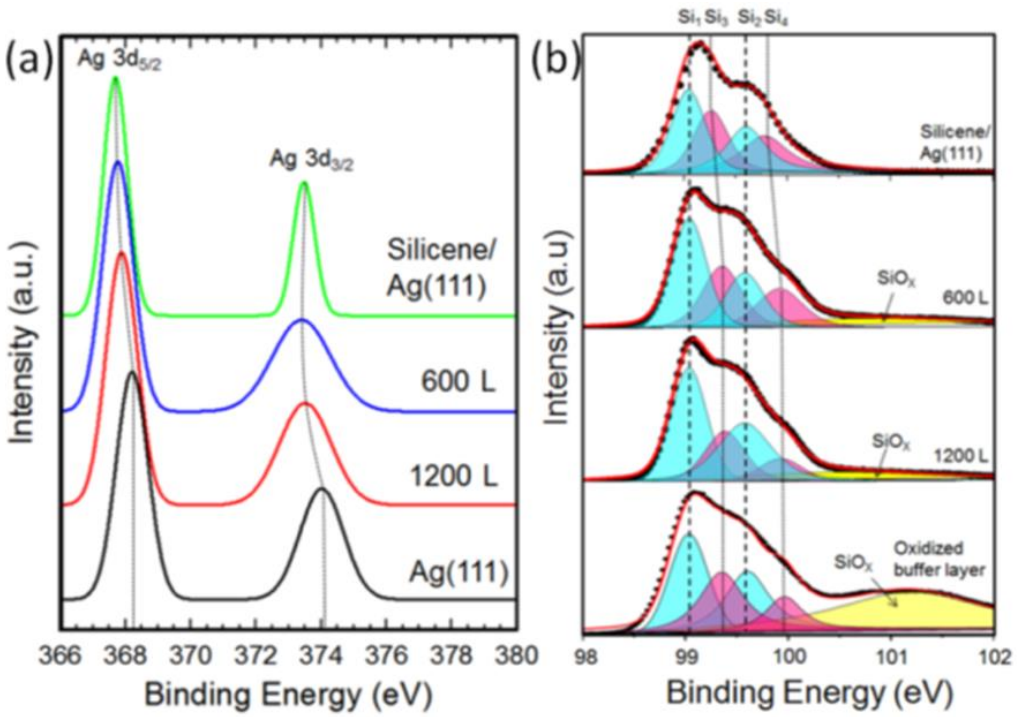

Fig. 7.3 Representative Ag 3*d* and Si 2*p* core level XPS spectra of pristine and oxygen intercalated silicene layers grown on Ag(111). (a) Ag 3*d* XPS spectra for Ag(111), pristine silicene, and intercalated samples with different oxygen doses. (b) Si 2*p* core level XPS spectra of pristine and oxygen intercalated silicene layers grown on Ag(111). The Si_1 and Si_2 peaks are attributed to Si-Si bonds in $\sqrt{3}\times\sqrt{3}$ silicene, while Si_3 and Si_4 are attributed to the $\sqrt{13}\times\sqrt{13}/4\times4$ silicene buffer layer. The XPS spectra indicate that the buffer layer is oxidized and detached from Ag(111) in the oxygen intercalation process, while $\sqrt{3}\times\sqrt{3}$ silicene retains its electronic structure after oxygen intercalation.

7.3.3 Raman spectra of oxygen-intercalated $\sqrt{3}\times\sqrt{3}$ silicene

Raman spectroscopy is particularly sensitive to changes in the band gap, the *in-plane* bonds, and the strain effect associated with structural change, and thus plays an important role in the structural characterization of 2D materials [30-32]. The phonon modes in the pristine and oxygen-intercalated samples were characterized by *in-situ* Raman spectroscopy, as shown in Fig. 7.4. Since Ag(111) substrate is a metal, which does not contribute a Raman signal, the Raman spectra are only attributed to the epitaxial silicene layers, although the silicene layers

are thinner than the penetration depth of Raman incident light. The Raman peak at 526.3±3 cm^{-1} is due to the doubly degenerate E_{2g} mode [31,32] at the Brillouin zone (BZ) center Γ point for all silicene structures. The E_{2g} peak of silicene is sensitive to temperature variation regardless of structure.

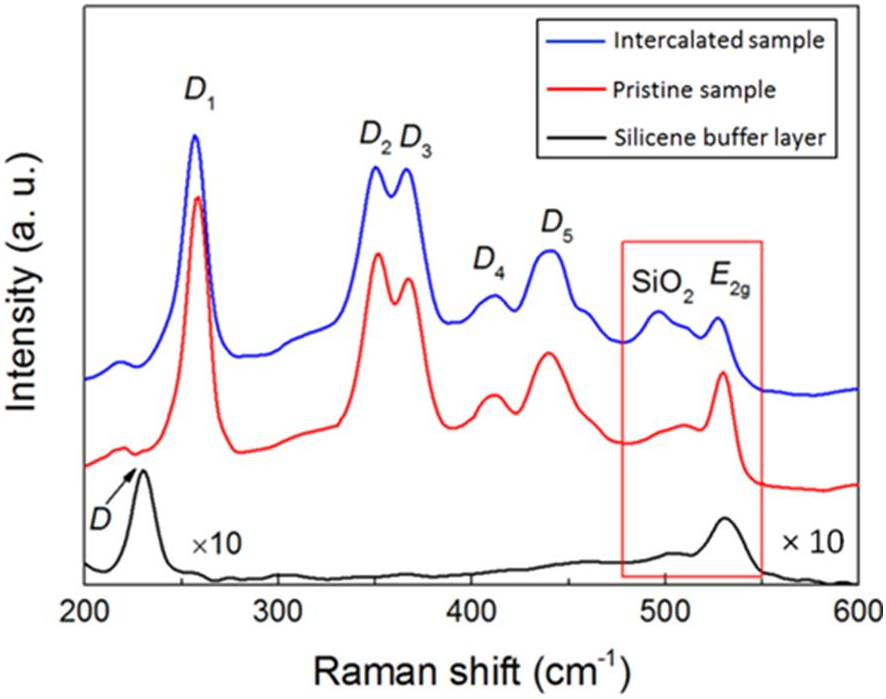

Fig. 7.4 Raman spectra of √13×√13/4×4 silicene buffer layer (black), √3×√3 silicene with 0.3 ML coverage on √13×√13/4×4 buffer layer (pristine sample, red), and oxygen intercalated sample (blue). The oxidized buffer layer features a broad Raman peak at 494 cm^{-1} in the spectrum of the oxygen intercalated sample.

The *in-situ* temperature-dependent Raman spectra of monolayer 4×4/√13×√13 buffer layer and √3×√3 silicene samples from liquid nitrogen temperature to 275 K are shown in Fig. 7.5. The E_{2g} mode in both samples shows an obvious blue shift when the temperature is decreased. In contrast to the 4×4/√13×√13 structure, the √3×√3 silicene exhibits a more sensitive E_{2g} mode under temperature variation from 80 K to 275 K. The D_1-D_5 peaks are attributed to electron intervalley or intravalley scattering at the zigzag and armchair edges in the √3×√3

silicene, and the *D* peak is induced by boundary defects in the 4×4/√13×√13 silicene [32]. After oxygen treatment, the *D* peak vanishes, and an additional Raman peak at 494 cm^{-1} emerges, which indicates the formation of amorphous silicon oxide [33]. In contrast, all the Raman peaks assigned to the √3×√3 silicene are almost invariable after oxygen treatment. By scrutinizing the fingerprint E_{2g} peak, it is found that the peak position is blue-shifted by 4 cm^{-1} in the oxygen-intercalated sample. The shift of the Raman signal suggests that the tensile strain in epitaxial √3×√3 silicene is "released" towards "unstrained" free-standing 1×1 silicene by oxygen intercalation [31,32,34].

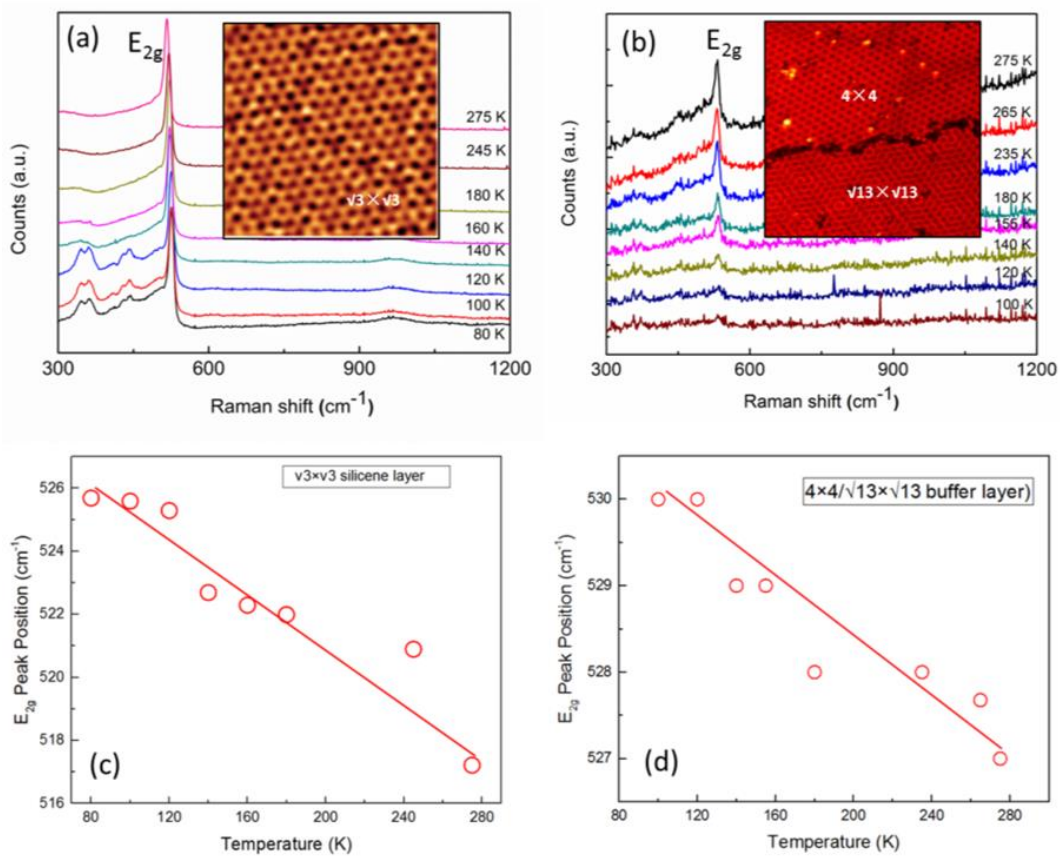

Fig. 7.5 *In-situ* temperature-dependent Raman spectra of (a) 0.5 ML √3×√3 silicene and (b) monolayer 4×4/√13×√13-silicene buffer layer samples from liquid nitrogen temperature to 275 K. The insets are corresponding STM images of the samples. (c) and (d) are plots of the E_{2g} peak position (cm^{-1}) *vs* temperature (K) for the √3×√3 silicene and buffer layer, respectively. It is found that the E_{2g} mode in both samples shows an obvious blue shift when the temperature is decreased.

The *ex-situ* Raman spectra were used to examine the stability of the oxygen-intercalated sample exposed to ambient air. The detailed results are displayed in Fig. 7.6. We used *ex-situ* Raman spectroscopy to examine the stability of the intercalated monolayer √3×√3 silicene. The Raman spectra were obtained from samples exposed to ambient air for periods ranging from 0.5 h to 150 h. The signature Raman peak provided by bond stretching of all sp^2 silicon atoms is assigned to the E_{2g} mode (about 526 cm^{-1}). The shoulder peak at lower wavenumber (about 460-480 cm^{-1}) is attributed to the oxidized buffer layer, which has been well studied in our previous work[2]. The intensity of the E_{2g} peak decreases with increasing exposure time, combined with an intensified signal of the SiO_x peak. Importantly, the E_{2g} peak survives in the Raman spectra until the sample has been exposed to ambient air for more than 150 h. Therefore, the oxygen-intercalated √3×√3 silicene demonstrates stability in the ambient environment for up to 6 days, which is much better than what was expected [18].

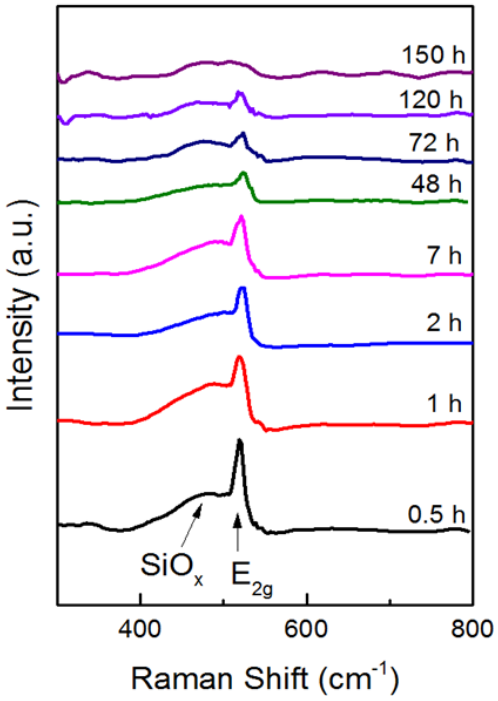

Fig. 7.6 *Ex-situ* Raman spectra of √3×√3 silicene samples that were exposed to ambient air from 0.5 hour to 150 hours. The E_{2g} peak decreased in intensity as the sample was exposed to ambient air. The SiO_x peak is attributed to the oxidized buffer layer.

7.3.4 DFT calculations on the oxidation of √3×√3 silicene

The STM, XPS, and Raman spectroscopy results suggest that the oxygen atoms are intercalated between the silicene layers and weaken the interaction between the top layer and the Ag(111) surface. This picture is confirmed by our DFT calculations on the oxidation of the silicene layers on the Ag(111) surface. As shown in Fig. 7.7 (a), when an O_2 molecule is adsorbed on monolayer 4×4 silicene/Ag(111), it will spontaneously decompose into two O atoms, with one O atom sitting on the top of a silicon atom and the other located at the neighboring bridge site. The chemical dissociation of a gaseous O_2 molecule on monolayer 4×4 silicene is an exothermic process with adsorption energy of 5.474 eV. In sharp contrast, when an O_2 molecule is adsorbed on the √3×√3 silicene layer on top of 4×4 silicene/Ag(111), it would not decompose after relaxation, as shown in Fig. 7.7 (b). The corresponding adsorption energy of only 2.84 eV is much smaller than that for the dissociative adsorption of O_2 on the monolayer 4×4 silicene (5.474 eV), indicating the higher resistance of √3×√3 silicene to oxidation compared with monolayer 4×4 silicene, as observed in our experimental results.

It is necessary to determine the status of the buffer layer beneath √3×√3 silicene before simulating the interaction strength after oxygen-intercalation. We directly placed an O_2 molecule between the top √3×√3 layer and the bottom 4×4 layer in bilayer silicene [Fig. 7.7 (c)]. Upon relaxation, O_2 would spontaneously dissociate into two oxygen atoms, and the adsorption energy is as large as 6.36 eV, comparable to the adsorption energy of the uncovered buffer layer. The even larger adsorption energy for the covered buffer layer suggests the preference for oxidization of the covered √13×√13/4×4 silicene layer underneath the top √3×√3 silicene layer, as shown in the schematic diagrams in Fig. 7.8 (b). The dynamic procedure of oxygen intercalation is further experimentally revealed in Fig. 7.9, where the

intercalation depth, which is the distance from the silicene edges to the centers of the top √3×√3 silicene islands, increases with increasing oxygen dose.

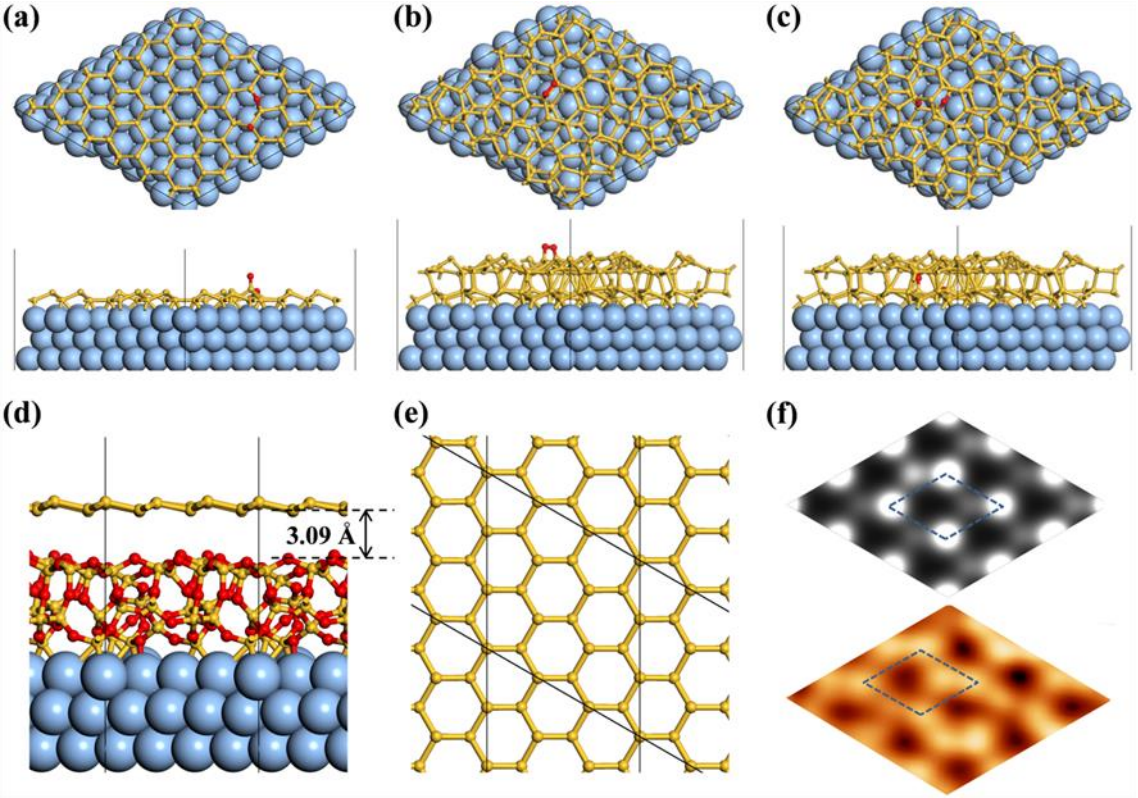

Fig. 7.7 Atomic structures of an O_2 molecule adsorbed on (a) 4×4 silicene buffer layer, (b) top layer silicene, (c) 4×4 buffer layer underneath √3×√3 silicene. Atomic structure of silicene/SiO_x/Ag(111) from AIMD simulation: (d) side view, (e) top view of the top layer silicene only. (f) Simulated (top) and experimental (bottom) high-resolution STM images of silicene/SiO_x/Ag(111), showing the 1×1 silicene honeycomb lattice.

To model the oxidized bilayer silicene on Ag(111) substrate, we constructed a sandwich structure of √3×√3 silicene/SiO_x/Ag(111) [x = 1.909], as depicted in Fig. 7.7 (d). After relaxation, the top silicene sheet retains its hexagonal honeycomb lattice [Fig. 7.7 (e)] and interacts weakly with the SiO_x buffer layer at an average separation of 3.09 Å. Compared to the interfacial binding energy (123 meV/Å^2) between the top layer and the bottom layer of the pristine bilayer silicene, the binding energy (12 meV/Å^2) between the silicene top layer and

the SiO_x buffer layer is significantly reduced by one order of magnitude after oxygen intercalation. As a consequence of the weakened silicene-substrate interaction, the simulated STM image [Fig. 7.7 (f)], based on the structural model of silicene/SiO_x/Ag(111) in Fig. 7.7 (d), coincides with the experimental one, showing the clear pattern of the 1×1 structure of the honeycomb lattice of silicene. Therefore, DFT calculations convincingly support the existence of a quasi-free-standing silicene top layer after oxygen intercalation, as conjectured from our experiments.

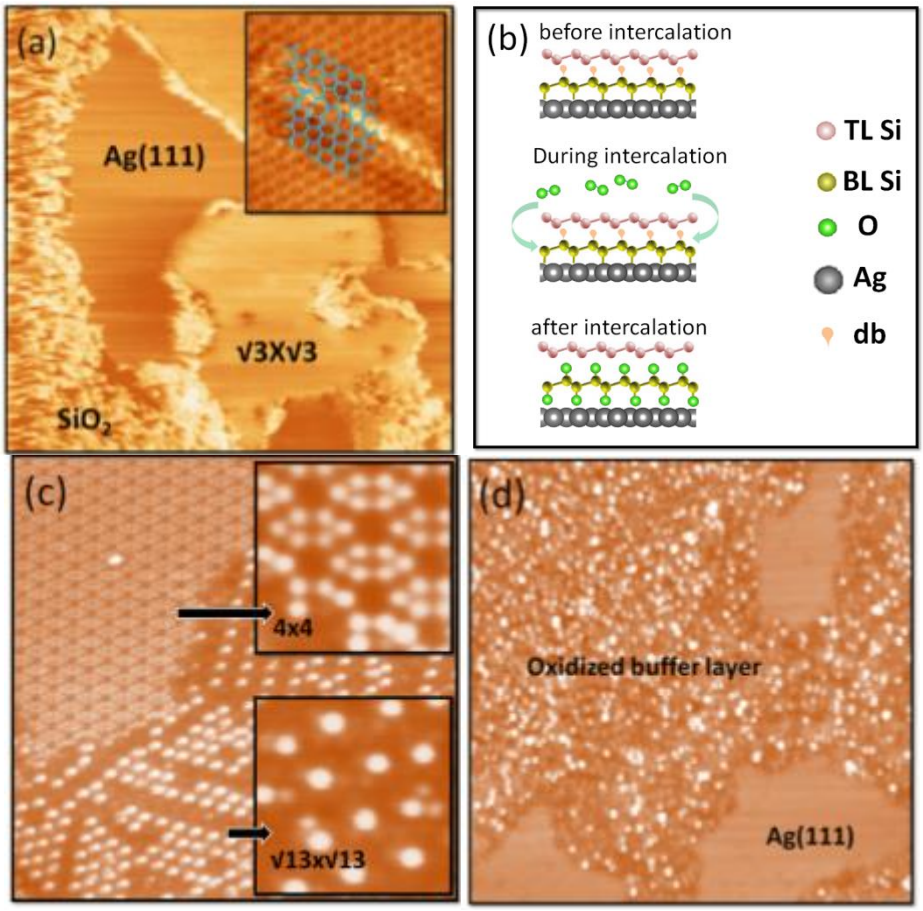

Fig. 7.8 (a) STM topographic image of oxygen-intercalated silicene layers grown on Ag(111). The inset is a corrugated area on top of √3×√3 silicene due to intercalation. (b) Schematic diagrams of oxygen intercalation in silicene layers, in which the oxygen gas diffuses into the underlying silicene buffer layer, breaks the bonds at the buffer layer/Ag(111) interface, and saturates the dangling bonds (db) in the √13×√13/4×4 buffer layer. TL Si refers to Si in the top layer √3×√3 silicene, and BL Si refers to Si in the √13×√13/4×4 silicene buffer layer. (c) STM topographic image of two major phases that are mixed in the

silicene buffer layer, √13×√13 and 4×4, in different domains. The insets show the detailed structures of the two phases in the buffer layer. (d) STM topographic image of oxidized silicene buffer layer after an oxygen dose of 600 L. It verifies that the buffer layer is unstable in an oxygen environment.

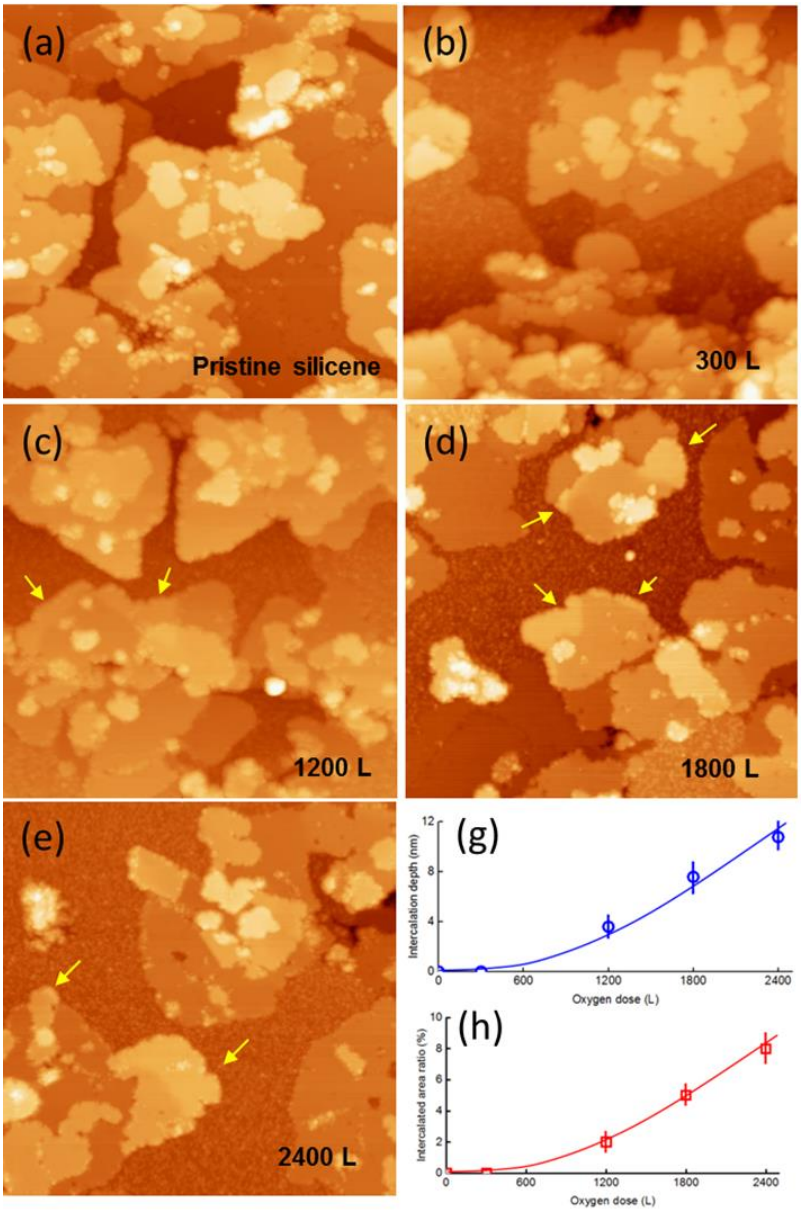

Fig. 7.9 STM images of (a) √3×√3 silicene grown on Ag(111) surface and of the samples after oxygen intercalation under different oxygen doses of (b) 300 L, (c) 1200 L, (d) 1800 L, and (e) 2400 L (100 nm×100 nm, V = 1.2 V, I = 50 pA). (g) Intercalation depth (nm) as a function of oxygen dose in intercalated silicene samples. (h) Intercalated area ratio (%) as a function of oxygen dose in intercalated silicene samples. Yellow arrows identify intercalated regions.

7.3.5 ARPES spectra on pristine silicene and oxygen intercalated silicone

Apart from the structural aspect, oxygen intercalation has a remarkable impact on the electronic structure of silicene layers. Figure 7.10 shows the electronic band structures measured by ARPES on pristine silicene and oxygen intercalated silicene grown on Ag(111). As a reference, the electronic band structure of the clean Ag(111) surface is also shown in Fig. 7.10 (a), where the SSS at the BZ center (Γ point) and the bulk Ag *sp*-band are indicated. When $\sqrt{3}\times\sqrt{3}$ silicene was grown, we observed two faint linear dispersed bands crossing at the Γ point, as shown in Fig. 7.10 (b). Constant-energy cuts of the spectral function at different binding energies verify that both bands originate from a Dirac cone structure, as shown in Fig. 7.10 (e), which can be assigned to the linear π and π^* states of $\sqrt{3}\times\sqrt{3}$ silicene [17,35]. The Dirac point (DP) is located at about 0.33 eV below the Fermi level (E_F) due to electron doping from the Ag(111) substrate [36].

Figure 7.10 (c) and (d) present the electronic band structures after oxygen intercalation under different doses of oxygen (600 L and 1200 L) at 200 $^{\circ}$C, as measured by ARPES with higher energy and momentum resolutions. One can clearly see that two single Dirac cones meet at the DP, which is located at about −0.28 eV and −0.26 eV for the samples exposed to oxygen doses of 600 L and 1200 L, respectively. The characteristic "Δ"-shaped bands at a deep energy level (below -0.7 eV), which were attributed to the hybridization between interface Si p_z orbitals and Ag *d* orbitals in the pristine sample [9,10], are smeared or vanish after oxygen intercalation. The typical bulk *sp*-band of Ag across the Fermi level at k = 1.15 Å^{-1} appeared in the ARPES results after oxygen intercalation, as shwn in Fig. 7.11. It indicates that this band remains stable upon Si deposition as well as oxygen intercalation. A new state corresponding to silicon oxide appears in the oxygen intercalated silicene at a deep energy level (below -0.6 eV), centred at k = -0.2 Å along the Γ-K direction. This state is more

obvious in the ARPES feature for the oxygen-intercalated sample after an oxygen dose of 1200 L, as shown in Fig. 7.10 (d).

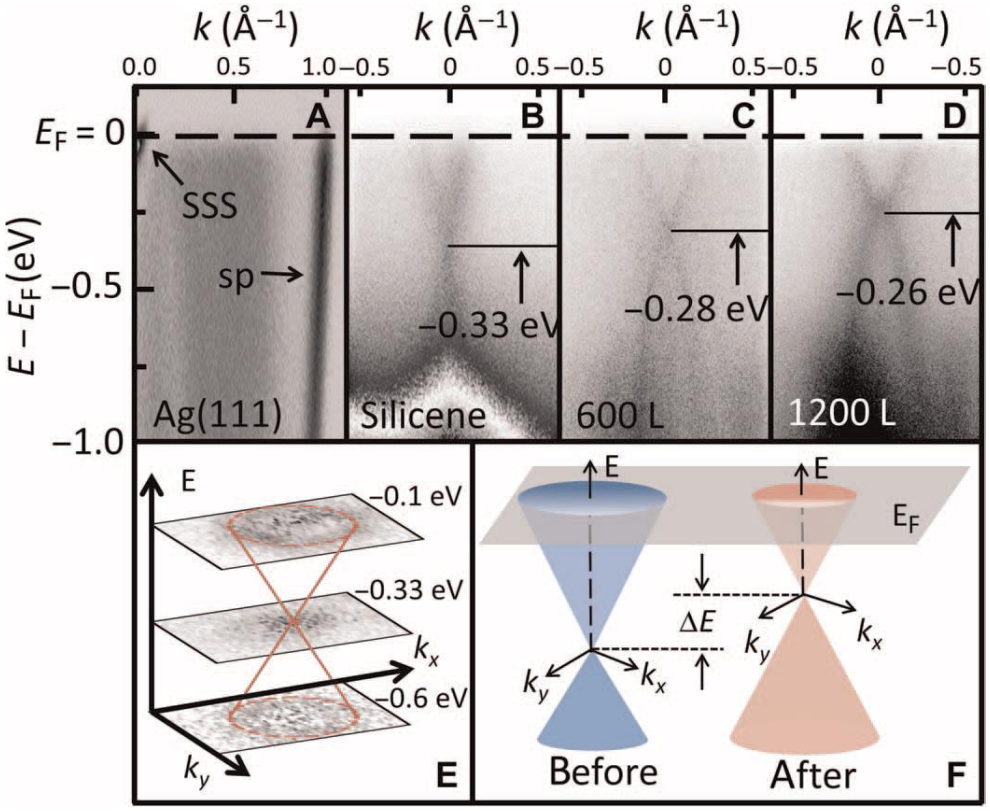

Fig. 7.10 Energy vs. *k* dispersion measured by ARPES for (a) clean Ag(111) surface, (b) as-grown √3×√3 silicene formed on buffer layer, (c) oxygen intercalated silicene with oxygen dose of 600 L, and (d) intercalated silicene with oxygen dose of 1200 L, respectively. The Shockley surface state (SSS) and the *sp* band in (a) are attributed to the Ag(111) substrate. The Dirac point in (b)-(d) is lifted up with increased oxygen dose from 0 L to 1200 L, indicating less electron doping from the Ag(111) substrate due to oxygen intercalation. (e) ARPES energy cuts reveal a Dirac cone structure in pristine silicene. (f) Schematic view of shifting of Dirac cone due to oxygen intercalation in ARPES measurement.

The corresponding positions of the ARPES cuts are illustrated in Fig. 7.11 (d). The positions of the Dirac cone, the Ag *sp* band, and the Brillouin zones of √3×√3 silicene and Ag(111) are illustrated as well. We did not observe the SSS of the Ag(111) substrate in the oxygen intercalated sample, as shown in Fig. 7.11 (a). This is different from the ARPES cut from the

oxidized 4×4/√13×√13-silicene buffer layer. The SSS can be easily modulated or destroyed by surface adsorbates. In the oxidized 4×4/√13×√13-silicene buffer layer sample, the remaining Ag(111) surface is large enough to support the existence of the SSS band, although its intensity is much lower than that of the SSS on a clean Ag(111) surface. In contrast, only a very limited amount of Ag(111) surface (less than one third of the total area) was exposed in the oxygen intercalated √3×√3 silicene, because √3×√3 silicene is not crumpled at all by oxygen intercalation. In other words, most of the Ag(111) surface was covered by quasi-free-standing silicene after oxygen intercalation. Therefore, the SSS of the Ag(111) surface in oxygen intercalated samples is most likely destroyed by √3×√3 silicene. Although we did not observe the SSS state in Ag(111), a clear Ag *sp*-state can be seen in ARPES Cut 2 and Cut 3 in Fig. 7.11 (b) and (c), respectively. Note that the *sp* band is a bulk state of the Ag(111) substrate. Its existence in ARPES is not determined by the cleanliness of the surface.

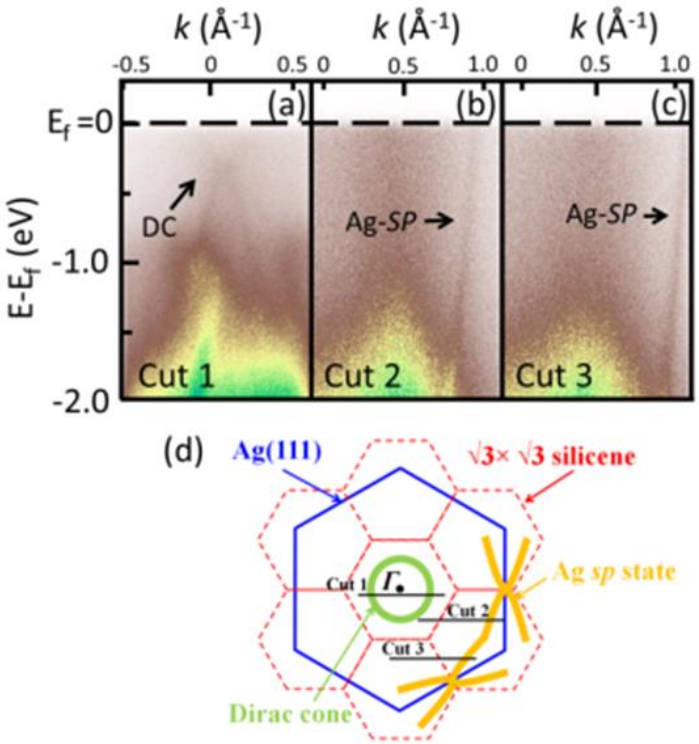

Fig. 7.11 Energy vs. *k* dispersion measured by ARPES for oxygen intercalated √3×√3 silicene under oxygen dose of 600 L. Three ARPES results along three cuts shown in (d) reveal (a) Dirac cone (DC) of

√3×√3 silicene, (b) and (c) bulk *sp*-band of Ag(111) substrate. (d) Schematic diagram of BZ for √3×√3 silicene grown on Ag(111): blue and red honeycomb structures correspond to Ag(111) and √3×√3 silicene, respectively. Positions of three ARPES cuts, Dirac cone, and Ag *sp*-state are respectively indicated.

The ARPES results reveal that the electronic structures of epitaxial silicene are modulated by chemical adsorption. In the initial intercalation stage, the chemical interaction between the buffer-layer silicene and the Ag substrate is broken by the oxygen atoms. The Si-Ag hybridized state in the silicene/Ag(111) system is replaced by electronic states attributable to the Si-O bonds. As the oxygen dose increases, the oxidized 4×4/√13×√13 buffer layer contributes more states at the deep level (below -0.6 eV). Meanwhile, the DP is pushed up towards the Fermi level, because the oxidized buffer layer acts as a dielectric barrier and lowers the electron doping in the top √3×√3 silicene layer, as shown in Fig. 7.10 (f). Interestingly, the thickness of the oxidized buffer layer is increased when the oxygen dose is increased. In other words, the dielectric barrier will become thicker with an oxygen dose. Consequently, the doping level should be lower in the intercalated silicene with a higher oxygen dose. This agrees well with our ARPES results, in which 1200 L-oxygen-intercalated silicene has the Dirac point at 0.26 eV below the Fermi level while 600 L-oxygen intercalated silicene has its Dirac point at 0.28 eV below the Fermi level.

The weakened doping effect from the substrate on the silicene's electronic structure is also observed in the STS results, as shown in Fig. 7.12. For each intercalation stage, we carefully investigated the morphology and electronic structures of the intercalated silicene. It was found that the buffer layer is easily oxidized, as described in above. Nevertheless, all the √3×√3 silicene layers show a high resistance to oxidation, even under an oxygen dose of 2400 L, whereas no adsorbate could be identified on the √3×√3 silicene surface. Obvious intercalation occurred when the oxygen dose was increased above 600 L. The intercalated areas can be easily identified in STM images in terms of apparent height, and these are

indicated by the yellow arrows in Fig. 7.9 (c)-(e). For all the samples, it is clearly shown that the oxygen intercalation starts at the edge of the silicene. It is proposed that oxygen molecules then diffuse from the edge towards the center of the silicene bilayer region, because the intercalation depth (which is the distance from the silicene edge to the end of the intercalation area) is increased with increasing oxygen dose. The intercalation depth as a function of oxygen dose has been plotted in Fig. 7.9 (g). The intercalated area is correspondingly increased when the oxygen dose is increased, as shown in Fig. 7.9 (h). It should be noted that the intercalation only occurs at the interface between the buffer layer and the first $\sqrt{3}\times\sqrt{3}$ silicene layer, in agreement with our model for intercalation, which is caused by the oxygen diffusion from the uncovered buffer layer to the region beneath the $\sqrt{3}\times\sqrt{3}$ silicene. STM characterization of the oxygen-intercalated area on the silicene shows the dynamic process of oxygen intercalation.

We then characterized the electronic structures in oxygen intercalated silicene, in particular with respect to the doping level, by using STS techniques. We collected the spectra along a line crossing the pristine and intercalated areas on the sample, as indicated in Fig. 7.12 (a). It was found that the signature peak at about -0.9 eV in the pristine area shows an obvious shift to -0.75 eV in the intercalated area [Fig. 7.12 (b)]. The peak shift demonstrates that the electron doping is depressed due to oxygen intercalation, which agrees well with our ARPES results in the main text. In addition, the peak intensity is also decreased for the peak obtained in the intercalated area. In a previous study, this peak was attributed to a flat band in silicene [37]. This band, which is sensitive to the underlying defects in silicene, is expected to reflect the interlayer interaction in epitaxial silicene. Thus, the depression of the intensity of this peak also indicates the weakened interaction between the $\sqrt{3}\times\sqrt{3}$ silicene and the sublayers.

Based on the STM results and dI/dV spectra, we can conclude that (1) buffer layer silicene is

easily oxidized under oxygen atmosphere, even under a small oxygen dose; (2) all the √3×√3 silicene layers show a high resistance to oxygen and retain their ordered lattice structure under oxygen doses up to 2400 L; and (3) the interaction between √3×√3 silicene and the sublayers is weakened by oxygen intercalation, leading to the depression of electron doping from the silver substrate.

Based on the ARPES results, the Fermi velocity is estimated to be about $(4.4 \pm 0.2)\times10^5$ m/s for the pristine sample, although it decreases to about $(3.9 \pm 0.5)\times10^5$ m/s and $(3.4 \pm 0.5)\times10^5$ m/s for the 600 L-oxygen and 1200 L-oxygen intercalated silicene, respectively. In the intercalated silicene, the tensile strain is released, which modifies the hopping parameters and decreases the mobility of electrons [38]. Consequently, the Fermi velocity is expected to be lower in freestanding silicene than in epitaxial silicene. The observed decrease in the Fermi velocity is most likely attributable to the oxygen intercalation process. The Fermi velocity is almost half that of graphene, regardless of oxidation, excluding the possibility of the S_1 surface state of √3×√3-Ag, in which the Fermi velocity is close to that of graphene [39-41]. The ARPES measurements indicate that the √3×√3 silicene layer possesses a high resistance to oxidation and that its Dirac cone structure is robust during oxygen intercalation. The DFT band structure calculations based on the structural model of silicene/SiO_x/Ag [Fig. 7.7 (d)] also show the existence of the characteristic Dirac cone of quasi-free-standing silicene around the Fermi level (Fig. 7.11). Finally, our results suggest that the insulating SiO_x buffer layer provides a barrier for electric gating that can be directly used in FETs. This is significant for the integration of silicene into future microelectronic devices.

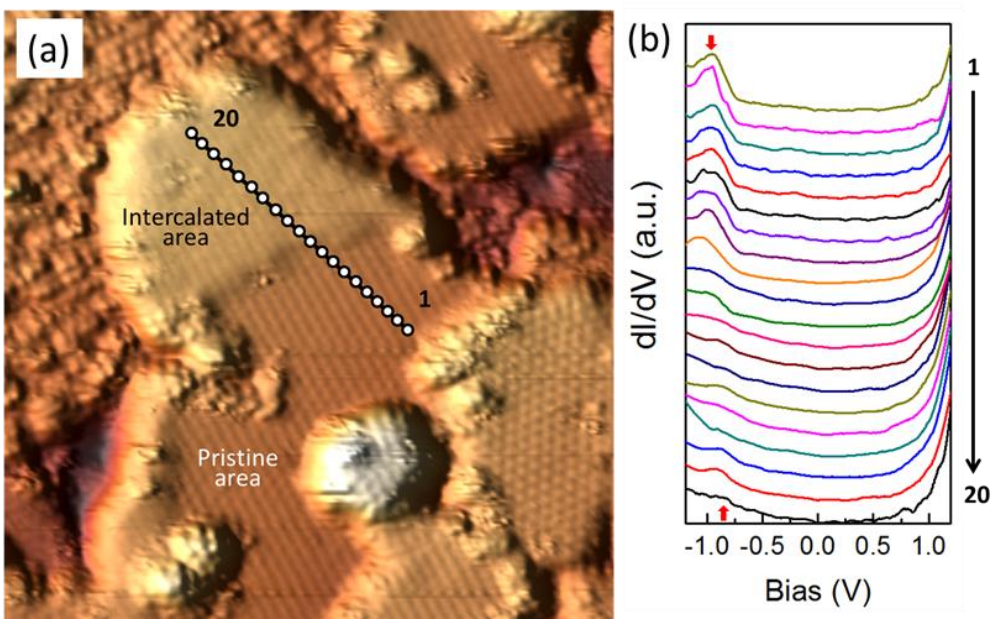

Fig. 7.12 STS in intercalated and pristine areas of √3×√3 silicene. (a) Topography of partially intercalated √3×√3 silicene layer, in which the top left area shows a higher apparent height due to oxygen intercalation (30 nm × 30 nm, V = -1.0 V, I =50 pA). (b) Spatial dependence of tunnelling spectra along the line from the intercalated area to the pristine area that is marked by the white dots in (a) (V = -1.2 V, I = 50 pA, $A_{\text{modulation}}$ = 20 mV, $f_{\text{modulation}}$ = 937 Hz). The red arrows in (b) indicate the peaks attributable to the flat band state in √3×√3 silicene.

7.4 Summary

In summary, we have demonstrated an effective method to make epitaxial silicene quasi-free-standing from Ag(111) substrate by oxygen intercalation. The highly reactive √13×√13 and 4×4 silicene interfacial layers can be fully oxidized, resulting in decoupling of the top silicon atoms from the Ag substrate. Meanwhile, the top √3×√3 silicene layer shows chemical resistance to oxygen, which ensures retention of the honeycomb structure and the characteristic massless Dirac fermions after oxygen intercalation. Moreover, the oxidized √13×√13/4×4 silicene buffer layer (SiO_x) is expected to serve as an ideal dielectric layer for

electric gating purposes in silicene-based FET devices.

1. S. Cahangirov, M. Topsakal, E. Aktürk, H. Şahin, and S. Ciraci, Phys. Rev. Lett. **102**, 236804 (2009).
2. P. Vogt, P. De Padova, C. Quaresima, J. Avila, E. Frantzeskakis, M. C. Asensio, A. Resta,, B. Ealet, and G. Le Lay, Phys. Rev. Lett. **108**, 155501 (2012).
3. B. Feng, Z. Ding, S. Meng, Y. Yao, X. He, P. Cheng, L. Chen, K. Wu, Nano Lett. **12**, 3507 (2012).
4. A. Fleurence, R. Friedlein, T. Ozaki, H. Kawai, Y. Wang, and Y. Yamada-Takamura, Phys. Rev. Lett. **108**, 245501 (2012).
5. L. Meng, Y. Wang, L. Zhang, S. Du, R. Wu, L. Li, Y. Zhang, G. Li, H. Zhou, W. A. Hofer, and H. J. Gao, Nano Lett. **13**, 685 (2013).
6. G. G. Guzmán-Verri and L. C. Lew Yan Voon, Phys. Rev. B **76**, 075131 (2007).
7. L. Tao, E. Cinquanta, D. Chiappe, C. Grazianetti, M. Fanciulli, M. Dubey, A. Molle, and D. Akinwande, Nat. Nanotech. **10**, 227 (2015).
8. H. Pan, Z. Li, C. C. Liu, G. Zhu, Z. Qiao, and Y. G. Yao, Phys. Rev. Lett. **112**, 106802 (2014).
9. D. Tsoutsou, E. Xenogiannopoulou, E. Golias, P. Tsipas, and A. Dimoulas, Appl. Phys. Lett. **103**, 231604 (2013).
10. X. Xu, J. C. Zhuang, Y. Du, H. F. Feng, N. Zhang, C. Liu, T. Lei, J. O. Wang, M. Spencer, T. Morishita, X. L. Wang, and S. X. Dou, Sci. Rep. **4**, 7543 (2014).
11. F. Liu, C. C. Liu, K. H. Wu, F. Yang, and Y. G. Yao, Phys. Rev. Lett. **111**, 066804 (2013).
12. L. Chen, B. J. Feng, and K. H. Wu, Appl. Phys. Lett. **102**, 081602 (2013).

13. E. Cinquanta, E. Scalise, D. Chiappe, C. Grazianetti, B. van den Broek, M. Houssa, M. Fanciulli, and A. Molle, J. Phys. Chem. C **117**, 16719 (2013).
14. H. S. Liu, J. F. Gao, and J. J. Zhao, J. Phys. Chem. C **117**, 10353 (2013).
15. S. Kokott, P. Pflugradt, L. Matthes, and F. Bechstedt, J. Phys.: Condens. Matter **26**, 185002 (2014).
16. J. J. Zhu and U. Schwingenschlögl, ACS Appl. Mater. Interfaces **6**, 11675 (2014).
17. P. De Padova, P. Vogt, A. Resta, J. Avila, I. Razado-Colambo, C. Quaresima, C. Ottaviani, B. Olivieri, T. Bruhn, T. Hirahara, T. Shirai, S. Hasegawa, M. C. Asensio, and G. Le Lay, Appl. Phys. Lett. **102**, 163106 (2013).
18. P. De Padova, C. Ottaviani, C. Quaresima, B. Olivieri, P. Imperatori, E. Salomon, T. Angot, A. Quagliano, C. Romano, A. Vona, M. Muniz-Miranda, A. Generosi, B. Paci, and G. Le Ley, 2D Mater. **1**, 021003 (2014).
19. Y. Du, J. C. Zhuang, H. S. Liu, X. Xu, S. Eilers, K. H. Wu, P. Cheng, J. Zhao, X. D. Pi, K. W. See, G. Peleckis, X. L. Wang, and S. X. Dou, ACS Nano **8**, 10019 (2014).
20. J. Qiu, H. Fu, Y. Xu, A. I. Oreshkin, T. Shao, H. Li, S. Meng, L. Chen, and K. H. Wu, Phys. Rev. Lett. **114**, 126101 (2015).
21. J. Gao and J. Zhao, Surface. Sci. Rep. **2**, 861 (2012).
22. C. Riedl, C. Coletti, T. Iwasaki, A. A. Zakharov, and U. Starke, Phys. Rev. Lett. **103**, 246804 (2009).
23. S. L. Wong, H. Huang, Y. Wang, L. Cao, D. Qi, I. Santoso, W. Chen, and A. T. S. Wee, ACS Nano **5**, 7662 (2011).
24. G. Kresse and J. Furthmüller, Phys. Rev. B **54**, 11169 (1996).
25. G. Kresse and D. Joubert, Phys. Rev. B **59**, 1758 (1999).
26. J. P. Perdew, K. Burke, and M. Ernzerhof, Phys. Rev. Lett. **77**, 3865 (1996).
27. S. Grimme, J. Antony, S. Ehrlich, and S. Krieg, J. Chem. Phys. **132**, 154104 (2010).

28. H. Enriquez, S. Vizzini, A. Kara, B. Lalmi, and H. Oughaddou, J. Phys.: Condens. Matter **24**, 314211 (2012).

29. L. Chen, H. Li, B. Feng, Z. Ding, J. Qiu, P. Cheng, K. Wu, and S. Meng, Phys. Rev. Lett. **110**, 085504 (2013).

30. Z. Ni, Q. Liu, K. Tang, J. Zheng, J. Zhou, R. Qin, Z. Gao, D. Yu, and J. Lu, Nano Lett., **12**, 113 (2012).

31. J. -A. Yan, R. Stein, D. M. Schaefer, X. -Q. Wang, and M. Y. Chou, Phys. Rev. B **88**, 121403 (2013).

32. J. C. Zhuang, X. Xu, Y. Du, K. H. Wu, L. Chen, W. C. Hao, J. O. Wang, W. K. Yeoh, X. L. Wang, and S. X. Dou, Phys. Rev. B **91**, 161409 (2015).

33. D. Beeman, R. Tsu, and M. F. Thorpe, Phys. Rev. B **32**, 874 (1985).

34. A. O'Hare, F. V. Kusmartsev, and K. I. Kugel, Nano Lett. **12**, 1045 (2012).

35. L. Chen, C. C. Liu, B. Feng, X. He, P. Cheng, Z. Ding, S. Meng, Y. Yao, and K. H. Wu, Phys. Rev. Lett. **109**, 056804 (2012).

36. B. Feng, H. Li, C. C. Liu, T. N. Shao, P. Cheng, Y. Yao, S. Meng, L. Chen, and K. H. Wu, ACS Nano 7, 9049 (2013).

37. Y. Feng, B. J. Feng, Z. J. Xie, W. B. Li, X. Liu, D. F. Liu, L. Zhao, L. Chen, X. J. Zhou, and K. H. Wu, Chin. Phys. Lett. **31**, 127303 (2014).

38. J. Yan, S. Gao, R. Stein, and G. Coard, Phys. Rev. B. **91**, 245403 (2015).

39. H. Aizawa, M. Tsukada, N. Sato, and S. Hasegawa, Surf. Sci. **429**, L509 (1999).

40. T. Shirai, T. Shirasawa, T. Hirahara, N. Fukui, T. Takahashi, and S. Hasegawa, Phys. Rev. B **89**, 241403 (2014).

41. R. Arafune, C. L. Lin, R. Nagao, M. Kawai, and N. Takagi, Phys. Rev. Lett. **110**, 229701 (2013).

CHAPERTER 8

CONCLUSIONS AND RECOMMENDATIONS

8.1 Conclusions.

The influence of substrate temperature and coverage level on growth dynamic mechanism for silicene is investigated. Defects in the $\sqrt{13}\times\sqrt{13}$ phase are evoked by both the grain boundaries between different phases and the low coverage. Deficiencies of atoms in the top layer form the defects in the 4×4 phase, which may be induced by the great number of atoms in the top layer and the weak bonds between the top layer atoms and the silver atoms in substrate. The lattice mismatch between the silicene and the substrate induces the breakages and distortions in the dark part of the moiré pattern in the $2\sqrt{3}\times2\sqrt{3}$ phase. Our results imply that the growth mechanism of silicene is under the SK mode, providing a better understand the complex thermodynamics and kinetics at the core of silicene formation, and a route towards fabricating novel nanostructures for application in the microelectronics industry.

Silicene layers with different structures and coverage have been fabricated, and identified by in situ UHV Raman spectroscopy and STM. The intrinsic phonon modes for different silicene structures are identified. We found that EPC strength in silicene could be significantly enhanced due to the lattice mismatch between silicene layers and the substrate. The Raman spectroscopy demonstrates the effects of coverage, strain, charge doping, and defects on silicene's phonon modes, and allows unambiguous, high-throughput, nondestructive identification of epitaxial silicene.

An electronic band gap in monolayer silicene on the Ag(111) substrate was produced by oxidation, verified by STM combined with *in-situ* Raman spectroscopy studies. O^d is the most energetically favored configuration for the oxygen adsorption on the surfaces of all

three silicene superstructures. The different buckled structures lead to different heights of oxygen adatoms on the silicene. The sized of band gap could be modulated from semimetallic to semiconducting type, which can overcome the zero-gap disadvantage of silicene. In fully oxidized silicene, the buckled silicene structure vanishes, with subsequent crumpling of the sample as well as exposure of bare Ag(111) surface areas.

The oxidation effects on the structure and electronic properties of 4×4 silicene on Ag(111) are investigated. After oxidation, the silicene oxide exhibits an amorphous structure with a semiconductor-like band structure. By combining DFT calculations and ARPES results, it is proved that the 2D metallic surface state in 4×4 silicene on Ag(111) is ascribed to hybridization of Si p_z and Ag 3*d* states. The hybridization is broken and the Ag(111) Shockley surface state could be revived after silicene is oxidized. This surface band demonstrates high chemical activity, facilitating chemical functionalization of silicene layers.

An effective method to make epitaxial silicene quasi-free-standing from Ag(111) substrate by oxygen intercalation is proposed. The highly reactive √13×√13 and 4×4 silicene interfacial layers can be fully oxidized, resulting in decoupling of the top silicon atoms from the Ag substrate. Meanwhile, the top √3×√3 silicene layer shows chemical resistance to oxygen, which ensures retention of the honeycomb structure and the characteristic massless Dirac fermions after oxygen intercalation. Moreover, the oxidized √13×√13/4×4 silicene buffer layer (SiO_x) is expected to serve as an ideal dielectric layer for electric gating purposes in silicene-based FET devices.

8.2 Recommendations.

1. More detailed research on the atomic structure of silicene, especially for √3×√3 silicene,

should be performed. √3×√3 silicene grown on Ag(111) shares structural similarities with Si(111)-(√3×√3)-Ag surface, which leads recent arguments on whether STM-observed √3×√3 silicene would be Si(111)-(√3×√3)-Ag reconstruction or not. This issue is crucial for the future development of this material. Thus, the comprehensive supplementary works on Si(111)-(√3×√3)-Ag samples in addition to the √3×√3 silicene on Ag(111) are required.

2. More vibrational modes are induced by various edge arrangements in silicene Raman spectroscopy, consisting well with the emergency of D_1–D_5 peaks. The edge-induced Raman peaks reflect the unique buckled characteristic in silicene. However, distinguishing the origin of these peaks is still need to be clarified to futher functionizing this material. Tip-enhanced Raman spectroscopy is likely to advance insights into the edge effects on phonon modes in this low-buckled 2D material.

3. Transport measurement on the epitaxial is desired to confirm its Dirac fermion characteristics. The high resisitivity of √3×√3 proved by our works enhances the possibility of the *ex-situ* measurements. The realization of free-standing silicene will be the next aim to exlclude the conductive substrate effect.

APPENDIX A: PUBLICATION LIST

1. Zhi Li, **Jincheng Zhuang (Co-first author)**, Lan Chen, Zhenyi Ni, Chen Liu, Li Wang, Xun Xu, Jiaou Wang, Xiaodong Pi, Xiaolin Wang, Yi Du, Kehui Wu, and Shi Xue Dou, ACS Central Science DOI: 10.1021/acscentsci.6b00152
2. Yi Du, **Jincheng Zhuang**, Jiaou Wang, Zhi Li, Hongsheng Liu, Jijun Zhao, Xun Xu, Haifeng Feng, Lan Chen, Kehui Wu, Xiaolin Wang, and Shi Xue Dou, Sci. Adv. **2**, e1600067 (2016).
3. Zhi Li, Haifeng Feng, **Jincheng Zhuang**, Na Pu, Li Wang, Xun Xu, Weichang Hao, and Yi Du, J. Phys.: Condens. Matter **28**, 034002 (2016).
4. Xiong Li, Yufeng Zhang, Feifei Yuan, **Jincheng Zhuang**, Zhimin Cao, Xiangzhuo Xing, Wei Zhou, and Zhixiang Shi, J. Alloy Compd. **664**, 218 (2016).
5. **Jincheng Zhuang**, Zhi Li, Xun Xu, Li Wang, Wai Kong Yeoh, Zhixiang Shi, Xiaolin Wang, Yi Du, and Shi Xue Dou, Appl. Phys. Lett. **107**, 222601 (2015).
6. Xiong Li, Xintong Shi, Jiaping Wang, Yufeng Zhang, **Jincheng Zhuang**, Feifei Yuan, and Zhixiang Shi, J. Alloy Compd. **644**, 523 (2015).
7. **Jincheng Zhuang**, Xun Xu, Haifeng Feng, Zhi Li, Xiaolin Wang, and Yi Du, Sci. Bull. **60**, 1551 (2015).
8. **Jincheng Zhuang**, Xun Xu, Yi Du, Kehui Wu, Lan Chen, Weichang Hao, Jiaou Wang, Wai Kong Yeoh, Xiaolin Wang, and Shi Xue Dou, Phys. Rev. B **91**, 161409(R) (2015).
9. Xiong Li, **Jincheng Zhuang**, Yue Sun, Jing Bai, Zainab Zafar, Zhenhua Ni, Biaobin Jin, and Zhixiang Shi, Carbon **82**, 346- (2015).
10. Xun Xu, **Jincheng Zhuang (Co-first author)**, Yi Du, Haifeng Feng, Nian Zhang, Chen Liu, Tao Lei, Jiaou Wang, Michelle Spencer, Tetsuya Morishita, Xiaolin Wang, and Shi Xue Dou, Sci. Rep. **4**, 7543 (2014).

11. **Jincheng Zhuang**, Wai Kong Yeoh, Xiangyuan Cui, Xun Xu, Yi Du, Zhixiang Shi, Simon P. Ringer, Xiaolin Wang, and Shi Xue Dou, Sci. Rep. **4**, 7273 (2014).
12. Yi Du, **Jincheng Zhuang**, Hongsheng Liu, Xun Xu, Strfan Eilers, Kehui Wu, Peng Cheng, Jijun Zhao, Xiaodong Pi, Khay Wai See, Germanas Peleckis, Xiaolin Wang, and Shi Xue Dou, ACS Nano **8**, 10019 (2014).
13. **Jincheng Zhuang**, Wai Kong Yeoh, Xiangyuan Cui, Jung Ho Kim, Dongqi Shi, Zhixiang Shi, Simon P. Ringer, Xiaolin Wang, and Shi Xue Dou, Appl. Phys. Lett. **104**, 262601 (2014).
14. Wei Zhou, **Jincheng Zhuang**, Feifei Yuan, Xiong Li, Xiangzhuo Xing, Yue Sun, and Zhixiang Shi, Appl. Phys. Express **7**, 063102 (2014).
15. Wei Zhou, Yue Sun, Shuo Zhang, **Jincheng Zhuang**, Feifei Yuan, Xiong Li, Zhixiang Shi, Tatsuhiro Yamada, Yuji Tsuchiya, and Tsuyoshi Tamegai, J. Phys. Soc. Jpn. **83**, 064704 (2014).
16. Wei Zhou, Xiong Li, Xuan Zhou, Feifei Yuan, Yi Ding, **Jincheng Zhuang**, Yue Sun, and Zhixiang Shi, J. Low Temp. Phys. 175, **543** (2014).
17. Xun Xu, **Jincheng Zhuang**, Yi Du, Strfan Eilers, Germanas Peleckis, Wai Kong Yeoh, Xiaolin Wang, Shi Xue Dou, and Kehui Wu, International conference on nanoscience and nanotechnology (ICONN) **28** (2014).
18. Feifei Yuan, Yi Ding, Yue Sun, **Jincheng Zhuang**, Wei Zhou, Guangze Li, Michael D. Sumption, Xiaowei Li, and Zhixiang Shi, Physica C **495**, 198 (2013).
19. Yue Sun, Wei Zhou, Lijun Cui, **Jincheng Zhuang**, Yi Ding, Feifei Yuan, Jing Bai, and Zhixiang Shi, AIP adv. **3**, 102120 (2013).
20. Wei Zhou, Feifei Yuan, **Jincheng Zhuang**, Yue Sun, Yi Ding, Lijun Cui, Jing Bai, and Zhixiang Shi, Supercond. Sci. Technol. **26**, 095003 (2013).

21. Yue Sun, Yi Ding, Dongmei Gu, **Jincheng Zhuang**, Zhixiang Shi, and Tsuyoshi Tamegai, J. Phys. Soc. Jpn **82**, 074713 (2013).
22. **Jincheng Zhuang**, Yue Sun, Yi Ding, Feifei Yuan, Xun Jia, Zhixiang Shi, and Haiyan Huang, J. Low Temp. Phys. **172**, 113 (2013).
23. **Jincheng Zhuang**, Yue Sun, Yi Ding, Feifei Yuan, Jiatao Liu, Zhixiang Shi, and Xiaowei Li, Mod. Phys. Lett. B **26**, 1250197 (2012).
24. Yi Ding, Guangze Li, Ying Yang, Chris. J. Kovacs, Michael A. Susner, Michael D. Sumption, Yue Sun, **Jincheng Zhuang**, Zhixiang Shi, Milan Majoros, and Edward W. Collings, Physica C **483**, 13 (2012).
25. Yi Ding, Yue Sun, **Jincheng Zhuang**, Lijun Cui, Zhixiang Shi, Michael D. Sumption, Milan Majoros, Michael A. Susner, Chris J. Kovacs, Guangze Li, Edward W. Collings, and Zhian Ren, Supercond. Sci. Technol. **24**, 125012 (2011).
26. Yi Ding, Yue Sun, Xiangde Wang, **Jincheng Zhuang**, Lijun Cui, and Zhixiang Shi, Supercond. Sci. Technol. **24**, 095014 (2011).
27. Yue Sun, Yi Ding, **Jincheng Zhuang**, Lijun Cui, Xuepin Yuan, Zhixiang Shi, and Zhian Ren, Supercond. Sci. Technol. **24**, 085011 (2011).

APPENDIX A: RECEIVED AWARDS

1. Excellent Postgraduate Scholarship of Southeast University (2012).
2. Oversea Short-Term Visiting Scholarship of Southeast University (2013).
3. Funding by Scientific Research Foundation of Graduate School of Southeast University (2014).
4. International Postgraduate Tuition Award (IPTA) of University of Wollongong (2014).
5. ISEM Student Excellence Award (2014).
6. Excellent Ph.D thesis of Southeast University (2015).